A New Cold Molecule Source: The Buffer Gas Cooled Molecular Beam

A Dissertation
Presented to the Faculty of the Graduate School
of
Yale University
in Candidacy for the Degree of
Doctor of Philosophy

by
Jessie A. Petricka

Dissertation Director: David Demille

December 2007

Abstract

A New Cold Molecule Source: The Buffer Gas Cooled Molecular Beam

Jessie A. Petricka
2007

This thesis outlines the construction of a novel apparatus for the production of ultracold polar molecules. The machine produces molecules via laser ablation, which then thermalize by contact with cryogenically cooled helium buffer gas. Extraction of the thermalized molecules through an aperture in the buffer gas cell forms a molecular beam. Experiments with the species SrO characterize both the thermalization and extraction process in the buffer gas cell. Beam properties such as temperature and flux are defined and explored in simple models; the observed results with molecular SrO are presented and compared with the models.

A broad set of applications for the production of ultracold polar molecules sets the motivation of atomic and molecular physics goals and directs the beginning of this thesis. The outline of several different techniques in pursuit of this goal are discussed. The buffer gas cooling process and beam are then generally described. The construction and operation of the apparatus is then presented. Results with SrO demonstrate progress toward the goal. Finally, a scheme for reaching ultracold temperatures with guiding and trapping of molecules from this beam source is presented.

Dedication

For *Jalean*, *Leif*, my *family*, and my *faith*.

In all you do, surround yourself with friends
rely on them to carry you forward
for they will bring you to your final goal

Contents

Abstract **iii**

Dedication **iv**

1 Introduction **1**

1.1 Motivation 2

1.1.1 Atoms 2

1.1.2 Polar molecules 3

1.2 Applications of cold molecules 3

1.2.1 Precision measurement 3

1.2.2 Molecular interactions 7

1.2.3 Quantum devices 10

1.2.4 Ultracold requirement 12

1.3 Summary 13

2 Producing cold molecules **14**

2.1 Laser cooling 14

2.2 Molecules from cold atoms 16

2.2.1 Photoassociation 16

2.2.2 Feshbach resonance 17

2.3 Direct cold molecule production 17

2.3.1 Stark decelerator 17
2.3.2 Laser Stark decelerator 18
2.3.3 Quadrupole filtering 19
2.4 Buffer gas cooling 20
2.4.1 Previous work 21
2.4.2 Molecule-buffer gas collisions 22
2.4.3 Extraction efficiency estimate 25
2.4.4 Simulation of the cooling process 30
2.4.5 Choosing a molecule: SrO 32

3 Experimental apparatus 35

3.1 Vacuum assembly 37
3.1.1 Vacuum chamber 37
3.1.2 Vacuum viewports 38
3.1.3 Support structure 39
3.1.4 Vacuum pumping system 41
3.1.5 Charcoal sorb 43
3.2 Cryogenics 44
3.2.1 Blackbody radiation 45
3.2.2 Thermal conductivity 46
3.2.3 Thermal contractions 47
3.2.4 Cryostat design 50
3.2.5 Nitrogen shield and bath 53
3.2.6 Optical baffles 55
3.2.7 Cooling down 56
3.3 Buffer gas cell 57
3.3.1 He gas inlet 59

3.3.2 Cell density determination 60
3.4 Ablation laser setup 62
3.5 Detection laser setup 65
3.5.1 Diode laser 65
3.5.2 AOM setup 66
3.6 Locking the laser frequency 67
3.6.1 Locking apparatus 70
3.6.2 Fabry-Perot transfer cavity 70
3.6.3 He-Ne laser 73
3.6.4 Diode laser optical setup 73
3.6.5 Lock performance 76
3.6.6 Ratchet lock 77
3.7 Absorption detection 79
3.8 Fluorescence detection 82
3.8.1 Collection lenses and signal filtering 83
3.9 Summary 87
3.9.1 Improvements 87

4 Studies with strontium oxide **89**
4.1 Room temperature yield 89
4.1.1 Determining the yield 90
4.2 Lifetime of the excited state 95
4.3 Buffer gas cooling at 4K 98
4.4 Collision cross section 98
4.5 Saturation intensity 102
4.6 Buffer gas molecular beam 106
4.6.1 Beam flux 107

4.6.2 Rotational temperature 108
4.6.3 Velocity distribution 110
4.6.4 Enhanced yield observation 117
4.7 Summary and improvements 119

5 Beyond 4K: guiding and trapping 123
5.1 Guiding the molecules 124
5.1.1 DC Stark effect 125
5.1.2 Quadrupole field 129
5.1.3 Molecule energies in a quadrupole field 130
5.1.4 Guide construction and testing 132
5.2 Molecule trapping 136
5.3 AC Stark effect 137
5.4 Linear polarization 139
5.5 Circular polarization 144
5.6 Microwave trap design 145
5.7 Future directions 148

List of Figures

1.1 Schematic of how an electron EDM violates a time reversal operation. 5

1.2 A coordinate system involving an electric field $\vec{\mathcal{E}}$, a magnetic field $\vec{B}$ and a direction $\vec{k}$ (of a molecule or light beam for example), and a configuration with opposite parity. 7

1.3 Four different configurations for the orientation of two molecules. . . 8

1.4 Schematic of the use of cold polar molecules for quantum computation. 12

2.1 Loss from the laser cooling of a non-closed transition. 15

2.2 Saturated density of ^{4}He vapor versus temperature. 26

2.3 Thermalization and beam extraction model in a buffer gas cooling cell. 28

2.4 1D beam extraction model for large buffer gas density. 29

2.5 Streamlines and flow speed in a buffer gas cell. 31

3.1 Broad outline of the buffer gas beam apparatus. 36

3.2 Mechanical drawings of the experimental chamber. 37

3.3 Vacuum viewport fogging problem and solution. 40

3.4 Drawing of the experimental chamber support structure. 41

3.5 Thermal conductance of copper metallic joint with various coupling compounds. 48

3.6 Construction of a cryogenic joint. 49

3.7 Mechanical drawing of cryostat top and bottom views. 51

3.8 Mechanical drawing of cryostat, side view. 52
3.9 Schematic of nitrogen cooled baffles. 56
3.10 Configurations of the buffer gas cell. 59
3.11 Ablation yield for repeated ablation of the same target point. 64
3.12 Molecule flux as a function of time for a quick series (100Hz rate) of 5 ablation pulses. 65
3.13 Schematic of a double pass AOM setup. 68
3.14 Overview of the laser lock optical setup. 74
3.15 Combined efficiency of the locking optical setup to the input of the Fabry-Perot cavity. 76
3.16 The ratchet lock process. 77
3.17 Schematic of ablation plume. 81
3.18 Schematic of lens arrangements for the collection of fluorescence light. 84
3.19 Ray tracing of fluorescence light in the two lens detection setup (with plano-spherical lenses). 85

4.1 Experimental setup of the room temperature buffer gas setup. 91
4.2 Simulation of the thermalization process. 93
4.3 Room temperature fractional absorption of SrO. 96
4.4 Data set determining the lifetime τ of the $|A^1\Sigma, J' = 1, v'' = 1\rangle$ state. 99
4.5 Lifetime measurement for the SrO excited $|A^1\Sigma, J' = 10, v'' = 1\rangle$ state. 100
4.6 Characteristic data from the SrO-He cross section determination. . . 103
4.7 SrO-He cold cross section determination. 104
4.8 Setup of the buffer gas beam measurements. 107
4.9 Typical fluorescence data trace. 109
4.10 Molecular beam temperature characterization. 111
4.11 Forward velocity boost in the molecular beam. 116

4.12 Molecule flux in the molecular beam as a function of buffer gas density. 120
4.13 Beam flux and boost for the large cell, 3 mm aperture geometry. . . . 122

5.1 DC Stark effect in polar diatomic molecules as a function of electric field strength. 128
5.2 Left: general quadrupole guide geometry of radius R. Right: photograph of the constructed and tested guide using 0.25" diameter rods. 130
5.3 DC Stark energies of the $|1,0\rangle$ molecular state in the two dimensional quadrupole electric field. 132
5.4 Diagram of a typical Paschen curve. 134
5.5 Diagram of the cell and (foreground) guides, showing the manner in which ion filtering voltages were applied. 135
5.6 Dressed-state energy level diagrams for rotational states of a diatomic molecule subject to a linear ($\vec{\epsilon} = \hat{z}$) microwave electric field. 140
5.7 Energies of dressed states vs. applied microwave electric field strength for linear polarization ($\vec{\epsilon} = \hat{z}$). 142
5.8 Energies of dressed states vs. applied microwave electric field strength for linear polarization ($\vec{\epsilon} = \hat{z}$), partial subspace. 143
5.9 Dressed-state energy level diagram for rotational states of a diatomic molecule subject to a circular ($\vec{\epsilon} = (\hat{x} - i\hat{y})/\sqrt{2}$) microwave electric field. 146
5.10 Energies of dressed states vs. applied microwave electric field strength for circular polarization ($\vec{\epsilon} = \frac{1}{\sqrt{2}}\hat{x} - i\hat{y}$). 147

List of Tables

2.1 Overview of SrO molecular properties. 34

2.2 Franck-Condon factors in the SrO $X^1\Sigma v'' \Leftrightarrow A^1\Sigma\, v'$ transition and the approximate wavelength, of the band origins. 34

2.3 Overview of SrO two body reactions. 34

3.1 Thermal conductivity integrals in several materials in units of W/cm. 47

3.2 Thermal expansion $\Delta L/L = (L_T - L_{293})/L_{293}$ (in percent) of several materials at $T = 4$ K and 77 K. 48

4.1 Parameters involved in the molecule beam fluorescence detection. . . 109

5.1 Outline of the maximum Stark shift, ΔE_{Max}, for the first three (zero field labeled) $|J, 0\rangle$ weak field seeking states, and the field strength $\mathcal{E}_{\mathrm{turn}}$ where it occurs. 129

Chapter 1

Introduction

After plateauing somewhat, atomic physics has seen a remarkable resurgence of interest in recent decades. This is due, in large part, to the development of technologies and techniques that allow for complete control over atomic parameters and interactions. Now, not only the internal degrees of freedom such as quantum state, but external degrees of freedom such as motion, can be manipulated coherently. Further, control is not limited to single particle properties. Particle-particle collisions, collective behavior and quantum entanglement are but some of the ways to control groups of atoms. Such power of atomic control has opened the door to a host of new effects, applications and investigations. Yet while exciting research and breakthroughs continue in atomic research, there is a great interest in achieving the same level of control in molecules. The hope, and to some degree expectation, is that full molecular control will provide even more interesting phenomena and more powerful applications.

This thesis describes the pursuit of molecular control with a new apparatus whose goal is to produce ultracold, trapped, polar molecules. The current device, constructed over the course of this study, produces a cold molecular beam for use in the ongoing program. Novel features of this beam source including its high flux make it extremely useful for this purpose, and also perhaps in other experiments where high count rates are profitable.

1.1 Motivation

1.1.1 Atoms

The revolution in technologies and techniques available to the atomic physicist began with the incredible tool that is the laser [1]. Using this narrow band coherent source, the term precision in precision spectroscopy gained a whole new meaning. With it, new measurements were made that shed light on the structure of atoms and aided the development of relativistic theories and atomic models. In addition to using this narrow band source for spectroscopy, it was realized [2] that the light from a laser could exert a force on atoms to slow their motion. Some ten years of experimental work later, the "optical molasses" technique [3] showed that pairs of laser beams could indeed be used to cool atoms's motional degrees of freedom. Further work led to the magneto-optical-trap (MOT) [4], which combines the molasses with magnetic fields to confine the atoms to a region in space. From these beginnings, development after development has led to a situation today that routinely enables confinement of greater than 10^7 atoms at temperatures less than 250 nK [5].

These ultra-low temperatures have allowed for a host of studies of new effects, such as the realization of Bose-Einstein Condensation and other phase transitions [6, 7, 8]. Ultracold temperatures have also allowed atoms to be used in technical applications. For example, cold-atom matter-wave interferometers [9] can be used to sense inertial and rotational motions. In addition, atomic gravitational [10] and magnetic field [11] sensors are now among the most sensitive of their kind. Even more astounding is that precise measurements of the cesium atom actually *define* the standard of time [12] by the period of its oscillation.

1.1.2 Polar molecules

The extension of atomic techniques to create systems of ultracold polar molecules is expected to have as broad an impact on science, both pure and practical, as atoms. Molecules, however, are just on the leading edge of converting interest into results. This leads to a giddy situation where both the theorist and experimentalist can dream; dream of the possible applications and the apparatus that will support them.

1.2 Applications of cold molecules

1.2.1 Precision measurement

Loosely termed, modern precision measurement physics seeks to probe the underlying nature of theories with very sensitive measurements of fundamental properties and interactions. Many atomic physics experiments have verified the standard precepts of quantum mechanics, newer areas of the field are branching out into areas like high-energy or nuclear physics. While it might sound odd that atomic and molecular physics is capable of providing insight into exotic particles created in high energy accelerators, or theories that delve past the standard quantum mechanics that describes them so well, in fact the opposite is true. This field has profound relevance and moreover is one of the most exciting (in the authors' view) in which to study new physics. The reason, as could be expected, is that the degree to which we know the atom (and molecule) through measurement is astounding. Comparison between measurements and theoretical predictions allow even seemingly small effects to be tested, to a fantastic level. Thus atomic and molecular systems and measurements can play a direct role in determining, or refining theories in a wide range of areas.

EDM

At the most pure end of scientific studies is the use of polar molecules to search for an electric dipole moment (EDM) of the electron. An electron, in our most basic of understandings, is a point charge. However, the possibility exists, upon closer examination, that the electron has some asymmetric charge distribution leading to a permanent electric dipole moment. The existence of an EDM, however, would not only change our view of the electron, but could also change our understanding of the fundamental precepts of nature. This is because an EDM would violate the time reversal symmetry of nature, because an electron and its time reversed version would have different relative orientations of its EDM and spin (see figure 1.1).

Thus searches for a permanent electric dipole moment of the electron [13, 14] provide some of the most stringent constraints on physics beyond the standard model [15] because they constrain *ad-hoc* time-reversal violating processes. Although an EDM is predicted in the standard model, it arises only in high levels of perturbation theory [16]. As a result, the predicted value for the electron EDM is exceedingly small [15]; so small in fact, that measurement of its existence is outside the reach of any current modern physics experiment. However, in many theoretical extensions to the standard model, for example in supersymmetric theories [17], an EDM could arise at low levels of perturbation. New paths to EDM creation in many of these extended theories puts the predicted value for the electron EDM much higher than the standard model value.

These predictions put the electron EDM value near, or just below, the limits of our ability to measure. Currently, the most sensitive measurement of the electron EDM is done in an atomic thallium system [13]. This atom has an energy structure typical of most atoms and has energy levels of opposite parity separated by $\sim$3 eV. This allows for only a small polarization of the atom in the lab frame, even when placed

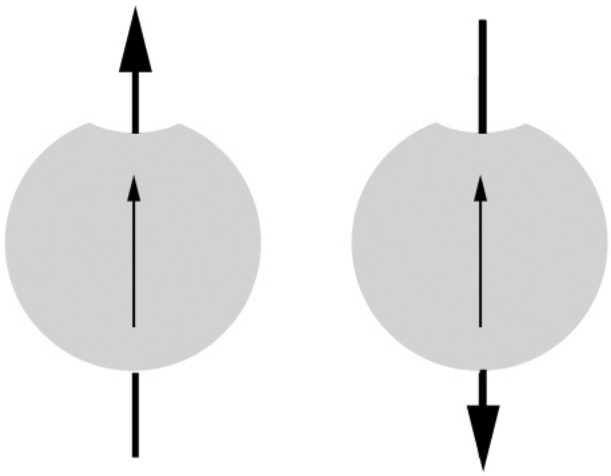

Figure 1.1: Schematic of how an electron EDM violates a time reversal operation. On the left, the electron rotates around its spin axis (large arrow). The dipole (small arrow) associated with the electrons' asymmetry (small dimple) is parallel with the spin axis (left). Under a time reversal operation (right), the electron reverses its spin direction, but not its spatial orientation. Thus a time reversal operation produces an electron whose spin and electric dipole change relative orientation.

in a large electric field. Since the measured EDM effect in atoms (and molecules) is a relativistic one [18], where (fast) motion of the electron near the nucleus allows its EDM to asymmetrically interact with the lab frame polarization, the ideal EDM candidate atoms are both heavy (where relativistic effects are more pronounced) and polarizable.

Polar molecules have the ability to make more sensitive measurements of an electron EDM [19] because placing a polar molecule in even a modest electric field can fully polarize the molecule, in the lab frame. Further, the molecule's large internal electric field (oriented along the molecular polarization) leads to an enhanced sensitivity to the lab fields for the relevant molecular EDM effect. With diatomic (polar) molecules, one has a plethora of search choices, including molecules that are easier to polarize, heavier, easier to deal with (detect, etc.), in order to optimize an EDM search.

Parity violation

In addition to time-reversal, parity is also a symmetry of nature that is obeyed to a high degree. In general, parity violation produces measurable differences between systems with a right-handed and a left-handed coordinate systems. This is realized in the lab, for example, by reversing the direction of a field or velocity (see figure 1.2). We know now that parity violation is intimately intertwined with the weak force and indeed was first observed in nuclear systems via measurements in beta decay [20] processes. Atomic [21] and molecular [22] measurements of parity violation, however, are unique in that the use of different systems or parameters can not only test the low energy validity of the standard model parity violating processes, but also can allow study of the different mechanisms that generate parity violation.

The most sensitive measurement of parity violating effects in atoms [21] is in atomic cesium. This experiment relies on the precise control and detection of the internal state of the atom to measure parity violating mixing of the atomic S and P states. Measurement of the level of parity violation comes from the degree that the selection rule between the ground 6s state and electronically excited 7s state (forbidding transition between them) is broken. Much like the EDM case, the experiment utilizes mixing between levels that are separated by $\gtrsim$1 eV.

Molecules, in contrast to atoms, have levels of opposite parity that naturally lie much closer together, their rotational levels [23]. With the use of magnetic fields and the Zeeman effect, these opposite parity levels can even be brought into resonance, thereby allowing the parity violating amplitude to be one of the major effects in the system, a whole new regime for making detailed measurements of its effects. Again, like the electron EDM, effects of parity violation in molecules are quite generally enhanced over the atomic case. Further, in molecular experiments, the possibility of using different molecular species allows the experimenter to further probe the different

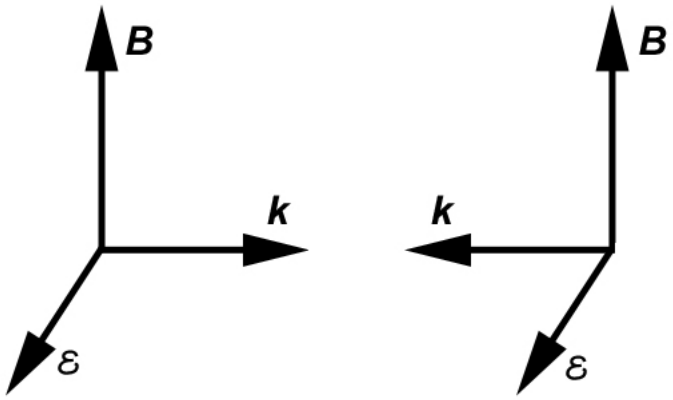

Figure 1.2: A coordinate system involving an electric field $\vec{\mathcal{E}}$, a magnetic field $\vec{B}$ and a direction $\vec{k}$ (of a molecule or light beam for example), and a configuration with opposite parity. Parity violation would produce differences between measurements of these systems.

contributions to the parity violating effect.

1.2.2 Molecular interactions

Studies of molecular collisions can lead one to think that the whole affair is complicated and confusing. This is because at large collision energy, the internal energies of the colliding molecules can undergo changes from their initial state [24] either virtually during an elastic collision process, or in the final state, leading to an inelastic scattering event. Collisions at ultracold temperatures simplify this picture substantially. Here, excited internal states of the colliding pair are that are energetically inaccessible drop out of the problem for inelastic processes. In addition, the number of scattering partial waves involved is reduced.

What makes polar molecular collisions distinct from atomic ones is not only the variety of (low lying) molecular states that can be accessed, but also the fundamental interaction between particles. Whereas the interaction energy between neutral atoms E_{vdw} is due to the van der Waals force, polarized molecules interact via the dipole-

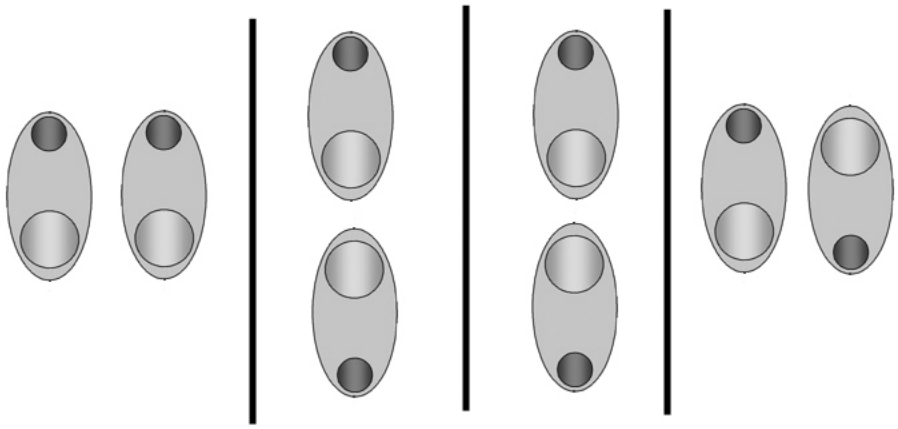

Figure 1.3: Four different configurations for the orientation of two molecules, shown from left to right as being from most repulsive to most attractive. A polarized molecule can be pictured as separated charges; when like charges approach one another the interaction is repulsive and when opposite charges approach one another the interaction is attractive.

dipole force giving an entirely different form of the interaction energy E_{dip}:

$$E_{\text{vdw}} = \frac{C_6}{r^6}\,, \tag{1.1}$$

$$E_{\text{dip}} = \frac{\vec{d_1}\cdot\vec{d_2} - 3(\hat{r}\cdot\vec{d_1})(\hat{r}\cdot\vec{d_2})}{r^3}\,. \tag{1.2}$$

The differences between these interactions first shows that the molecular interaction is much longer range ($1/r^3$) than the atomic interaction ($1/r^6$). Also, the dipole-dipole energy depends on orientation of the dipoles $\vec{d_1}$ and $\vec{d_2}$ relative to one another, and relative to their separation $\vec{r}$ (see figure 1.3). This strong, anisotropic interaction is the cornerstone on which many of the interesting departures from cold atoms is laid.

Of particular interest is the tunability of this interaction, due to the tunability of molecular dipoles. What does it mean for a molecular dipole to be tunable? A polar molecule is easily seen to have a permanent dipole in its rest frame. In the lab frame free of electric fields, however, the molecule is equally likely to point in any direction, so the dipole averages to zero. Only when electric fields are applied does the molecule

become oriented by the field and acquire a dipole moment.

Phase transitions

This tunable dipolar interaction, coupled with an ultracold environment, has the potential ability to open up a whole new area of phase transition studies. For example, quantum phases such as the superfluid and Mott insulator can be studied with an additional dipolar interaction [25]. In addition, the existence of new quantum phases due to this interaction are a distinct possibility. For instance the superfluid, characterized by its lack of flow resistance, may be modified into a phase characterized by both this property *and* spatial order, referred to as a supersolid [26]. Another example is a modification of the Mott insulator phase, where atoms are number-squeezed into individually occupied lattice sites. Here the Mott insulator, in the presence of dipolar interactions, could give rise to ferroelectric states, or fractional occupation states with various forms of spontaneous symmetry breaking [27]. Since the dipolar interaction is tunable, these states, and transitions between them, can be created and tuned with an applied electric field. Such control over phase transitions is akin to, but potentially more powerful and far reaching than, the exciting work being done in Feshbach transitions in atoms [28].

Quantum chemistry

With precise manipulation over the motion of a molecule, its internal state and orientation, the experimenter has all the knobs needed to carefully study the controlled collisions of molecular species. Limiting molecular collisions based on these parameters can provide insight into the nature of chemical reactions. For energetically suppressed reactions, quantum tunneling [29] can drive the reaction, even at zero energy. Again, varying an applied external field can alter both the character of the pairwise collisions and their reaction products [30], by turning on anisotropic dipolar

interactions.

1.2.3 Quantum devices

Quantum computer

The development of a computer that is based on quantum mechanical interactions is the goal of many different fields. The reason for this interest is that many tasks could be solved *much* more efficiently by a quantum computer, among them: the search [31] and traveling-salesman problems, factorization [32], and encryption [33] tasks. In addition, the use of a quantum computer to simulate other quantum systems could be a very powerful tool for the understanding and development of strongly coupled media (for instance in understanding high T_c superconductors [25]). The development of many different schemes [34] for use as a quantum computer leads to a large and diverse battleground for ideas, attention and resources. Currently, though, no single approach has overcome the technical hurdles to create a viable competitor to the classical computer. The use of ultracold polar molecules for quantum computation [35, 36, 37] is an attractive solution: enough so that our research group also has two active polar molecule production studies (including this one) with quantum computation as one of its goals.

The basic building block of the quantum computer consists of the qubit, the unit of storing information. Much like the classical bit, the qubit can occupy states labeled $|0\rangle$ and $|1\rangle$. Unlike the classical case, however, a single qubit can exist in any linear superposition of the states. Moreover, multiple qubits can be correlated through interactions leading to entanglement. It is this ability to be correlated that gives the quantum computation its edge over classical computing. Actually building a machine that exploits these quantum effects, however, requires a few other metrics to be met. The generally accepted criteria for realization of a quantum computer are:

- scalability
- initialization
- long coherence times
- gating operations
- readout

The polar molecule quantum computer appears well suited to satisfy all of these requirements. In the molecular realization of the quantum computer (see figure 1.4), the up/down orientation of the molecular dipole moment are the qubit $|0\rangle$ and $|1\rangle$ states. More specifically, these two states are the lowest two rotational states of the molecule mixed (polarized) in an external field. Forming a register of bits in a standing wave optical lattice with one molecule per lattice site allows for scalability of the system. Use of molecules at ultracold temperatures allows for weak trapping fields leading to very long coherence times. Varying an external electric field across the lattice Stark-shifts each molecule as a function of position, allowing for individual gating, initialization, and readout with microwave and laser fields. Since the molecules are polarized, strong dipole-dipole interactions between neighbors allows for individual gates to be faster than any decoherence in the system.

Molecular sensors

The use of atoms for interesting real world applications is becoming a mature field. Sensors that use matter-wave interferometry for detecting accelerations and rotations [38] have enhanced the sensitivities of these devices over classical machines. Atomic sensors for gravitational [10], and magnetic [11] fields are by far the world's most powerful. Current work in miniaturizing atomic apparatuses may put whole instruments on a chip [39] allowing for a host of real world applications requiring less bulky

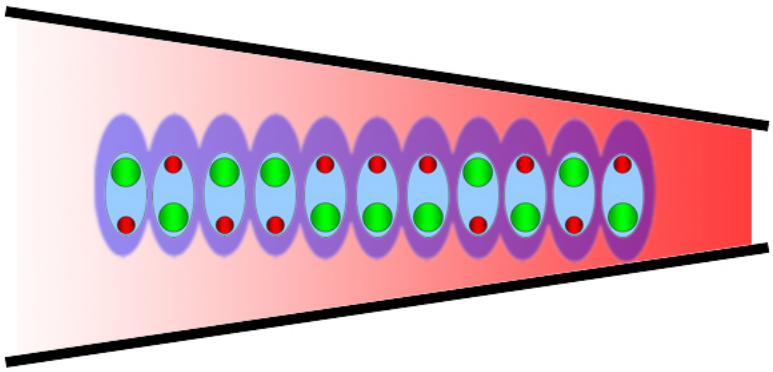

Figure 1.4: Schematic of the use of cold polar molecules for quantum computation. A 1D array of polar molecules is formed and held in an optical lattice (blue). A spatially varying electric field (red) is applied via a voltage difference to field plates (black) to allow for the individual addressability or readout of the molecules orientation. Strong dipole-dipole interactions allow for fast operation (gates) of the computer.

detectors and portability. Use of molecules would target the same goal, enhanced measurement sensitivity using unique molecular properties. Molecules may have advantages over atoms due to their ease of manipulation with electric fields [40] inside interferometers. They also may target a whole new class of sensors for electric fields (ease of polarization) or microwave fields (with their rotational structure).

1.2.4 Ultracold requirement

All of the discussed examples either benefit greatly or entirely require the use of *ultracold* polar molecules. In the first case, the cold temperatures allow better counting statistics in experiments such as precise measurements because of higher densities and slower motion (for long interrogation times, e.g. in slow beams or traps). In the latter, the novel effects simply do not appear until the molecular sample reaches a high enough phase-space density. The rough boundary for molecular Bose-Einstein condensation, for example, requires temperatures $\sim$100 nK with densities $\sim 10^{13}$ cm^{-3}.

Current sources of molecules are not even near this threshold. Therefore, in order to be able to study these wonderful topics, much progress towards making ultracold samples must be made.

1.3 Summary

The motivation to produce and study the ultracold polar molecule is clear. Whether the interest is basic science, applied science, or somewhere in between, cold molecules compel researchers to pay heed to this field. Already the promise of the cold polar molecule has lured considerable attention and investigation [41]. Hopefully, this will lead to new developments will revolutionize the field in the same way that cold atoms have.

Chapter 2

Producing cold molecules

In this chapter we review the many techniques for producing samples of ultracold polar molecules. Various comparisons between the methods are useful to ascertain their ultimate viability, giving grounds for pursuing the method. One worthwhile distinction to be made is the ultimate attainable temperature of the technique. Two distinct classes exist: one where ultracold temperatures (<1 mK) are the direct result of using atomic cooling techniques, and another where the more moderate temperatures (1 mK – 4.2 K) produced will require additional stages of cooling to study the applications mentioned in the introduction. This aside, however, since the different techniques are in various stages of development and no one technique has carved a clear path to the ultracold regime, we will content ourselves with an overview of the current situation, while mentioning any clear pros or cons of the methods.

2.1 Laser cooling

Laser cooling is the mainstay of the cold atom field, at the core of any atomic experiment. Pairs of counter-propagating lasers detuned to the red of resonance are directed at the atoms. Atomic motion Doppler-shifts the beams propagating opposite to the atomic velocity towards the blue, bringing the atom closer to resonance. Thus there is a preferential absorption of those beams. Absorption of a photon from

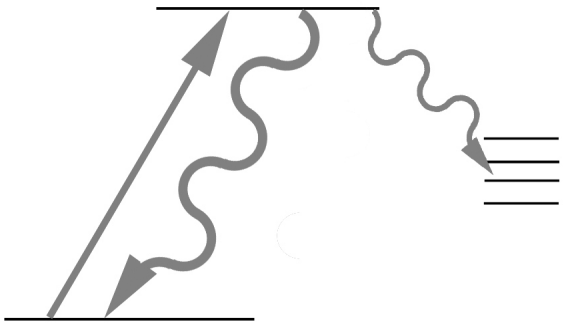

Figure 2.1: Loss from the laser cooling of a non-closed transition. Laser cooling excites atom (or molecules) from the ground state to the excited state (straight arrow). For a closed transition, the only decay (wavy arrow) is back to the ground state. The presence of other decay channels (levels to the right) presents a loss mechanism for laser cooling. The use of repump laser beams can bring atoms or molecules lost back into the cooling process. In molecules, however, the sheer number of decay channels makes laser cooling extraordinarily difficult, due to the repump requirements.

a counter-propagating beam gives the atom a momentum change opposite its motion, slowing it down. Since spontaneous emission of the excited atom is isotropic, there is no average momentum transferred to the atom from its decay. In this way the motion of the atom is slowed by repeated absorption and emission cycles.

For laser cooling to work, it is important that the absorption/emission process be closed. That is, upon emission, the atom must come back to the state it originally started in. If other final states exist for the cycle, the atom is soon lost from the system because it will no longer be in resonance with the cooling beams (see figure 2.1). In practice some small amount of leakage to other final states can be overcome with the use of 'repump' beams that optically pump the atom back into the desired state. Atoms that have been laser cooled thus have a favorable energy level structure with reasonably closed transitions. The classes of atoms that fit this requirement is pretty small: the alkalis and alkaline earths, plus a few others.

Excited molecules, due to their ro-vibrational structure, have a plethora of states

that they can decay to. It is the norm for molecules to have Franck-Condon factors (which determine the vibrational relaxation branching ratios) that allow relaxation to many states. In addition, rotational branching ratios leading to loss are always of the same order as the desired relaxation. In principle it is possible to repump all of the loss channels in a molecule to enable laser cooling, and this is being attempted [42]. Like the atomic case, it becomes critically important to choose a molecule with a favorable structure, especially those with good Franck-Condon factors, because the different, widely spaced, molecular vibrational transitions in molecules would lead to a prohibitively complex apparatus if many were involved in the decay.

2.2 Molecules from cold atoms

Direct laser cooling of molecules seems a daunting task. However, the techniques of cold atom physics work extremely well for certain individual species, that several groups are attempting to form cold polar molecules from samples of precooled atoms. The main advantages to such routes are the ability to work with familiar atomic species and techniques, and the ultimate low temperatures that they produce. Due to their complexity, however, the size of such cold samples and the apparatus to support them remain a concern.

2.2.1 Photoassociation

Photoassociation is the process whereby two atoms are bound together using light. By symmetry, a homonuclear molecule cannot be polar, i.e. charge cannot preferentially reside on just one of the (same) atoms. Thus for the formation of a polar molecule, the two atoms must be different, forming a heteronuclear molecule. This requires the precooling of two entirely separate atoms; with the associated dual species optics, atom sources, etc. Although not a herculean task, setting up two overlapping cold

atom apparatuses does set a substantial level of complexity from the start.

Once the two cold species have been brought together, the process to form ground state, trapped molecules is still quite complex. Photoassociation produces excited state molecules only when the light frequency matches a free bound-transition. The formation rate depends on things such as the two-body inelastic collision rate and the photoassociation laser intensity. Even once the photoassociation process is optimized, the molecules formed are still in the excited state. Getting a large fraction of the excited molecules into ground state is yet another step that introduces more complexity and loss processes to the system. Still, pioneering work done in our group [43] has managed to conquer these obstacles and form samples of cold ground state RbCs. Currently, work is underway to put these molecules into an optical dipole trap/lattice for the first studies of ultracold polar molecules.

2.2.2 Feshbach resonance

Similar in respects to the photoassociation method, the Feshbach resonance method starts with a dual species, cold atom setup. Here though, the association of these atoms happens by sweeping an external magnetic field through a free-bound resonance [44]. The produced molecules are thus in the electronic ground state, but the absolute highest vibrational state supported by the molecular potential. Decay and loss of this excited state is extremely rapid, so that quickly transferring to the absolute ground state will be needed to produce any substantial numbers of ultracold molecules.

2.3 Direct cold molecule production

2.3.1 Stark decelerator

The Stark decelerator is a demonstrated technique [45] that uses time varying applied fields to slow a molecular beam. The source for these detectors is a supersonic beam

expansion that produces molecules with internal temperatures and velocity distributions of roughly 1 K. For most molecules, this means that only a few of the lowest ro-vibrational levels are populated, enhancing the number in the desired ground state. During the process of expansion, the energy associated with the internal and external degrees of freedom is transferred to the forward beam direction, and large forward beam velocities result. Since the velocity and state distributions are narrow, however, it is possible to select a substantial fraction of the beam intensity and slow its forward motion in the lab frame.

In order to slow the molecules, the DC Stark effect (see section 5.1) creates a conservative potential energy hill that molecules climb to decelerate. Since the forward velocity of the molecule source is quite high (>100 m/s) and the fields' ability to decelerate is weak, multiple stages of deceleration are required. To accomplish this, the molecule beam is aimed at the field-producing electrodes. Each stage turns on as the molecule approaches the electrode and turns off as the molecules near the center of the field maximum (to prevent accelerating the molecules as they leave the field). Since the fields are conservative, this amounts to slowing and not cooling. Therefore the intensity of the slowed beam depends on the ability to stably slow a section of the original phase space of the beam. While this selection range is small, a substantial number of molecules from the input beam can be slowed. Meanwhile, the moderate temperatures and fairly low flux of molecules have prevented slowed (and subsequently trapped) molecules from reaching the phase space densities required for further cooling, either evaporative or sympathetic.

2.3.2 Laser Stark decelerator

Instead of using stages of time varying DC electric fields to slow a beam of molecules, the AC Stark effect inside a pulsed optical lattice may create the conservative potential

for molecules to climb. With high power, tightly focused beams forming the lattice, a single stage of slowing (one laser pulse) is now enough to stop a molecule from a supersonic source [46]. Here though, in contrast to the DC field decelerator, the dimensions of the required lattice (on the order of the wavelength of the slowing light), presents a serious limitation on the volume of the slowing region. In order to efficiently slow a reasonable number of molecules using this technique, the initial phase space density for loading must be very high.

2.3.3 Quadrupole filtering

Yet another technique that uses the Stark effect to produce a cold molecular beam is quadrupole filtering [47]. Essentially the same as the guide to be presented in section 5.1, this technique creates a linear potential energy minimum for polar molecules with electric quadrupole fields. This potential is used to guide the low energy molecules present in any distribution away from those who can overcome the guiding potential. Transverse energy filtering is set by the maximum guiding potentials, while longitudinal filtering is accomplished by bending the guide around a smooth corner. Longitudinally fast molecules will not experience enough centripetal force to remain in the guide, the slow ones will. Although conceptually simple, the warm (effusive oven beam) or fast (supersonic beam) velocity distribution of the sources used for quadrupole filtering severely limit the cold molecule fluxes for this technique. We note that the combination of buffer gas-cooled molecule beam and guide described in this thesis is in essence the same technique, using a much higher phase space density (cold and slow) source.

2.4 Buffer gas cooling

Yet another method for the production of ultracold molecules exists: that of buffer gas cooling. As it is distinct from the other methods and traditional atomic techniques, buffer gas cooling is a beast of its own. Favored for its high molecule production rate, this is the method for molecule production described by this thesis. Here we present an introduction and overview of the buffer gas molecular beam, its theory, and general design considerations. Specific details and construction of the apparatus are described in chapter 3, while the results and characterization of the machine reside in chapter 4.

Buffer gas cooling is a straightforward process [48]. At its heart lies a basic premise of thermodynamics: that bodies in contact with one another will proceed towards equilibrium. In buffer gas cooling, the principle source of refrigeration is thermal contact with a cryogenic gas. Thus buffer gas cooling is completely general in that it works on atoms, molecules (including free radicals), and even ions or metastable electronic states. In contrast to the other direct methods which select or slow molecules from a input distribution, buffer gas cooling is truly dissipative, cooling all degrees of freedom in the lab frame. As such, its molecule production rate is potentially very large compared to the other methods discussed. Of course, the temperature produced will be determined by the temperature of the buffer gas; cryogenic helium gas is useable down to $\sim$500 mK. Thus this method, like the others, must be used as an input source for further cooling techniques in order to reach the ultracold regime. Yet, as long as the thermal contact remains with the buffer gas, the ultimate temperature achieved will be limited. A buffer gas molecular beam solves this problem, by having a cooling region with large buffer gas densities (the buffer gas cell) and a separate region of low buffer gas densities (the beam).

The total flux of such a beam is determined by the number of molecules intro-

duced into the buffer gas cell, and the efficiency of the cooling and beam formation process. Previous buffer gas experiments [49] have shown that very large input rates are possible for a wide variety of species, and that the cooling efficiency is high. Consequently, even with a rather low beam extraction efficiency (initially expected), the resulting flux can be astoundingly high. Later in this thesis it will be shown that the beam formation process can indeed be quite efficient, leading to even larger fluxes.

A completely general, low temperature, high flux beam was the main motivation for choosing the buffer gas method to produce cold molecules. That the method is also conceptually and technically simple was also a consideration because the physics to be done with such a source is the main attraction, not the source itself. Since the ultimate goal of all cold molecule production methods, and our own goal, is the ultracold regime (<1 μK), this method certainly requires additional stages of cooling. However, going colder than 4.2 K with this technique to as a molecular source seems plausible and the current program continues in this direction.

2.4.1 Previous work

Buffer gas cooling was pioneered in the group of John Doyle at Harvard University. The first experiments concentrated on laser ablation and cooling of atomic species inside a closed buffer gas cell [49]. Subsequent expansion to molecules [50] showed that an array of molecular species could also be produced via laser ablation (given suitable precursors), and subsequently cooled. In these experiments magnetic field coils surround the cell to trap the cooled atoms or molecules via their magnetic moments. Many species have been successfully trapped in this way, as only a modest ($\sim$1 μ_b) magnetic moment is needed to trap atoms in attainable lab magnetic fields. However, further cooling to produce atoms and molecules at temperatures lower than the buffer gas temperature requires that the thermal link to the cryogenic system

must be broken. A variety of methods involving some heavy cryogenic engineering in the Doyle labs removes helium from the buffer gas cell after reaching the buffer gas temperature. This breaks the thermal link to the walls [49] and allows magnetic trapping in the buffer gas cell. This method has provided much success, yet the nature of magnetic trapping, especially in molecules (see section 5.2) has precluded these experiments from reaching the ultracold regime.

2.4.2 Molecule-buffer gas collisions

In the center of mass (CM) frame, elastic (energy conserving) collisions conserve the particles' speed, but randomizes their direction. This can be seen with the CM equations of motion,

$$m_1\mathbf{v}'_{1i} + m_2\mathbf{v}'_{2i} = 0 \tag{2.1}$$

$$m_1\mathbf{v}'_{1f} + m_2\mathbf{v}'_{2f} = 0 \tag{2.2}$$

$$m_1{\mathrm{v}'_{1i}}^2 + m_2{\mathrm{v}'_{2i}}^2 = m_1{\mathrm{v}'_{1f}}^2 + m_2{\mathrm{v}'_{2f}}^2 \tag{2.3}$$

for the center of mass velocities ($\mathbf{v}'$) and speeds (v') of particles 1 and 2 before (i) and after (f) the collision. Since the total momentum in the CM frame is zero, the momentum conservation condition separates into the first two separate constraints (equations 2.1 and 2.2). Solving for v'_{2i} and v'_{2f} gives,

$$\mathrm{v}'_{1i} = \mathrm{v}'_{1f} \tag{2.4}$$

so that the CM speed of particle 1 (and therefore particle 2) is the same before and after the collision.

This CM frame relation permits us to find the lab frame temperature change of a particle after a single collision. First we express the velocity of the center of mass in the lab frame:

$$\mathbf{V}_{CM} = \frac{m_1\mathbf{v}_{1i} + m_2\mathbf{v}_{2i}}{m_1 + m_2}, \tag{2.5}$$

where the unprimed velocities represent lab frame velocities. As the CM speed after the collision is the same as before (equation 2.4), its square can be expressed in terms of lab frame velocities and $\mathbf{V}_{CM}$:

$$\begin{aligned}
{\mathbf{v}'_{1f}}^2 &= {\mathbf{v}'_{1i}}^2 = (\mathbf{v}_{1i} - \mathbf{V}_{CM})^2 && (2.6)\\
&= {\mathbf{v}_{1i}}^2 + {\mathbf{V}_{CM}}^2 - 2\,\mathbf{v}_{1i}\cdot\mathbf{V}_{CM} && (2.7)\\
&= {\mathbf{v}_{1i}}^2 + {\mathbf{V}_{CM}}^2 - 2\,\mathbf{v}_{1i}\cdot\frac{m_1\mathbf{v}_{1i} + m_2\mathbf{v}_{2i}}{m_1+m_2} && (2.8)\\
&= \left(1 - \frac{2\,m_1}{m_1+m_2}\right){\mathbf{v}_{1i}}^2 + {\mathbf{V}_{CM}}^2 - \left(\frac{2\,m_2}{m_1+m_2}\right)\mathbf{v}_{1i}\cdot\mathbf{v}_{2i} && (2.9)
\end{aligned}$$

Because the initial particle velocities ($\mathbf{v}_{1i}$ and $\mathbf{v}_{2i}$) are random with respect to one another $\left[\langle\mathbf{v}_{1i}\cdot\mathbf{v}_{2i}\rangle = 0\right]$, the average collision yields,

$$\left\langle {\mathbf{v}'_{1f}}^2\right\rangle = \left(1 - \frac{2m_1}{m_1+m_2}\right)\left\langle {\mathbf{v}_{1i}}^2\right\rangle + \left\langle {\mathbf{V}_{CM}}^2\right\rangle \qquad (2.10)$$

Using the transformation back to the lab frame,

$$\mathbf{v}_{1f}^2 = \left(\mathbf{v}'_{1f} + \mathbf{V}_{CM}\right)^2 = {\mathbf{v}'_{1f}}^2 + {\mathbf{V}_{CM}}^2 + 2\,\mathbf{v}'_{1f}\cdot\mathbf{V}_{CM}, \qquad (2.11)$$

and noting that $\mathbf{v}'_{1f}$ is randomly oriented with respect to $\mathbf{V}_{CM}$ due to the effect of the collision so that $\left\langle\mathbf{v}'_{1f}\cdot\mathbf{V}_{CM}\right\rangle = 0$, one finds

$$\left\langle {\mathbf{v}_{1f}}^2\right\rangle = \left\langle {\mathbf{v}'_{1f}}^2\right\rangle + \left\langle {\mathbf{V}_{CM}}^2\right\rangle \qquad (2.12)$$

for the average collision.

The average temperature change $\langle T_f - T_i\rangle$ during the collision can now be found for particle 1. Using equations (2.10) and (2.12), it is,

$$\begin{aligned}
\langle T_f - T_i\rangle &= \frac{m_1}{2}\left(\left\langle {\mathbf{v}_{1f}}^2\right\rangle - \left\langle {\mathbf{v}_{1i}}^2\right\rangle\right) && (2.13)\\
&= \frac{-2\,m_1m_2}{(m_1+m_2)^2}\left(\frac{m_1}{2}\left\langle {\mathbf{v}_{1i}}^2\right\rangle - \frac{m_2}{2}\left\langle {\mathbf{v}_{2i}}^2\right\rangle\right) && (2.14)\\
&= \frac{-2\,m_1m_2}{(m_1+m_2)^2}\left(T_{1i} - T_{2i}\right), && (2.15)
\end{aligned}$$

where T_{1i} and T_{2i} are the initial temperatures of the particles.

This single-collision temperature change can be used to model a typical buffer gas cooling case, where thermalizing collisions occur between the initially hot molecule and cold buffer gas atoms. The temperature, T_N, after N collisions of a molecule of mass M colliding with buffer gas of temperature T_B and mass m_B can thus be cast into differential form:

$$\frac{dT_N}{dN} = \frac{-2\,Mm_B}{(M+m_B)^2}(T_N - T_B). \tag{2.16}$$

This equation has the simple exponential solution,

$$T_N = T_B + (T_i - T_B)\exp\left(\frac{-2\,Mm_B}{(M+m_B)^2}N\right) \tag{2.17}$$

when the initial temperature of the molecules is T_i. For an initial temperature $T_i = 1000$ K, (a typical empirically determined ablation temperature), the number of collisions to reach $T_N = 5$ K using ^{4}He buffer gas at $T_B = 4.2$ K, is $N = 100$, for SrO ($M = 103$ amu).

When considering the size of the buffer gas cell and density of buffer gas, it is important that the number of collisions between the ablation-introduced hot molecules and the cold buffer gas be sufficient to thermalize the molecule cloud before it reaches the wall of the cell. This is because any collisions with the wall will cause the molecules to be permanently attached and thereby lost. The path the molecules travel must range between the extremes of diffusive random walk and purely ballistic motion. Thus the mean distance (l_t) the molecules travel in these N collisions in order to thermalize has rough limits of,

$$\sqrt{N}\lambda_{X-He} < l_t < N\lambda_{X-He} \tag{2.18}$$

where the mean free path λ_{X-He} is the average distance between collisions between molecule X and He buffer gas. When the density of X is low enough so that X-X

collisions can be ignored, the mean free path is simply

$$\lambda_{X-He} = \frac{1}{n_{He}\sigma_{X-He}} \tag{2.19}$$

where n_{He} is the helium density and σ_{X-He} is the X-helium collision cross section. When the molecules are introduced, they are hot and heavy, with much more energy and momentum than the cold and light helium. For most of the path over which they thermalize then, they will travel ballistically rather than diffusively through the helium, and the thermalization distance will tend toward the upper limit of equation 2.18.

Most σ_{X-He} low temperature cross sections are unknown. However, the majority of those measured are near $\sigma_{X-He} = 10^{-14}$ cm^2. Hence we use this value as a reasonable estimate for σ_{X-He} to find that the range of helium densities required to thermalize SrO within 2 cm (the center of a 4 cm cell) is

$$5 \times 10^{14}\,\mathrm{cm}^{-3} < n_{He} < 5 \times 10^{15}\,\mathrm{cm}^{-3}, \tag{2.20}$$

with the expectation that the truly required value is closer to the upper limit. This is a perfectly accessible helium density; as figure 2.2 shows, the saturated density due to the vapor pressure of ^{4}He is sufficiently high for any temperature above 500 mK.

2.4.3 Extraction efficiency estimate

Static buffer gas

Modeling the cell and beam extraction aperture simply as a cubic cell of size D and a circular hole of diameter d_h can give an estimate of the molecular extraction efficiency when the density inside the cell is low. The cutoff for such behavior is taken to be when the aperture is small ($d_h < \lambda_{He-He}$), so that molecular *helium* flow conditions exist near the aperture. Here the helium density is roughly constant and unmoving over the volume of the cell.

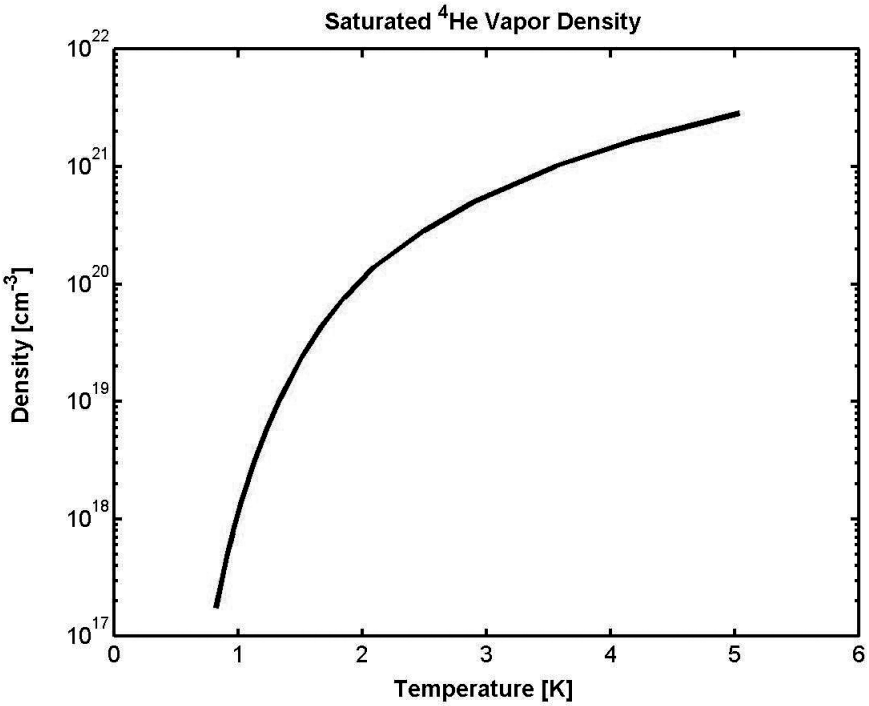

Figure 2.2: Saturated density of ^{4}He vapor versus temperature.

In this regime, we make the further simplification of *neglecting* the walls. We thus model the thermalization and extraction process *geometrically* as follows: thermalization occurs at a distance l_t (either inside the cell or at a virtual point outside the cell) and the molecules diffuse radially outward from this point (see figure 2.3). The solid angle of the aperture as seen from this point is the measure of the extraction efficiency η for thermalized molecules. If the distance from the thermalization point to the aperture is R, then the crude estimate for this solid angle is the area of the hole (A_h) to the surface area (A_R) of a sphere of radius R:

$$\eta = \frac{A_h}{A_R} = \frac{(d_h/2)^2}{4R^2}\,. \tag{2.21}$$

Expressing R in terms of the thermalization distance and cell size yields,

$$R = \sqrt{\left(\frac{D}{2}\right)^2 + \left(l_t - \frac{D}{2}\right)^2}\,. \tag{2.22}$$

As related in equation 2.19, the thermalization distance scales with helium density as $l_t \propto 1/n_{He}$. It is immediately seen that in this model, the extraction efficiency of the system scales as $\eta \sim n_{He}^2$ for low helium density ($n_{He} \ll 2N/D\sigma_{X-He}$), then rises to a maximum of $\eta \sim {d_h}^2/4D^2$ when $l_t = D/2$, and finally falls to ${d_h}^2/8D^2$ for high helium densities (when the thermalization is complete over very short distances). There is thus an optimum helium density for this geometric estimate that puts the thermalization at the center of the cell.

Of course, neglecting the effects of the walls, especially at the density limits, will severely change this result, because the molecules *will* stick to the walls. For example, at the low density limit when $l_t \gg D$, it is impossible for a large fraction of the molecules to thermalize before running into the wall and sticking. That is, the concept of a virtual thermalization point may be poor. In the high density limit, the thermalization distance is very small and the chance that the random walk motion of the diffusing molecule taking it into the initial wall can also be very high. A 1D model of this is shown in figure 2.4. In this model, the left and right walls are the ablation point and the aperture, respectively. The distance between them is the "cell" size D. All molecules thermalize in the distance l_t. If $l_t = D/2$ then the molecules have a 50% chance of reaching either wall. If $l_t = D/4$ then they have a 50% chance of making it to the middle, and thus a 25% chance of making it to the aperture. In this way if l_t is approximated by $D/2^n$, then the probability to reach the aperture is $1/2^n$. Thus

$$l_t = \frac{D}{2^n} = \frac{N}{n_{He}\sigma_{X-He}} \tag{2.23}$$

$$\eta = \frac{1}{2^n} \tag{2.24}$$

and the probability to reach the aperture in the 1D model is,

$$\eta = \frac{N}{n_{He}\sigma_{X-He}}\,. \tag{2.25}$$

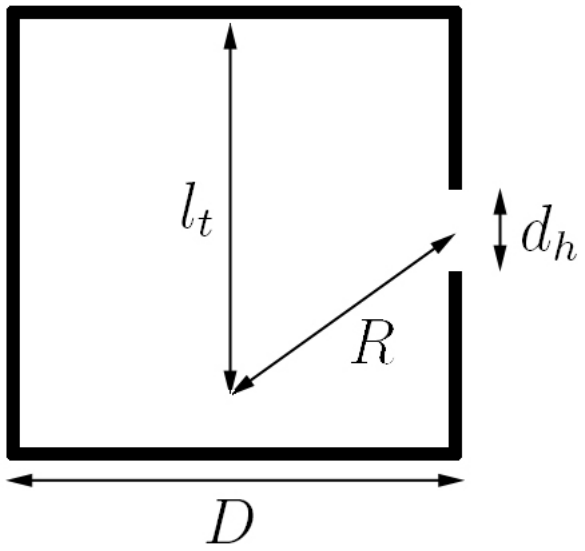

Figure 2.3: Thermalization and beam extraction model in a buffer gas cooling cell. Ablation occurs at the center of the top wall. Cell and exit hole are of dimensions D and d_h respectively. The mean distance to thermalize is l_t and the distance from this point to the hole is R. Beam extraction efficiency is the solid angle of the aperture as seen from the thermalization point.

The extraction efficiency of the 1D exercise scales as $1/n_{He}$. Although this is a 1D example, the same general idea applies to the 3D cell. We note that the true scaling may be even faster than $1/n_{He}$. Seeing as we are interested in maximizing extraction experimentally, we will vary the helium density to determine the maximum yield. This wall collision argument serves to emphasize that the range of buffer gas densities over which the beam is efficiently extracted is small. Hopefully, when we find this maximum, the extraction will be close to that of the previous *geometric* argument above. Note that for a $d_h = 3$ mm diameter hole and a $D = 5$ cm cell size, this extraction maximum is $\eta = 9 \times 10^{-4}$, a rather small fraction.

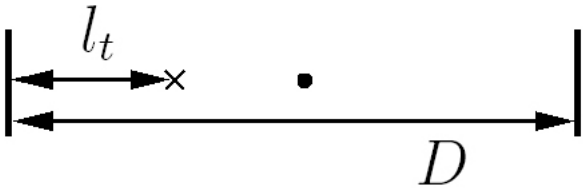

Figure 2.4: 1D beam extraction model for large buffer gas density. Ablation occurs in a 1D cell geometry between two walls separated by distance D. Thermalization of these molecules happens at length l_t (to black X). If molecules reach the center point of the cell (black circle) they have an equal chance to reach either wall. By induction, molecules that reach $D/4$ have a 25% chance of reaching the right wall.

Dynamic buffer gas

This estimate implicitly assumes that the buffer gas thermalization process occurs in a buffer gas that is static (i.e. it is moving with random thermal motion, but not in bulk). This assumption is not true in our case because the cell is steadily being emptied through the exit aperture and filled to maintain a constant density inside it. Thus there is a bulk flow from the fill towards the exit aperture (see figure 2.5). In fact, even for the previous assumption of molecular flow, the average forward (outward) velocity $v_{f,mol}$ of the exiting helium is roughly equivalent to its thermal velocity $v_{He} \equiv \sqrt{2k_BT/m_{He}}$ [51]:

$$v_{f,mol} = \frac{2}{\sqrt{\pi}}\sqrt{\frac{2k_BT}{m_{He}}} = 1.12\ v_{He}. \tag{2.26}$$

As the flow becomes more hydrodynamic, the helium velocity at the exit increases to its supersonic limit ($v_{f,ss}$) [51],

$$v_{f,ss} = \sqrt{2\gamma}\sqrt{\frac{2k_BT}{m_{He}}} = 1.83\ v_{He} \tag{2.27}$$

where $\gamma = 5/2$ in helium. The transition from molecular to hydrodynamic helium flow occurs when the diameter d_h of the aperture matches the helium mean free path λ_{He}. Inside the cell there is a bulk flow as well, although this flow occurs across a

larger area. Assuming that the density at the aperture is roughly that inside the cell (incompressible flow) we see that the ratio of mean speeds inside the cell to the aperture is the same as the ratio of the cell cross sectional area to the hole area.

The presence of this flow affects both the thermalization and beam formation process. During thermalization collisions, the presence of the flow tends to drag the molecules toward the hole, leading to an enhanced extraction efficiency. During beam formation, the collisions resulting upon exit from the hole will tend to drag the heavy and slow molecules to the helium speed. Although the latter was expected, the former was not. Both will be discussed when the results are presented, in chapter 4.

2.4.4 Simulation of the cooling process

Monte Carlo simulations of the buffer gas cooling process are performed to determine the dynamics of the in-cell buffer gas cooling. In a matlab routine, individual molecules are followed as they undergo collisions with cold helium atoms. Molecule-molecule interactions are assumed to be small due to their low density. To begin following a molecule, its random speed and angle are chosen from an input Maxwell-Boltzmann distribution at large (1000 K) temperature, and a cosine distribution relative to the normal of the target, respectively. This empirically approximates the introduction of the molecule via ablation. Next, the molecule is propagated a randomly chosen length from a distribution describing the free path (λ_{X-He}) of the molecule in some (fixed) density of helium and helium-X cross section. Then to elastically collide the molecule with the helium, a random velocity from a 4.2 K helium distribution is chosen. After transforming into the colliding center of mass frame, random deflection angles are chosen, and the result is transformed back into the lab frame. At every collision molecules are tracked by recording their position and velocity, and the time of the collision. Molecules are followed as the collision process

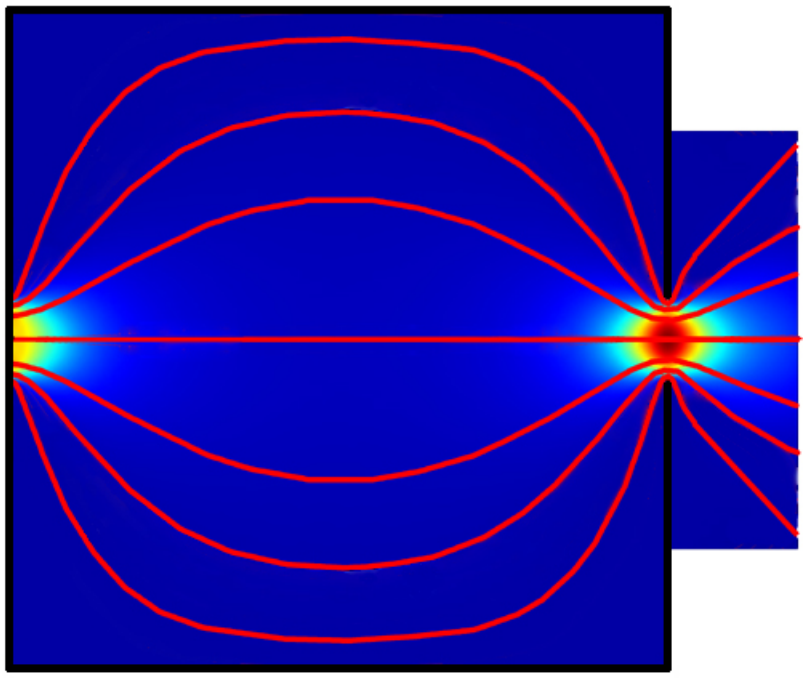

Figure 2.5: Streamlines and flow speed in a buffer gas cell (outlined in black). Streamlines are shown in red, flow speed as the color background. Calculations were made using finite element methods with a simplified 2D cylindrical cell geometry (diameter and length $D = 5$ cm, $d_h = 3$ mm) and with the assumption of incompressible, laminar flow (valid even for a compressible gas when the Mach number $M < .3$) [52]. The helium gas is taken to be at 4.2 K with density $n_{He} = 10^{15}$ cm^{-3}.

continues in this way until one of the pre-selected following thresholds occurs: the molecule's RMS velocity dips below that of the RMS for its 4.2 K distribution, or the molecule encounters a wall of the buffer gas cell.

Due to the large number of collision steps required, and the number of computations and random number generations in each step, the number of molecules that can be tracked is limited. In addition, since the buffer gas motion neither in the cell, nor at the hole are included in the model, this simulation serves more to affirm the in-cell thermalization conditions in the regime of low buffer gas flow. This flow can be included in a model for future simulations by adding the bulk flow at the collision point to the random helium velocity before each collision event.

2.4.5 Choosing a molecule: SrO

When beginning the experiment to produce a buffer gas-cooled beam of molecules, several technical and fundamental considerations were made prior to the selection of a molecule with which to proceed. Many diatomics were considered, and although the full list of diatomic molecules, considering all of their properties, is a very large parameter space, the molecule SrO and it attributes quickly proved to be the most promising. It is interesting to note that since buffer gas cooling is a general process, as aforementioned, the technical advantages play a larger part in the production and analysis of the buffer gas beam. However, the particulars of the SrO molecular constants should also add to its desired use in further work towards the ultracold regime. Its favorable qualities, listed in a rough order of perceived importance when the decision was made are as follows:

• Strontium Oxide has an 8.9 Debye dipole moment (see table 2.1). This moment determines the size of interaction within an applied electric field. When molecules are trapped with applied fields, a large dipole moment yields large maximum trap

depths for a physically realizable field. This is a key feature when looking to both guide and trap using either static or AC electric fields. The large dipole moment also leads to large dipole-dipole interactions when the molecules are polarized. This gives the advantage of fast collision times for efficient thermalization during evaporative cooling. Large dipole-dipole interactions are also integral to many of the interesting cold molecule applications that drive the motivation for these experiments.

• SrO has a simple rigid rotor structure ($^1\Sigma$ molecular ground state), no hyperfine structure, and known spectroscopy [53] with a convenient electronic transition at an optical wavelength of 785 nm (see table 2.2). This obviates the need for spectroscopic studies, simplifies the interpretation of absorption and fluorescence detection, and makes the use of easily available atomic rubidium optics (at 785 nm) possible. This technical advantage allows the experiment to proceed directly to the study of the buffer gas cooling and beam process with a single borrowed diode laser.

• SrO is a stable, commercially available compound. Results from other laser ablation and buffer gas cooling experiments suggest that direct laser ablation of a stable precursor will result in sizeable (10^{12}) yield of the desired diatomic molecule.

• SrO does not admit two body chemical reactions with itself (see table 2.3), nor (by general chemical considerations) with the alkalis Cs and Rb. This is important when considering building up large densities of molecules inside a trap. If two-body chemical reactions are energetically allowed, then loss mechanisms may be uncontrollably large. Reactions with the alkalis are considered because overlapping a trapped sample of molecules with cold atoms may be a viable route to cooling beyond 4.2 K using sympathetic cooling with laser cooled atoms.

• SrO has a ground rotational constant B_e of .338 cm^{-1}, leading to a $J = 0 \rightarrow J = 1$ rotational splitting of 20.1 GHz. This microwave transition is convenient both for manipulation of rotational levels and for trapping using microwave fields.

d	8.9 Debye	[54]
B_e	.338 cm^{-1}	[23]
ground state	$^1\Sigma$	[23]
Isotopes	^{86}Sr 10% I=0	[54]
	^{87}Sr 7% I=9/2	[54]
	^{88}Sr 83% I=0	[54]

Table 2.1: Overview of SrO molecular properties: dipole moment d, rotational constant B_e, ground molecular structure, and Sr natural isotopic abundance with nuclear spin I.

v′/v″	0	1	2	3	4
0	.283(920)	.412(978)	.236(1043)	.063(1117)	.008(1201)
1	.317(870)	.015(922)	.173(980)	.317(1044)	.148(1118)
2	.212(826)	.067(872)	.131(924)	.024(985)	.285(1045)
3	.109(786)	.163(828)	<.001	.151(925)	.002
4	.047(751)	.154(789)	.059(831)	.040(876)	.101(927)

Table 2.2: Franck-Condon factors in the SrO $X^1\Sigma\, v'' \Leftrightarrow A^1\Sigma v'$ transition [55] and the approximate wavelength (nm, in parentheses) of the band origins [53].

20 GHz is especially conveniently situated at the edge of the microwave K and Ku bands, allowing a range of standard microwave technologies (including high power amplifiers) to be employed.

SrO bond	426kJ/mol	[54]
O_2 bond	498kJ/mol	[54]
Sr_2 bond	16kJ/mol	[54]
Sr-O_2 bond	<251kJ/mol	[56]
	2SrO + 103 kJ/mol $\Leftrightarrow$ SrO_2 + Sr	
	2SrO + 338 kJ/mol $\Leftrightarrow$ O_2 + Sr_2	

Table 2.3: Overview of SrO two body reactions.

Chapter 3

Experimental apparatus

This chapter details the construction of the buffer gas beam apparatus. The building of this machine began at the outset of this thesis when the ideas, goals and outlines for producing ultracold polar molecules were fleshed out. Even though work continues on the buffer gas beam design, a description of the current setup provides considerable insight into the design-build-repeat process that went into this experiment. Hopefully this chapter can aid those taking up work on this apparatus as well as those who wish to build a buffer gas molecular beam of their own. The desire is that the pitfalls encountered can be avoided in the future with the experiences gleaned to date, while the current knowledge and state of the setup will facilitate future improvements in the apparatus and its use for experiments utilizing buffer gas molecular beams.

The broad outline of the buffer gas molecular beam is shown schematically in figure 3.1. The apparatus consists of a vacuum chamber and pump system to maintain high vacuum, a liquid helium cryostat for the production of low temperatures, an ablation laser setup for the introduction of gaseous molecules, a buffer gas cell for the precooling of molecules and creation of the molecular beam, and an optical detection system for the probing of in-cell cooling and molecular extraction processes. The development, workings, status, and future prospects for each of these subsystem elements will be traced in the following sections.

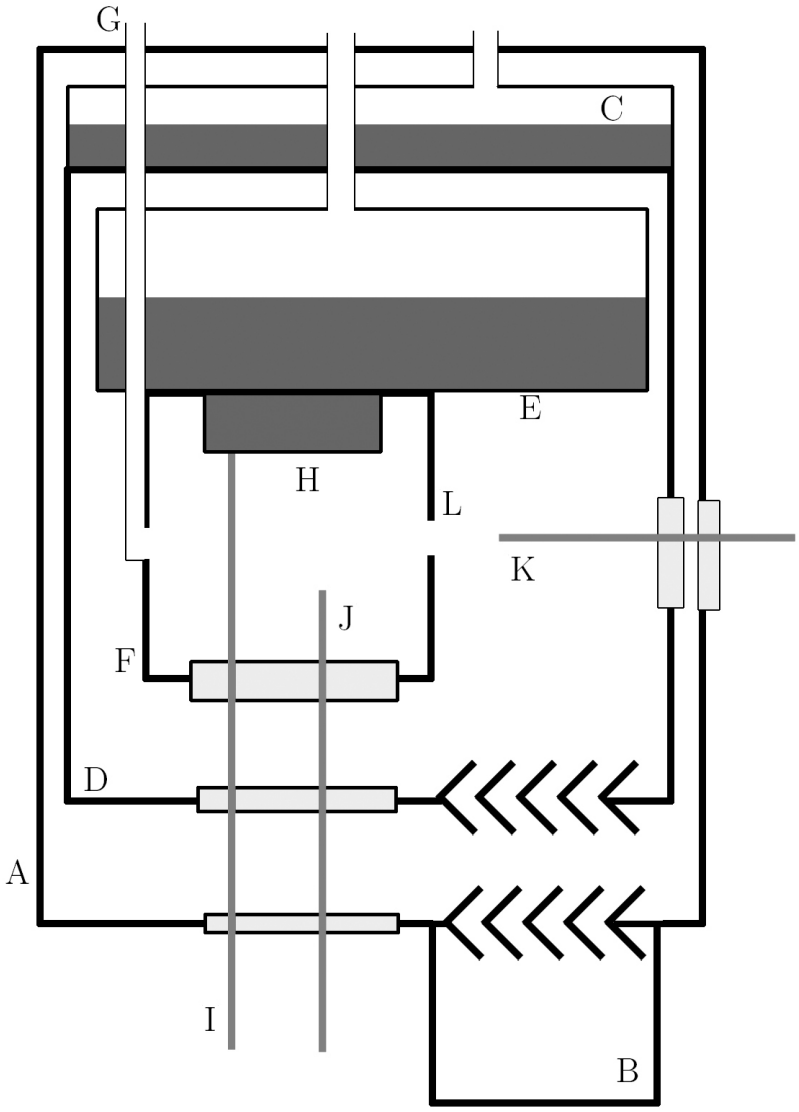

Figure 3.1: Broad outline of the buffer gas beam apparatus. A vacuum chamber (A) and vacuum pump (B) provide vacuum conditions for a custom cryostat. The cryostat consists of a liquid nitrogen (C) cooled shield (D) and a liquid helium cold plate (E). A buffer gas cell (F) is filled with helium gas with a fill line (G). A molecular precursor (H) placed in the cell is ablated with a high power YAG laser beam (I). The thermalized molecules are detected either via laser absorption in the cell (J) or via laser induced fluorescence in the beam (K) formed by the aperture (L).

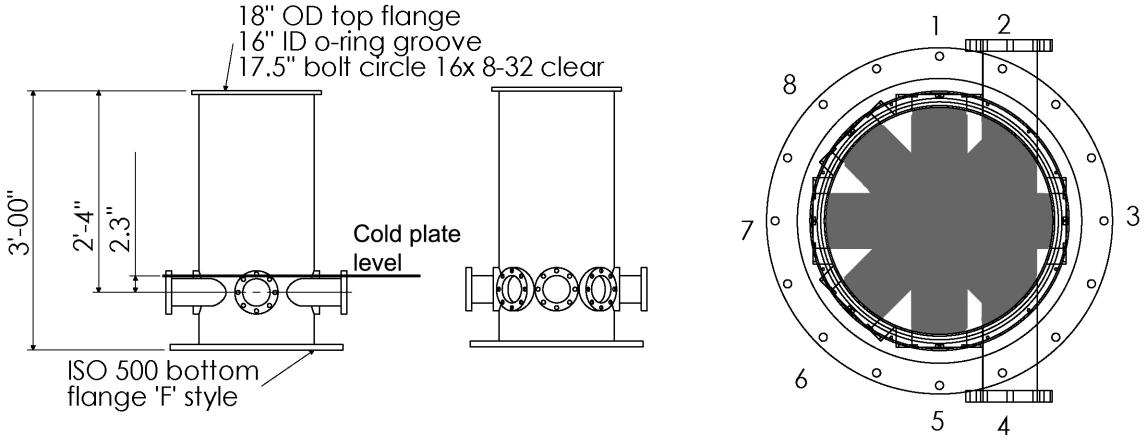

Figure 3.2: Mechanical drawings of the experimental chamber. Left two drawings are side views and indicate measurements involving chamber top, the center of the viewports and cold plate level. The right drawing is top-down showing the arrangement of the eight viewports, and their unobstructed optical access in grey.

3.1 Vacuum assembly

3.1.1 Vacuum chamber

The vacuum chamber is a custom designed stainless steel shell designed to accommodate the liquid helium cryostat described below. A mechanical drawing of the chamber is shown in figure 3.2. The top flange pattern attaches to the cryostat, sealing to it with an o-ring that rests in a grove in the vacuum chamber. The bottom flange is an ISO500-claw-clamped flange that mates to the supporting structure and diffusion pump. Most of the upper part of the chamber volume houses the large cryostat volume. The volume below the level of the cryostat cold plate is designed to be nine inches in height, allowing for the placement of the buffer gas cell and other experimental pieces.

In order to maximize optical access to the buffer gas cell region, a total of eight large area flanges are placed around the circumference of the chamber. Six of these

flanges point radially toward the center of the chamber and two are offset parallel to allow optical access along a molecular beam propagated through the chamber. Each of these flanges is a standard six inch conflat flange with a four inch bore tube. The central height of these flanges is offset 2.3 inches beneath the level of the cold plate.

All flanges, including those attached to the cryostat, to the support structure, and to the conflat blanks and windows, were fitted to the chamber using Viton o-ring seals providing adequate vacuum tightness to the rated ultimate pressure of the vacuum pumps. For the conflat flanges, attachment hardware is silver-plated and cro-moly (lubricant) coated in order to minimize seizing to the poorly tapped MDC-made flanges. Even with this preventative protection, the conflat hardware should be finger tightened during assembly and then re-finger-tightened after pumpdown has compressed the Viton gasket. If a copper gasket is desired (e.g. in mounting heavy equipment), then careful examination of which bolt holes to use should be taken or the chamber should be retapped.

3.1.2 Vacuum viewports

Vacuum viewport (part VP-601) flanges were purchased from Huntington Vacuum for optical access through the six inch conflat flanges. These large viewports quickly fogged in the center of the window (see figure 3.3) when the cryostat nitrogen shield was brought to liquid nitrogen temperatures. This fogging occurs because the window cools below the dew point of the air in the lab. The mechanism for this cooling is blackbody emission from the window onto the nitrogen shield and the 77 K window behind it. The thinness of the window, its large area, and the poor thermal conductivity of the glass ensures that the center of the window cools substantially as it loses heat via blackbody emission. The edges of the window do not fog; they are in direct thermal contact with the flange attachment, which is near room temperature.

Elimination of the fogging on the viewports may be achieved in many ways. Utilizing thicker windows can enhance the thermal conductivity to the edges. Direct heating can also keep the windows warm. Furthermore, use of smaller windows both decreases the blackbody loss and the distance from the window center to the edges (keeping the center warmer). Of course, smaller windows limit the optical access through the viewport. However, when access was not a concern this was the preferred choice. When full access over the large viewport window is needed, however, yet another method is employed (see figure 3.3). It is possible to attach high reflectivity aluminum foil to the viewport, forming a slit of optical access. Since the foil is a much poorer blackbody emitter than the glass, cooling due to this process is greatly reduced in the covered areas. In addition to the vacuum viewport, the nitrogen shield window is partially covered. Also, a matching foil slit can be placed half-way in between the windows. Covering the unused portion of the nitrogen window makes it a poorer blackbody absorber (i.e. reflecting more power back to the viewport) and placing the slit (anchored to the room temperature chamber) in between the windows limits the solid angle of cold surface that to which warm window is exposed.

3.1.3 Support structure

The support structure for the buffer gas beam experiment is rather substantial due to the size and weight of the vacuum chamber, liquid helium cryostat, and diffusion pump. A rough guide for its design supports several hundred pounds for the cryostat and chamber, over 400 lbs for the diffusion pump and two (2) two-hundred pound students standing on the structure. 80/20 Inc. double-wide 15 series (3 inch square) aluminum extrusion was used exclusively to accommodate this roughly 1000 lbs of design weight. As shown in figure 3.4 there are six vertical posts bearing the load to the ground. Resting on horizontal cross beams are two, one inch thick aluminum

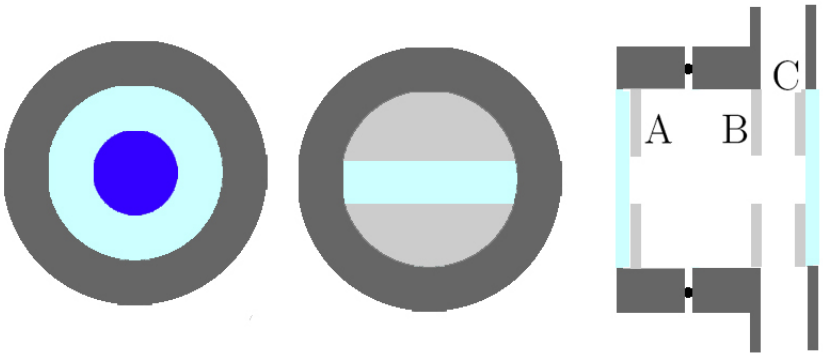

Figure 3.3: Vacuum viewport fogging problem and solution. Left: untreated large area vacuum viewports fogged (dark blue) in the center of the glass area (light blue) due to blackbody cooling. Center: limiting the optical access by placing metal foil (gray) behind the glass prevented the fogging. Right: side view showing foil behind the vacuum viewport glass (A), at the vacuum camber diameter to limit solid angle (B), and covering the nitrogen shield windows (C). Foils (A) and (B) are at the chamber (room temperature) but emit less blackbody radiation than glass due to their high emissivity. Foil (B) limits the solid angle of 77 K surface to which the glass is exposed. Foil (C) reflects blackbody radiation back to the warm surfaces.

plates, one for operation of the experiment and another working inside the cryostat.

The experimental plate has a 19.75 inch bore in its center and 32 tapped M12 holes matching the dimensions of ISO-500, a standard flange. 16 of the tapped holes are used for mounting the diffusion pump from below. The plate height is placed such that the diffusion pump is suspended one inch from the ground to avoid scorching the floor. Into the remaining holes on the top plate, multi-coolant baffles are mounted, and the vacuum chamber is mounted in turn to these baffles. The second plate is a platform for working underneath the vacuum chamber during assembly. This plate, at roughly three feet high, also has a large bore in the center. Resting the vacuum chamber on this piece allows safe work from below when lying on a mechanics' creeper underneath the structure.

It quickly became clear that the assembly and disassembly of the vacuum structure was an arduous task. Of great assistance was the installation of a one-ton hand chain

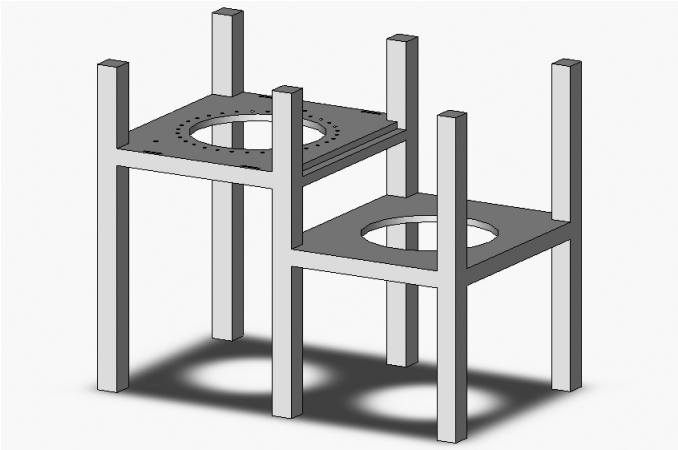

Figure 3.4: Drawing of the experimental chamber support structure. Two large aluminum plates rest on a frame made of 15 series 8020. On the left the higher plate suspends the diffusion pump and holds the chamber (both not shown) when running the experiment. On the right the lower plate safely holds the chamber when working from below.

hoist, suspended from the ceiling of the lab. Mounted as near to the ceiling as possible, this made it possible to lift the cryostat out of the vacuum chamber, when modifying the nitrogen shield or any area other than the cold plate. This hoist can be rolled on its trolley linearly along an aluminum I-beam allowing easy placement of the cryostat onto the work plate. Disassembly and especially positioning during reassembly eased considerably with the ability to precisely position the chamber before lowering it onto the experimental plate.

3.1.4 Vacuum pumping system

The vacuum pump subsection of the assembly consists of three main components: the backing pump, the diffusion pump, and the cooled baffles. Three main considerations drive the vacuum system requirements: the throughput, pumping speed and ultimate pressure. A large diffusion pump is the obvious choice when large throughput and pumping speeds are required, and ultimate pressures are less of a concern. Our choice (Edwards HT16), approximately matches the bore of the diffusion pump to

the diameter of the vacuum chamber. Roughly limited by the conductance of its bore, the pumping speed of this large pump is 7200 l/s for helium gas. Combined with a maximum throughput about an order of magnitude larger than any load we expect to introduce, and a large critical backing pressure, this choice has proved quite robust and straightforward to use.

For the characterization of the beam formation, especially near the aperture, moderate pressures can be tolerated because they should not disturb the beam dynamics over such a short range. However, in detecting or guiding the beam away from the aperture, the issue of ultimate pressure in the molecular beam region has become a concern. Ideally, the vacuum surrounding the cell is as low as possible. Practically, it should be below the level where collisions can occur along the length we wish to propagate the molecular beam. If we desire a nominal mean free path (length of guide) of 30 cm, this corresponds to a density in the vacuum region surrounding the cell of below 3.3×10^{12} cm^{-3} (assuming the standard 10^{-14} cm^2 cross section). This represents a room temperature helium pressure of 10^{-4} Torr. However, at the largest helium throughput (2.5 Torr l/s) applied over the course of characterizing the buffer gas beam, the diffusion pump is only specified to achieve a pressure of $\sim 5 \times 10^{-4}$ Torr, measured at the inlet to the pump, already at the pressure limit we wish to avoid.

In addition, in order to prevent backstreaming of pump oil into the chamber and also to limit direct blackbody radiation from the pump onto cold surfaces, it is necessary to place water cooled baffles (figure 3.9) between the pump and the cryostat. Along with these baffles, the essential 77 K nitrogen shield between the warm chamber and cold plate also impedes the helium gas traversing the vacuum towards the pump. Another set of baffles is placed here in order to allow gas to escape and prevent blackbody radiation from overwhelming the cryostat. These obstacles reduce the

effective pumping speed at the center of the cryostat [52].

The base pressure p_B inside the cryostat with a gas flow through the buffer cell of $\dot{Q}_{in}$ can be estimated using the equations

$$p_B = \frac{\dot{Q}_{in}}{S}, \tag{3.1}$$

$$S = \frac{1}{\frac{1}{S_0} + \frac{1}{C_1} + \frac{1}{C_2}}. \tag{3.2}$$

Equation 3.2 relates that the conductances of the baffles C_1 and C_2 add in parallel with the diffusion pumping speed S_0 to form the effective speed S. For the water cooled baffles, the specified conductance is $C_1 = 7000$ l/s, and for the similar nitrogen baffles, simply scaling by the ratio of areas gives $C_2 = 2000$ l/s. For a maximum flow through the buffer gas cell of 2.5 Torr l/s, the (300K equivalent) pressure inside the cyrostat is 2×10^{-3} Torr, a level too high to sustain even a free (unguided) molecular beam any substantial distance. The solution to this problem is the addition of cyropumping charcoal attached directly to the cold plate along with differential pumping stages.

3.1.5 Charcoal sorb

It turns out that charcoal, when held at cryogenic temperatures, is a fantastic cryopump [57] even for helium gas. Due to the large internal surface area of the charcoal connected by tiny holes, an atom impacting the outer surface is transported inward and has a near unit probabity of "sticking" (i.e. being cryopumped). Hence the effective pumping speed of a charcoal sorb is purely geometry limited. For example, if the source of a vacuum leak (such as our beam) is directed at a charcoal-coated surface, then to a good approximation, the beam sticks to the sorb and is pumped away. Any charcoal not directly facing the beam adds capacity, but not augmented pumping speed. In this way it is seen that the calculation of a true pumping speed, and ultimate dewar vacuum, is difficult due to large geometric variability. However, the use of this cryopump is clearly superior to the use the diffusion pump because the

charcoal can be placed directly where the pumping is needed (outside the exit of the cell) and avoids the need for baffles.

Experimentally, the addition of the charcoal sorb is a significant improvement. First, we see that it dramatically increases the pumping speed of the system. When charcoal is used, even without the diffusion pump, the highest gas flows (2.5 Torr l/s) through the buffer cell only produce a pressure change of roughly 10^{-7} Torr reading on a gauge that is located on the outer chamber. With only the diffusion pump, the pressure rises substantially, as discussed above, causing a poor enough guard vacuum to rapidly boil off liquid helium.

3.2 Cryogenics

The application of cryogenic techniques to atomic physics experiments is rare, especially since non-equilibrium techniques such as laser and evaporative cooling work so effectively. However, since many other fields employ low temperature methods to directly cool their apparatuses, these techniques are well developed and mature. Since the complexity of the cryogenic apparatus grows as the ultimate temperature desired decreases, we employed the minimalist design philosophy of reaching liquid helium temperatures. This allows for the use of liquid helium itself as the cooling agent, and a simple fill cryostat as the cold bath. Although the task of designing and building such an apparatus has been called simple so far, to an inexperienced *atomic* physicist it has not been. Thus we begin this section with a brief review of the basic design considerations for blackbody radiation, thermal conductivity, and contractions. This will allow critiques of the custom designed cryostat and the other low temperature components later in the chapter.

3.2.1 Blackbody radiation

Proper design of any cryogenic experiment accounts for thermal loads and the transfer of heat between components. One source of heat on a cryogenic system is blackbody radiation from the warmer surfaces surrounding it [58]. All bodies radiate power P from their surface area A at a rate that depends on the temperature T and emissivity ϵ of their surface, according to the formula

$$P = \epsilon \, \sigma A \, T^4, \tag{3.3}$$

where σ is the Stefan-Boltzman constant ($\sigma = 5.67 \times 10^{-8}$ W/m^{2}K^4). When two surfaces are at different temperatures, there is a heat link between them due to the emission of radiation from the warm surface being absorbed at the cold surface. Further, when the radiation of the cold surface can be neglected (a good assumption for 4 K versus 77 K surfaces, and also 77 K versus 300 K) the heat link can be described as the warm surface with emissivity ϵ_1 and area A_1 filling all modes with radiation intensity of $I = \epsilon_1 \sigma \, {T_1}^4$. At the cold surface, with emissivity ϵ_2, since emissivity is the same as absorbtivity, the cold surface will absorb a power per unit area of

$$\frac{P}{\delta A} = \epsilon_2 \, \epsilon_1 \, \sigma A \, {T_1}^4. \tag{3.4}$$

Corrections to this relation can be complex, depending on the geometry of the apparatus, but equation 3.4 is typically a good estimate. Characteristic emissivities for different materials can range from 0.01 to 0.1 for a clean metal surface, to 0.7 to 0.9 for a dirty, oily, or painted metal surface or glass [59]. Hence, shiny metal surfaces must be used whenever possible to minimize the values of ϵ. Also, care must be taken to keep surfaces clean (from diffusion pump oil, for example) to reduce black body losses.

When optical access is needed, windows that transmit at the desired optical wave-

length, yet absorb the 300 K blackbody emission are essential. At 300 K, the peak of the blackbody spectrum is near 10 μm. Many optical materials can be used at $\lambda < 1\,\mu$m while being absorptive at 10 μm. We use BK7 glass almost exclusively due to its low cost and easy availability.

3.2.2 Thermal conductivity

Another source of heat transfer that directly affects the design and performance of a cryogenic system is direct thermal contact. The 1D (z direction) heat equation [60]

$$\dot{Q} = -\kappa(T)\frac{\partial T}{\partial z} \tag{3.5}$$

governs the heat transfer $\dot{Q}$ for temperature $T(z)$ and temperature dependent thermal conductivity κ . Many calculations of heat transfer can be simplified to the specific situation where the ends of the material are held at constant temperatures T_1 and T_2, and the material is of constant cross section A. This is usually the case for any object anchored at two different temperatures. Also, for objects anchored at one end and subjected to a constant heat load applied to the other end, the load can be determined with a temperature measurement of the floating end. With length l between the fixed (either by design or measurement) ends, the heat load from one end of the piece to the other is simply [58]

$$\dot{Q} = \frac{A}{l}\int_{T_1}^{T_2} \kappa(T)dT. \tag{3.6}$$

The material dependent thermal conductivity integral between $T_1 = 0$ K and $T_2 = 300$ K (essentially the same as 4 K to 300 K) for materials held in contact with room temperature at one end and liquid helium at the other, and between $T_1 = 0$ K and $T_2 = 77$ K for liquid nitrogen and helium is given in table 3.1. The best thermal conductors are easily seen to be OFHC copper and aluminum (physically lighter than copper). These materials should be used wherever cold temperatures need to be maintained.

Material	0 to 300 K	0 to 77 K
Copper (OFHC)	1620	690
Aluminum (99% pure)	730	220
Copper (standard)	460	54
Brass	170	20
Stainless steel	30	3.2
G10	1.5	0.17
Nylon	0.8	0.13

Table 3.1: Thermal conductivity integrals ($\int_{T_1}^{T_2} \kappa(T)dT$) in several materials in units of W/cm [61].

In addition to the use of high conductivity materials for maintaining good thermal contact, it is important that good *physical* contact is made whenever two pieces are held together, in order to conduct heat from one piece to the next. Preparation of polished flat surfaces is the first step to ensure that gaps do not exist between the two pieces. Direct contact alone between these, however, can still be a relatively poor thermal conductor thus a coupling compound should usually be placed between the surfaces to address this. Surprisingly, as seen in figure 3.5, application of a *thin* layer of Apiezon-N grease has the best performance for making good thermal contact between cryogenic objects, much better than direct contact.

3.2.3 Thermal contractions

The vast majority of materials, when cooled, undergo a change in their length. Length changes resulting from the use of different materials, or from points cooled to different temperatures can misalign parts, loosen or tighten joints, and even break materials such as glass if one is not careful. The thermal linear expansion $\Delta L/L$, relative to room temperature, for some materials is reproduced in table 3.2 for 4 K and 77 K temperatures.

One important application of this knowledge to proper cryogenic design is to the construction of joints. Quite generally, construction of a joint that will tighten (or

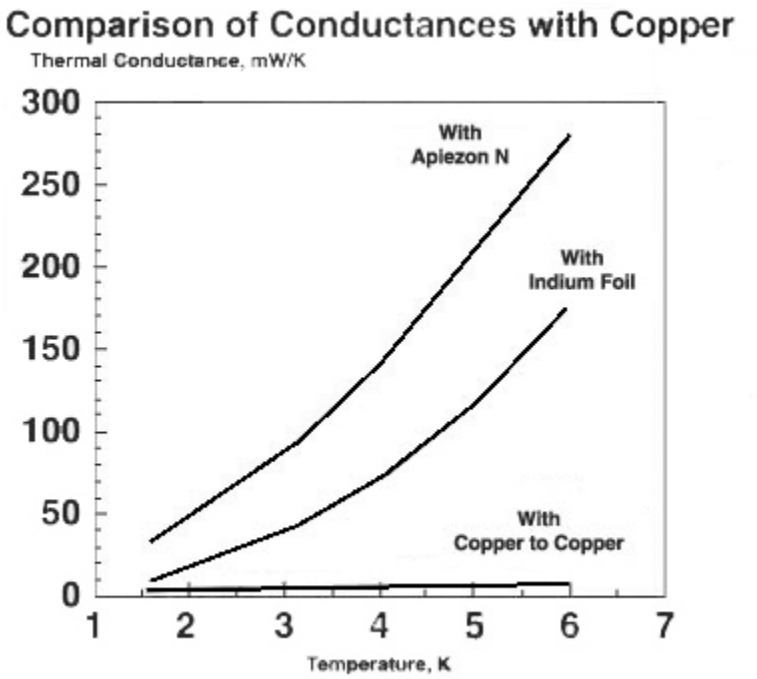

Figure 3.5: Thermal conductance of copper metallic joint with various coupling compounds [62].

Material	$\Delta L/L$ [%] 4 K	$\Delta L/L$ [%] 77 K
Copper	.324	.302
Aluminum	.415	.393
Brass	.384	.353
Stainless steel	.297	.279
Titanium	.151	.143
Glass	.055	.054
Nylon	1.389	1.256

Table 3.2: Thermal expansion $\Delta L/L = (L_T - L_{293})/L_{293}$ (in percent) of several materials at T =4 K and 77 K [58].

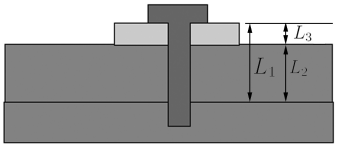

Figure 3.6: Construction of a cryogenic joint. Two pieces are joined together with a bolt and washer. All three have different coefficients of thermal expansion. If the change in part length ΔL_1 matches that of the bolt plus washer $\Delta L_2 + \Delta L_3$ the joint will remain at the same tightness when cooled.

at least not loosen) as it cools provides for better contact and rigidity. Ways to do this include using a bolt that matches the sample material, or alternatively, another material that contracts more than the sample being bolted. If securing copper, for instance, brass screws are an option. The problem with this example, though, is that brass irreversibly stretches under stress, resulting in loose screws during the next cool down. Ideally stainless steel screws are used, as they are sufficiently elastic that they do not show this behavior.

In general, the way to construct a joint that tightens when the bolt contracts less than the sample is to use a washer that contracts less than both (like titanium). For the situation shown in figure 3.6, it is easy to see that the joint will be stable (not loosen nor tighten) when the proper washer length is chosen from the calculation below.

$$\Delta L_1 = \Delta L_2 + \Delta L_3 \tag{3.7}$$

$$L_2 = \frac{L_3\left(\frac{\Delta L_3}{L_3} - \frac{\Delta L_1}{L_1}\right)}{\left(\frac{\Delta L_1}{L_1} - \frac{\Delta L_2}{L_2}\right)} \tag{3.8}$$

If the washer coefficient of thermal contraction is less than the bolt, and its length is greater than this value, the joint will actually tighten. Considerations like this are important whenever good thermal contact is desired (tightening joint) or fragile components are being joined (stable joint).

3.2.4 Cryostat design

The liquid helium cryostat was custom designed in conjunction with IRlabs Inc. based on their HDL14 cryostat. Design criteria for the cryostat included a long liquid helium hold time, a helium gas inlet and a large cold plate experimental surface. The outline schematic and mechanical drawing of the result is shown in figures 3.7 and 3.8. It consisted of a 36.4 liter liquid helium vessel, 14 inches in diameter. Included in the helium dewar design are two fill ports, originally to be used for fill and vent. Above the helium vessel is the 8.49 liter nitrogen bath, and its single inlet. At the top of the dewar are a safety rupture disk to prevent over-pressurization of the vacuum chamber, an electrical connector for the temperature sensors and a helium gas inlet. The inlet brings the gas into the vacuum region, first spiralling around the nitrogen bath to precool the gas to 77 K, then poking through the liquid vessel to bring the line down to the helium cold plate. Connections between points anchored at different temperatures are made using flexible metal bellows to increase the thermal conduction path length in these parts. The cold plate has 4-40 tapped holes on a half-inch grid for mounting experimental pieces such as the buffer gas cell. Other special modifications designed into our cryostat include lifting lugs for hoisting, a long (for IRlabs) work height between the cold plate and nitrogen shield, a split in the nitrogen shield for ease of disassembly, and a stand on top for handling the dewar.

Once received, learning the nuances, quirks and drawbacks of this particular dewar took some time. It is clear that even working with an experienced company, custom cryogenic design is a challenging process. The modifications post delivery, as well as dealings with the dewar's less than desirable characteristics will be discussed in the following sections.

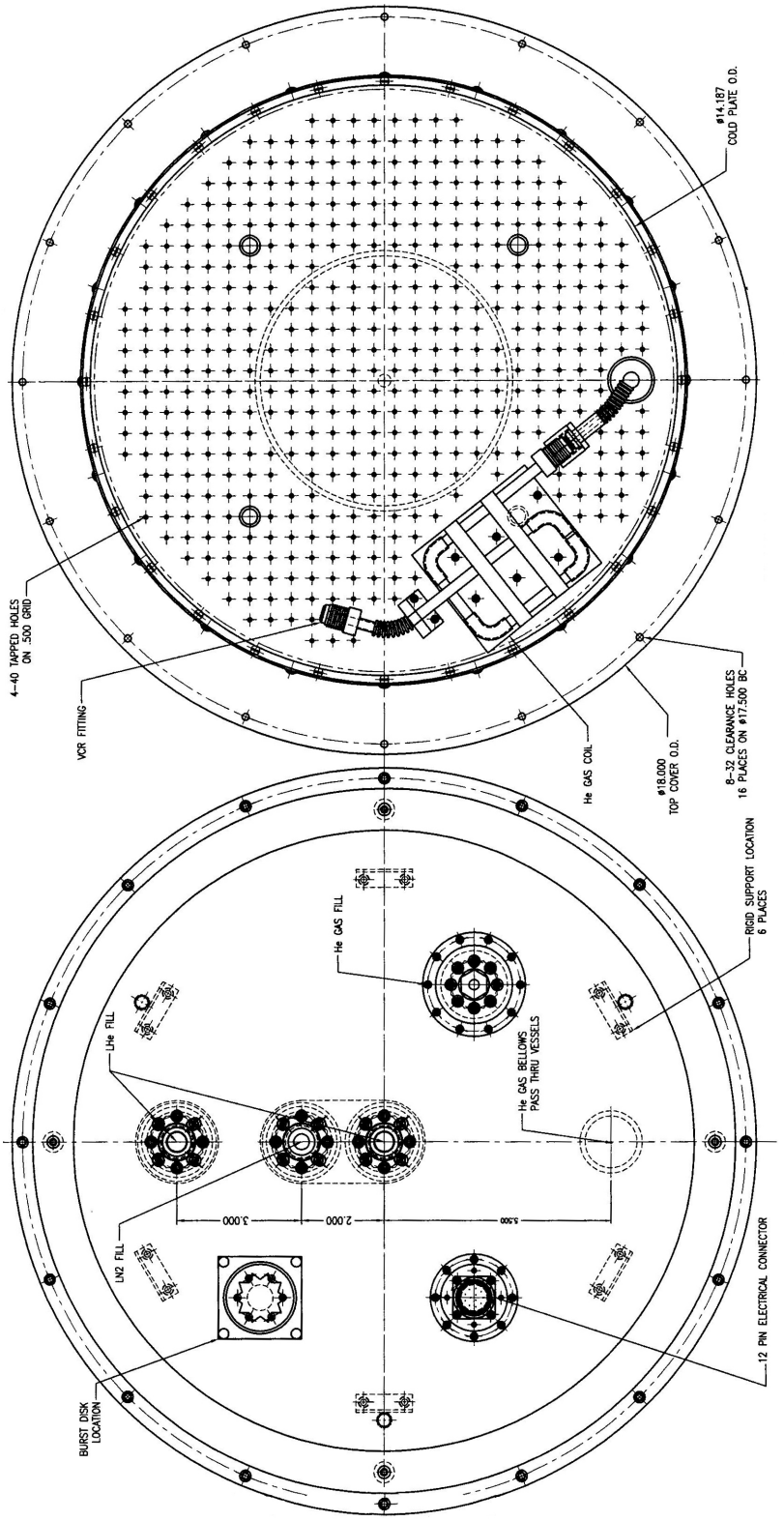

Figure 3.7: Mechanical drawing of cryostat top and bottom views.

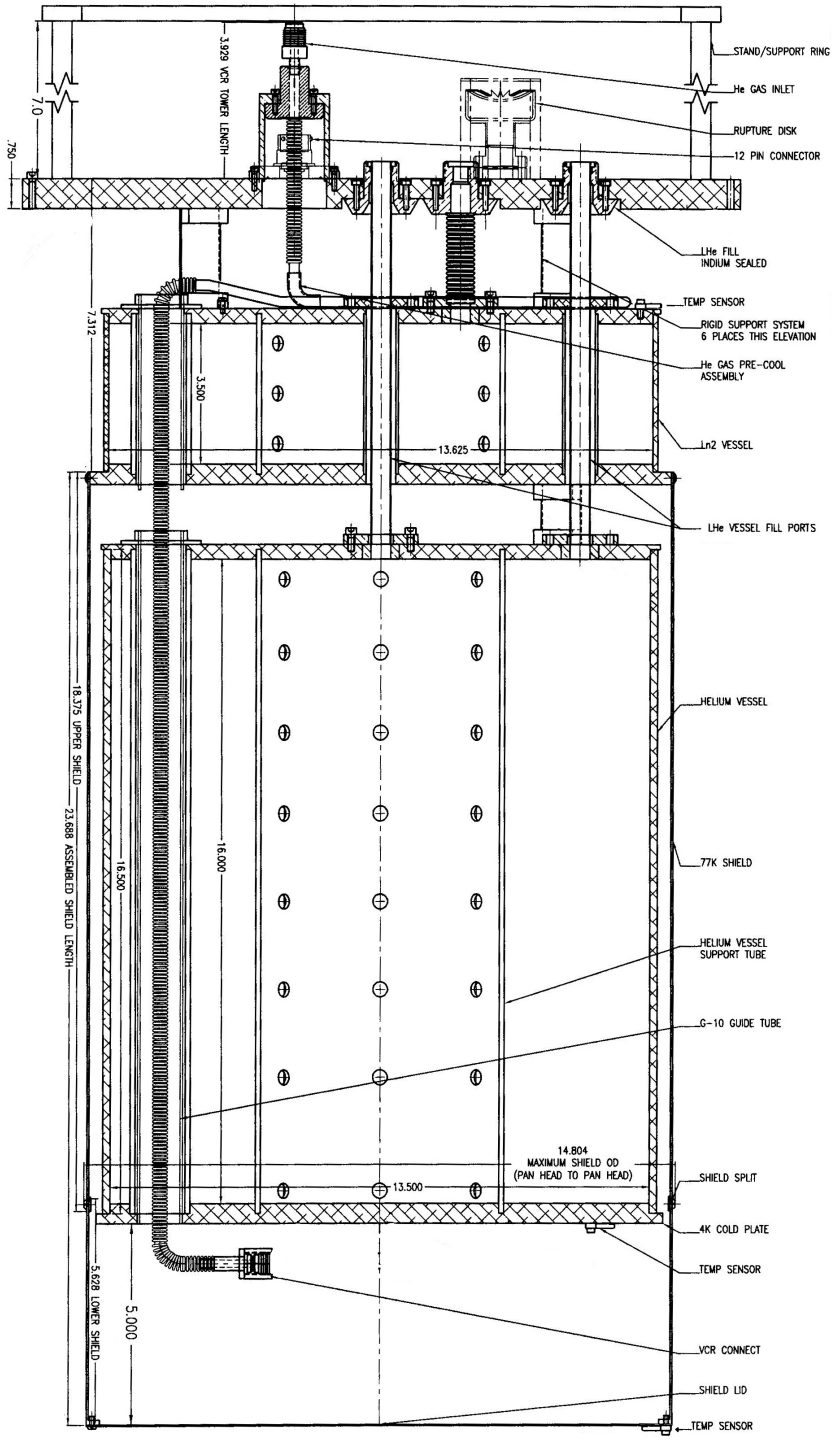

Figure 3.8: Mechanical drawing of cryostat, side view.

3.2.5 Nitrogen shield and bath

The nitrogen shield is a high-purity aluminum cylinder 23.7 inches long, 14.5 inch diameter, and 0.05 inch thick. It is attached to the bottom of a 5.3 inch deep cylindrical bath of the same diameter with a volume of 8.5 liters. Its purpose is to block room temperature blackbody radiation emitted from the walls of the vacuum chamber from reaching the 4 K cold surfaces. Ideally this intermediate surface is kept as cold as possible so that it radiates less onto the surfaces inside. Thus the liquid nitrogen bath's existence is to provide the cooling for this shield. When tested before prior to shipment, this filled vessel had a hold time of 23 hours. Of course, modifications for experimental use increased the heat load on the nitrogen shield substantially. Optical access windows have an emissivity near 1, compared with roughly 0.01 for clean aluminum, increasing the blackbody load on the shield. Another blackbody load is the blackened baffle (c.f. section 3.2.6) covering 90 inch^2 of the bottom plate.

With the three (3) three inch (3") diameter windows and the blackened baffle, the temperature as measured at the bottom of the plate is ∼150 K and the hold time of the nitrogen bath is ∼4 hours. Part of the decreased hold time is due to the extra heat load, and the rest is due to a lack of a convenient way to fill the nitrogen bath. Apparently, IRLabs' dewars are meant to be nitrogen filled via gravity, with a funnel. Given that the top of our dewar is 10 feet off of the ground, this is a very inconvenient method. Filling via a direct connection to the nitrogen storage dewar thus gives at most a 50% fill. This is because the single fill port, coupled with the squat dimensions of the nitrogen bath, causes too much turbulence during the fill process.

The increased temperature and reduced nitrogen hold time however, are major problems. Because surfaces radiate power as T^4 and $(150/77)^4 = 14$, the warmer shield increases the heat load on the helium dramatically. In addition, when the nitrogen runs out, the shield quickly warms and the (expensive) helium quickly boils

off. One improvement alleviating these problems is the covering of the unused portion of the windows as described in section 3.1.2. This reduces the temperature at the bottom to roughly 110 K and increases the nitrogen hold time to about 6 hours. To ameliorate the hold time issue, a computer controlled automatic fill was put into place.

The autofill program samples the temperature at the top of the liquid nitrogen bath (with the topmost thermometer shown in figure 3.8) in order to determine when to fill. When the bath contains liquid, the temperature at this point remains near 77 K. When the temperature there rises above 80 K, the computer determines the bath is empty. By opening a TTL controlled solenoid it begins filling the bath. For 15 minutes the fill continues regardless of temperature. At the end of this period the solenoid closes immediately when the temperature drops below 80 K. As long as the flow from the nitrogen storage dewar is properly set (by the storage dewar's hand valve) the 15 minutes will constitute an entire (50%) fill. Thus the nitrogen hold time issue is now effectively solved, with the caveat that the hand setting of the fill rate is touchy. If the fill rate is too fast, a 15 min auto-fill will spill lots of liquid nitrogen over the top of the dewar and onto the floor. This inevitably forms a thick layer of ice on the top of the dewar. If the fill rate is too slow, it is possible that no liquid will accumulate in the dewar and the shield will continue to warm.

While the autofill solves the hold time bother, the issue of the 110 K temperature of the shield persists, presenting an additional heat load on the helium. Solutions to this problem involve bringing more cooling power to the bottom of the nitrogen shield. This can be done by thickening the shield, or running copper braids from top to the bottom, or even flowing liquid nitrogen through a tube wrapped around the shield. Presently, with a base temperature of 110 K, none of these solutions have been deemed absolutely necessary. However, if the dewar is to be operated below 4 K (e.g.

by pumping on the helium) removal of this heat load may become a requirement.

3.2.6 Optical baffles

Owing to the T^4 dependance of the black body radiation, all direct lines of sight for far infrared radiation (IR) from room temperature surfaces onto the 4 K areas were eliminated. Optical access for the visible and near IR are not issues as windows that transmit these wavelengths and absorb the far IR (like BK7) exist and are used on intermediately cooled surfaces. Direct physical access is more of a problem because it necessitates *not* putting a surface where access is needed. Passing of the blackbody radiation to the cold areas is then a large problem that must be avoided. Using a painted baffle as shown in figure 3.9 does a fairly good job at solving this issue. The baffles are "optically opaque" in the sense that any photon incident upon them must strike at least two surfaces before making it through the baffle. Normal radiation shields have high emissivity in order to minimize their blackbody emission, however, using shiny metal surfaces for the baffle would simply reflect the room temperature blackbody off its surface into the cold area. Painting only the surfaces facing the cold area black [61] absorbs this room temperature blackbody, at the expense of increased heat load on the baffle (and the entire nitrogen shield). Areas facing the high temperature are left shiny to reflect some of the blackbody radiation from those areas. The increased heat load on the shield raises its temperature, yet this solution is still a net win. It turns out [63] that painting the entire baffle presents such a load on the 77 K that more than counteracts the drop in transmitted blackbody. This is also found in our setup, by experimentation with various levels and placement of painted baffle surfaces. In this way, painting the baffle can increase the helium hold time more than a full day.

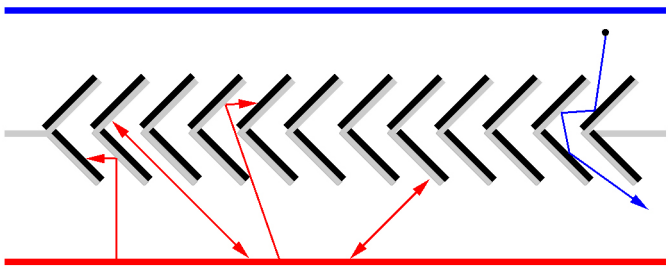

Figure 3.9: Schematic of nitrogen cooled baffles. The Baffles are placed between room temperature surfaces (red) and 4K cold surfaces (blue) and are held in contact with the 77 K nitrogen shield. The baffles are dense, meaning they do not allow a direct line of sight from one side to the other. Blackbody radiation from the hot surfaces (red arrows) is either absorbed on the painted (black) surfaces of the chevron or reflected from the shiny surfaces (gray). Painting the baffles as shown prevents the room temperature blackbody from reflecting into the cold areas, but presents a smaller heat load onto the 77 K than painting the entire baffle. A gas atom is free to traverse the baffle (blue arrow) and escape the cold region.

3.2.7 Cooling down

Beginning an experimental run starts with the cooling of the cryostat. Prior to filling, high vacuum ($<10^{-3}$ Torr) is obtained with the diffusion pump to break convective thermal contact between the 300 K, 77 K, and 4 K sections of the dewar, and to prevent condensation and icing. Once vacuum is achieved, "pre-cooling" can commence. Pre-cooling consists of using liquid nitrogen to cool the helium bath to 77 K. This is performed because the relative cost and cooling power of the liquids [58] makes using liquid nitrogen to cool to 77 K much more efficient. Once the helium bath is pre-cooled the nitrogen bath can be filled and the autofill system turned on. This process typically takes 2–3 hours. Waiting for the temperature at the bottom of the nitrogen shield to reach its terminal temperature ($\sim$110 K) takes about 6 hours, warrenting that the pre-cool operation ideally be conducted the night before the actual fill of liquid helium.

In order to fill with liquid helium its bath must be completely devoid of liquid

nitrogen (the nitrogen will freeze above 4.2 K). This is accomplished by blowing compressed helium or nitrogen gas through the bath space until the temperature rises above 80 K. Next, the vacuum jacketed transfer line is prepared by inserting the proper end into the liquid helium storage dewar, with all valves closed to build up pressure in the storage dewar. To precool the transfer line, the valve on the transfer line is opened while the other end is outside the helium bath until nitrogen from the air starts to condense on the surface. Then this the end is placed inside the dewar, lifted slightly from the bottom. Maintaining roughly 3 PSI inside the helium dewar by backfilling through the vent port with helium gas allows the fill to proceed at a sufficient pace and provides the energy needed to actually lift the liquid into the chamber. Experience shows that a proper fill rate puts the 77–4 K cooling time at 30 minutes (2 K/min), and the time to fill at another 30 minutes (5% /min). The proper rate can be checked by monitoring the temperature and fill sensors, and also by ensuring that the plume of cold gas leaving the fill port roughly reaches the ceiling (currently the top of the dewar is 10 feet from the ceiling).

Transfer from a 60 liter helium dewar fills roughly 85-90% of the dewar. Filling is complete when the helium in the dewar, as measured by the level meter, begins to drop, indicating that the storage dewar is empty. Immediate removal of the fill line is then prudent to prevent losing more of the transferred liquid. Transfer from a 100 liter dewar results in a 100% fill with enough left over for a 50% fill some days later (on the second fill the transfer line should be precooled even more than previously described to avoid reheating the dewar with warm gas).

3.3 Buffer gas cell

The buffer gas cell is a rather simple design. A cube with five open faces has its closed face bolted to the cold plate for thermal contact to 4.2 K. The cube is made of the

purest copper (alloy 101) to ensure high thermal conductivity. Interchangeable face pieces can be placed differently depending on the desired cell configuration. They each serve a different purpose:

- Hold the SrO
- He gas inlet
- Aperture (beam hole)
- Windows (for YAG or detection lasers)
- Blank face
- Combination of the above

Many different cell configurations were investigated; the two main layouts of use are shown in figure 3.10. The main difference between the two is their use for in-cell characterization via absorption, or out-of-cell beam characterization via fluorescence. The reason for the two different setups is that the fluorescence detection is very sensitive to YAG laser scatter and to the ablation plume. Use of the cell in figure 3.10 (a), which is optimized for absorption detection, collection of beam fluorescence also collects large amounts of light passing through the front window/aperture. Using a blank with a hole drilled in it for the aperture, as in figure 3.10 (b), blocks this light, and prevents the fluorescence detection from being swamped.

In addition to the various setups, different sizes of cell and aperture can be used to optimize the beam extraction efficiency. The first cell used in this study is a 7 cm sided cube fabricated from brass. The second cell size tried is a 3 cm sided cube of alloy 101 copper. Design changes incorporated into the second cell make it easier to use and colder. For example, the large cell always read a temperature 5.5-6 K at the point furthest from the cold plate. The small cell is made of a better thermal

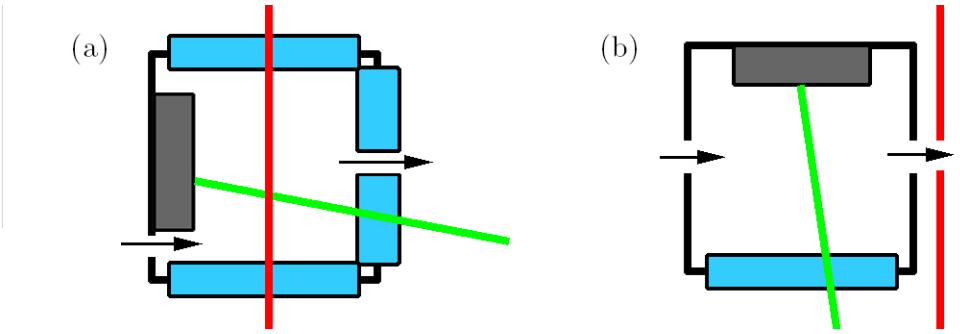

Figure 3.10: Configurations of the buffer gas cell. (a) shows the setup used for in-cell absorption characterization. Here, the ablation beam (green) passes through a window (blue) that also serves as the beam aperture (outward arrow), and strikes the SrO (gray) on the opposite wall. Helium enters (inward arrow) near the SrO target. The absorption probe beam (red) passes through the cell via two windows. (b) shows the setup used for molecular beam fluorescence measurements. Here the aperture is a thin blank with a hole drilled in it, and the probe laser beam passes outside of the cell.

conductor and utilizes tightening joints. In addition all bolt holes in the copper utilize stainless helicoil inserts which allows for sufficient tightening during assembly and cooldown contractions without deforming the screw threads (which does happen in the brass cell). With these changes the small copper cell reads under 4.5 K at the point furthest from the cold plate. The vacuum seals on the faces of the small cell are made using flat-to-flat contacts with a little apiezon-N grease in between parts, simplifying construction greatly. The large cell uses indium seals everywhere components ere mated. Since the aperture is such a large leak on its own, any flat-to-flat leaks in the small cell are trivial.

3.3.1 He gas inlet

Removal of the IRlabs manufactured 4 K gas precooling device (figure 3.7 'He GAS COIL') is necessary because it is too bulky and does not provide enough movement flexibility. After several design modifications, the new 4 K precooling device provides 4 K gas to the cell. The first design consists of direct attachment of the gas line

to the cell. This resulted in too large a heat load on the cell, keeping the bottom of the cell above 15 K. The second design brings the gas line to refrigerator tubing wrapped around a brass bobbin and then connects to the cell. This also performs poorly, because the conductivity of the brass and copper alloy does not allow it to provide enough cooling power to the flowing gas. The third design uses copper alloy 101 for both the bobbin and tubing. With this in place, immediately the in-cell molecule temperature characterizations plummeted to near 4.2 K. This demonstrates the necessity of using high quality materials for key parts.

3.3.2 Cell density determination

Determining the density of helium gas inside the cell can be tricky. First, since gas is compressible, and pressure and temperature gradients are bound to exist, the density cannot be strictly constant across the cell. Conservation of mass, though, implies that in steady state we can at least determine the flow through the cell (and aperture), as long as no other leaks besides the aperture are present. The assumption that the aperture presents a much greater constriction than the cell is certainly true; thus for low to moderate flow rates, the density should be fairly even over the cross section of the cell.

Helium flow rate

The flow rate through the cell is controlled by varying the upstream pressure from a controlled leak into the cell fill line. To calibrate this flow, a known volume is placed after the leak and pumped down to very low pressures. Upon valving off the pump, the pressure in the volume rises due to the leak. By monitoring this pressure increase, the leak rate into the volume can be determined. In order to take this measurement, we ensure that the pressure drop across the leak remains large for its duration, thus allowing us both to fit the pressure increase to a linear rise, and to stay within the

calibrated range (<10 Torr He) of the pressure gauges.

Cell density

Once the flow rate is known, the cell density can be inferred, given that the flow near the aperture is approximately the molecular case. There the vacuum conductance C of the circular aperture is,

$$C_a = 3.64\,[\mathrm{l/s}]\,A[\mathrm{cm}^2]\,\alpha\sqrt{\frac{T\,[\mathrm{K}]}{M\,[\mathrm{AMU}]}} \tag{3.9}$$

when the gas is temperature T and mass M, and aperture has area A and transmission probability α for a finite thickness aperture [52]. The input flow rate Q_{in} has dimensions of power, and is determined at room temperature. It can be related to the low temperature flow Q_{out} via the law of mass conservation (or, equivalently, the number $\dot{N}$ of atoms that cross the aperture each second) by,

$$\frac{Q_{\mathrm{in}}}{k_B T_{\mathrm{in}}} = \dot{N} \tag{3.10}$$

$$\frac{Q_{\mathrm{out}}}{k_B T_{\mathrm{out}}} = \dot{N} = \frac{C_a P_{\mathrm{cell}}}{k_B T_{\mathrm{out}}}\,, \tag{3.11}$$

where P_{cell} is the pressure inside the buffer gas cell. The density in the cell n_{Cold} is thus

$$n_{\mathrm{cell}} = \frac{Q_{\mathrm{in}}}{T_{\mathrm{in}} C_a k_B}\,, \tag{3.12}$$

where the ideal gas law $P_{\mathrm{cell}} = n_{\mathrm{cell}} k_B T_{\mathrm{out}}$ eliminates pressure from the equation. For convenience, the Boltzmann constant can be written in practical units as $k_B = 1.04 \times 10^{-19}$ Torr cm^3/K. By varying the cell density and aperture size, the required flow rate varies over roughly 3 orders of magnitude; hence a few different calibrated leaks to control the flow are required. In addition, at the largest input flow rates (with the largest aperture sizes), the output flow is no longer in the pure molecular flow regime but rather transitions toward the continuum flow. Under these conditions,

equation 3.9 is no longer valid. In this regime, the true conductance of the aperture is difficult to calculate, and equation 3.12 only provides a lower bound. The density limit for the full continuum flow regime is the upper bound and is roughly a factor of two larger [52].

3.4 Ablation laser setup

Ablation is performed with a pulsed Nd:YAG laser (Big Sky Laser CFR200). The output of the YAG is a 9 ns, 30 mJ pulse at 1064 nm. A doubling crystal in the unit allows roughly 50% conversion from the fundamental to 532 nm. High power dielectric mirrors, and (anti-reflection coated) windows and lenses steer and focus both of the wavelengths onto the ablation target inside the buffer gas cell. High quality optics and anti-reflection coatings are necessary for the protection from damage due to the large laser intensity. Special care must be taken to ensure that the optics remain clean, as a dirty surface damages much more easily. This is somewhat unavoidable for the window surface that faces the ablation target, due to the dust the ablation creates. Periodic cleaning (and less frequent changing since damage is inevitable) of this window is a practice performed every few data runs.

Since the ablation beam has both a vertical path and a path at eye level, we choose to leave a small tracer of the green (532 nm) among a predominately fundamental (1064 nm) beam. This choice is mostly for safety reasons, since there is no evidence that molecule production is enhanced by one wavelength over the other. Leaving a green tracer allows for alignment by eye (the fundamental is invisible to the eye) at low power by increasing the delay between the flashlamp and Q-switch. At full power, safety goggles can provide complete protection at 1064 nm without severely obstructing vision. Additional safety features such as beam stops, enclosures and curtains also help to keep the ablation beam contained.

The ablation process produces molecules (and atoms, and ions, and clusters, and dust...) when focused down to a spot on the ablation target. Although conceptually simple, laser ablation is one of the "dark arts" of science. Of our many attempts to characterize the ablation process, not many conclusions can be made. The naive expectation is that for the target area there exists some threshold intensity above which ablation can occur. With this thought in mind, the spot size on the target and the laser power per pulse are varied with the goal of increasing the molecular yield. Although the laser can be reduced to roughly 30% power before some sort of lower ablation threshold is reached, adjusting the spot size of the beam does not confirm the expected behavior. That is, when power variation suggests that the spot size can be increased for better yield, this does not happen. For a tight focus, and near to it, varying the size has roughly no effect. When the spot becomes too large though, there is a cutoff in the molecular yield. One possible explanation for this is the presence of some sort of "drilling", or ablation depth whose amount varies as the intensity changes. Here, the threshold can be the onset of the drilling, and when the intensity is too low no ablation occurs.

We observe definitively that something is physically changing the surface of the target, and "drilling" is as accurate as any word to describe its effects. Clearly, on each shot of the laser, some material leaves the surface, leaving behind a divot. If the ablation laser fires repeatedly at the same point, the damage to the surface resembles a hole. Two very important effects then limit the production of molecules when the laser fires. The first is the delay between shots impinging upon the same part of the target. To get full production this delay must be very long, on the order of a second. Any faster rate causes the yield to substantially ($\gg 50\%$) drop for pulses after the first. Perhaps this is due to some sort of localized heating, or melting even, of the target point that frustrates the ablation process for further quick shots. The second

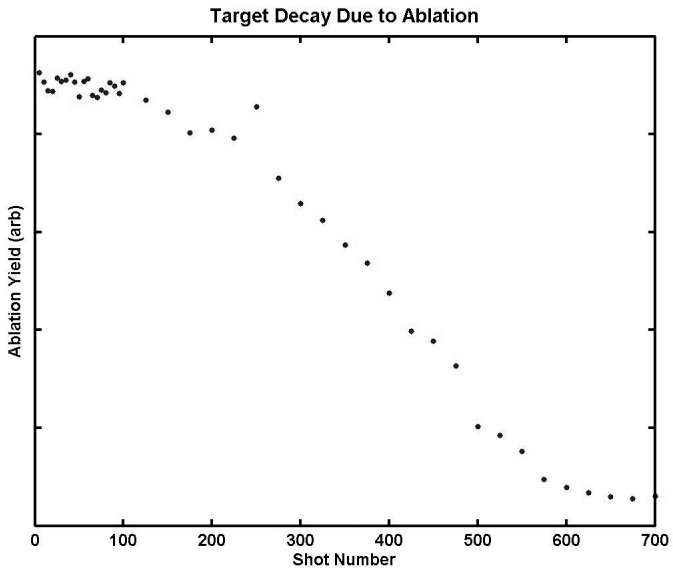

Figure 3.11: Ablation yield for repeated ablation of the same target point. A fresh spot produces the greatest yield. The successive ablation shots have a yield roughly the same size. After a slow decay in the yield during the next 500 shots, roughly 1% of the yield remains, for many shots.

effect is the deterioration of the target surface. Under a wide variety of laser powers and beam spot sizes, as long as the threshold is reached, damage to the surface follows the same pattern. For roughly 300 ablation pulses on a fresh surface of the target, the yield is roughly constant and is the highest for that point (see figure 3.11). During the next roughly 500 pulses there is a slow decay of the yield to roughly 1% of maximum. After these 1000 shots the 1% yield lasts for many many shots.

Since we wish to increase the flux of the molecule beam by ablating many times in quick succession, it is important to move the YAG beam to different spots between ablation shots. Also, since the damage to the surface builds over a number of shots, movement of the YAG has the potential to wear the surface more evenly, resulting in a more efficient use of the target. To this end, a linear motor actuator is placed in one of the beam steering mirror mounts. When a linear sawtooth pattern on this actuator is applied, the spot on the target also moves roughly in this pattern. Such a linear raster

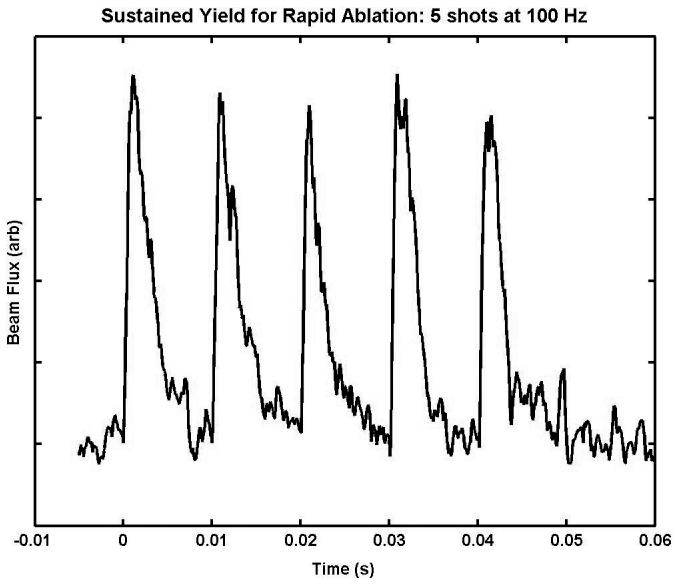

Figure 3.12: Molecule flux as a function of time for a quick series (100Hz rate) of 5 ablation pulses. Molecule number is a function of the area under the curve. Here the experimental conditions produce clearly separated pulses of roughly equal yield at a high (100Hz) repetition rate. Larger buffer gas densities can produce longer molecular pulses whose yields overlap, yet total flux still adds. This data was taken while the YAG ablation beam was rastered, taking roughly 5 seconds to cover roughly 1 cm of the SrO target.

totally alleviates the need for a delay between ablation shots, for repetition rates up to 100Hz, which is the maximum rate of our YAG (see figure 3.12). In addition, as expected, the total number of ablation shots that give the full yield, until a "trench" is dug on the surface of the target, increases with the raster length.

3.5 Detection laser setup

3.5.1 Diode laser

The laser used for detection of the molecules is an external-grating tunable diode laser (Sacher Lasertechnik TEC500) in the Littman configuration. This configuration specularly reflects the output of an anti-reflection coated laser diode off a holographic grating to produce an output pointing stability that is independent of laser frequency.

The first-order diffracted beam is retroreflected back into the diode to provide the feedback cavity for the laser. The cavity mirror is placed on a pivot adjusted by a piezo-electric actuator to allow for tuning of the laser frequency. The main advantage of the Littman configuration is that it allows for greater amounts of mode-hop free frequency tuning, crucial for monitoring many separated molecular rotational lines. We get roughly 20 mW of laser power from the Sacher laser, insufficient for our experimental and locking requirements; the laser is amplified via injection locking of a high power (100 mW) antireflection-coated diode.

3.5.2 AOM setup

One important element in the optical setup is the acousto-optic modulator (AOM). An AOM has the ability to change the frequency, direction, and intensity of a laser beam passing through it. It does this by coupling a radio-frequency (RF) drive into a crystal, setting up a density grating inside, off of which the laser can Bragg scatter if the correct angle between the beam and crystal is set. The first order upshifted (downshifted) beam has its frequency increased (decreased) by the RF frequency. Changing the frequency of the RF alters the periodicity of the grating, thereby changing the frequency of the light shift, the Bragg scattering angle and the amplitude of the density grating. The efficiency of the AOM is coupled to proper Bragg alignment, to the size of the density grating, and to the coupling of the RF power into the crystal. These non-ideal effects are important when the AOM is used to modulate the frequency of a light beam in time.

One way to reduce the changes in AOM diffraction efficiency as the RF frequency changes is to use a short focal length lens focused onto the AOM crystal. A beam with a tight focus is the natural opposite to a collimated beam; the collimated beam has only one propagating wavevector, whereas the beam with a tight focus has a large

angular spread. Although use of a tightly focused beam reduces the AOM efficiency (less of the beam will match the Bragg angle with the crystal), it adds versatility by allowing different angular components to diffract when the RF frequency is changed.

Another way to reduce the non-ideal coupling of the AOM frequency to the amplitude of the diffracted beam is to operate the AOM in a double-pass arrangement. As shown schematically in figure 3.13, linearly polarized laser light enters the system through a polarizing beam splitter and passes through a short 1:1 telescope, at the focus of which is the AOM crystal. A quarter-wave plate and retroreflecting mirror reverse the direction of light, and rotate its polarization by 90 degrees, passing it back through the telescope and out the other port of the beam splitter. Irises serve to block the undeflected portions of the beam. In this double pass configuration, twice the light frequency shift is obtained for a given change in the RF frequency. Also, the telescope and mirror exactly retroreflect the beam regardless of the diffraction angle, since a set of beams with different diffraction angles is converted to a parallel set of beams all normal to the retroreflection mirror.

Aside from frequency modulation the AOM is also used for optical switching. When the RF drive is on, the beam is diffracted; when off, the beam passes straight through the crystal. To switch a beam this spatial steering of is directed through a small aperture, or into an optical fiber, allowing only the diffracted beam to pass on to the experiment. Since the AOM can be turned on and off relatively fast, this setup can be used to intensity-modulate a beam for lock in detection.

3.6 Locking the laser frequency

Data taking sessions with our molecular beams, require frequency-stable lasers in order to detect the molecules via absorption or induced fluorescence spectroscopy. In general all experiments with atoms and molecules require stable lasers for detection,

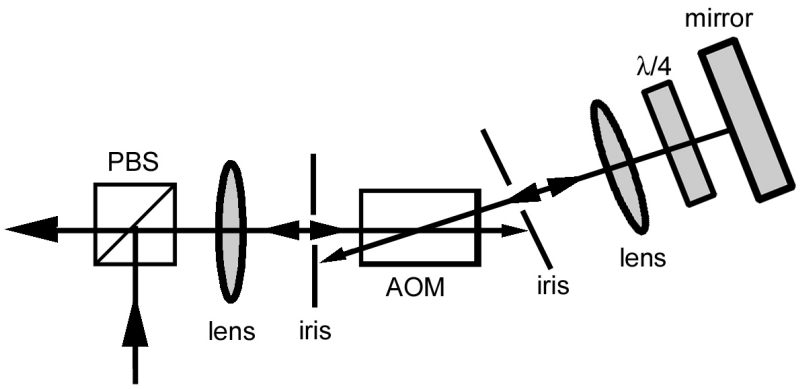

Figure 3.13: Schematic of a double pass AOM setup. The incoming beam (bottom) reflects through a polarizing beam splitter and is sent through a lens focused onto the AOM and an iris pinhole. The unshifted (and undeflected) beam passing through the AOM is blocked by a second iris, while the first-order shifted beam is deflected through the pinhole and another lens also focused on the AOM. The beam then passes through a quarter-wave plate ($\lambda/4$) before being retroreflected by a mirror. The retroreflected beam follows the reversed path but now has the opposite polarization when arriving at the PBS, passing through undeflected.

state preparation (pumping), external control (cooling), etc. Typically, the experimenter also wishes for some ability to change the laser frequency e.g. to scan over Doppler broadened absorption lines, to access various hyperfine or rotational levels, etc.

Tunable lasers such as the diode laser described above provide some ability to scan the frequency of the laser. This ability, however, coupled with noise sources such as thermal drifts and mechanical vibrations, tend to reduce overall stability when a fixed frequency is desired. Laser stabilization is reintroduced by locking the laser to a stable frequency reference. The stability of that reference is then transferred to the laser through the use of active feedback. Often, though, the stable reference is not tunable (e.g. a fixed atomic or molecular transition) or is not at the same frequency of interest. Further, locking the laser often limits the ability of the experimentalist to offset the laser from the locking frequency.

This work entailed the development of a system for locking a tunable diode laser of arbitrary wavelength. The resulting lock achieves this while maintaining a continuous tuning ability equivalent to the full modehop free range of the diode (∼50 GHz for our laser). In our method a Fabry-Perot (FP) cavity is actively stabilized to a He-Ne laser and provides stable frequency markers (longitudinal cavity modes) that are narrowly spaced. The FP cavity mirrors are ultra-broadband, allowing its use at both the He-Ne wavelength (633 nm) and an arbitrary diode wavelength from 300–1000 nm. An optical setup utilizing two acousto-optic modulators locks the diode laser to a single longitudinal cavity mode while providing offset tunability greater than the cavity mode spacing. A reliable method for changing the reference longitudinal mode while remaining locked extends the tuning range effectively until the diode laser undergoes a modehop. With this setup, stable diode scans of 50 GHz (in 3 min) are achieved for a 785 nm external cavity tunable diode laser.

Several features of this technique fit key requirements for our required optical setup. First, no molecular reference cell containing our molecule exists, due to lack of vapor pressure at reasonable temperatures, driving the need for a transfer cavity. Second, characterization of the beam source entails the need for locked scanning over 4 K Doppler widths (∼50 MHz) and linear Doppler shifts corresponding to velocities of 200 m/s (∼200 MHz) [64]. Third, to gauge the rotational temperature of our molecules, we require the ability to monitor many different molecular rotational transitions separated by ∼50 GHz [23]. Finally, the laser must be stable to less than our natural linewidth (∼1 MHz) over both long (30 min) data taking runs and short (10 ms) individual data events.

3.6.1 Locking apparatus

FP transfer cavities are widely used in atomic physics to stabilize or monitor a laser's frequency [65, 66, 67, 68, 69, 70, 71]. Two frequent problems remain with their use and are solved by our system setup. First, the fixed optical bandwidth of the cavity mirrors, limiting its use to either fixed wavelengths or narrow bands, has been removed by constructing the cavity using ultra-broadband mirrors. Second, the finite ability to offset the laser frequency from the locking frequency, necessitating a scanning lock or simple frequency monitoring, is eliminated, allowing for arbitrarily long scans.

Our system for the transfer cavity lock is outlined in figure 3.14. There are three main optical components: the FP transfer cavity, the stabilized He-Ne laser, and the stabilized diode optical setup; plus two main control components: the locking feedback, and the control of the diode scan "ratchet".

3.6.2 Fabry-Perot transfer cavity

A Fabry-Perot cavity is a spectroscopic device that achieves extreme resolution by utilizing multiple beam interference to either transmit or reflect a light from its input. The resonance transmission of the cavity occurs at regular optical frequency intervals, termed the free spectral range (FSR). Due to noise sources such as changes in the length of the cavity, the absolute frequency of these resonances change. These sources can be actively canceled, however, by locking the cavity to the transmission maximum of a stable optical source by changing its length with a piezoelectric actuator. When the stabilized cavity is used to monitor, or lock, the frequency of another optical frequency, the cavity is then termed a transfer cavity.

Our transfer cavity is constructed as a near-half-confocal cavity similar in design to that described in reference [72]. This design places a spherical mirror of radius R a distance $L \simeq R/2$ away from a flat mirror to form the cavity. Our cavity has mirror

raduis $R = 5$ cm. To reduce instabilities due to temperature fluctuations, all parts of our FP cavity are constructed from Invar. To facilitate non-confocal use, the curved mirror is cemented to a movable mount with a fine (40 threads/inch) screw secured via a locking nut. During locking operation we reduce the FSR by adjusting L to operate *away* from the half-confocal condition, i.e. such that $L \neq R/2$ [72].

This procedure of adjusting the cavity length allows resonances with regular frequency spacing of FSR $= c/4NL$ where N is an integer ($N = 2$ at the half confocal condition). While operating at large N has the advantage of producing smaller FSRs, the mode degeneracy is simultaneously N-fold reduced; causing a $N/2$-fold reduction in the intensity of each resonant transmission line, as well as enhanced sensitivity to cavity misalignment. In our cavity we observe resonant conditions with N up to $N = 25$, but for locking we operate the cavity at $N = 16$, $L = 5.25$ cm. In this configuration, the FSR is 88 MHz.

The requirement of reasonable resolving power in the cavity necessitates the use of high reflectivity mirrors. Typical cavity mirrors use dielectric coatings to provide high reflectivity over a narrow range of wavelengths. The advent of ultra-broadband mirrors allows us to extend the useful range of our FP cavity tremendously. Using these mirrors obviates the need for mirror sets that must be swapped for different wavelengths. They also permit us to use the cavity at multiple (largely separated) wavelengths simultaneously. One clear benefit is the relaxation of the requirement that the stable source be at a wavelength near the desired locking wavelength. Thus a single setup can serve the multiple requirements of our lab.

In our transfer cavity, each mirror is coated with the ultra-broadband Semrock Max-Mirror (MM1-311-A) coating in order to extend the useable range as far as possible. The flat mirror is a standard Semrock part and the curved mirror is custom coated onto a concave substrate (CVI SMCC-1025-.1-C). The Max-Mirror coating is

quoted to be >98% reflective from 350-1100 nm, which translates to reasonable cavity finesse (observed $F = 160$ at half-confocal) over the entire useable range.

Although the mirrors perform front-face reflection at a level consistent with manufacturers specifications, two main drawbacks with their use remain. One is that a mismatch in reflectivity between the mirrors exists, as measured by front-face reflection. This limits the total transmission of the cavity to less than 100% when on resonance. Although trying different mirror combinations can minimize this difference at a given wavelength, use at multiple wavelengths invariably requires relaxation of the perfect matching condition. In addition, another more serious problem persists that limits transmission even for well matched mirrors. While the reflection matches the manufacturers specifications, transmission does not make up the difference. For a good dielectric coating, one expects R (the reflection power coefficient) and T (the transmission power coefficient) to sum to one ($R+T = 1$). With the ultra-broadband coating mirrors, we measure (single mirror) T to be less than 10^{-4}, while R remains within spec ($\sim$.98). To explain the poor transmission, we propose that diffuse scattering off of the multiple layers needed to manufacture such a broadband mirror is the main loss mechanism. Since this mechanism limits the cavity transmission much more than the reflectivity mismatch, the total cavity transmission is approximated as an insertion loss in the input mirror and an extraction loss in the back mirror. At the half-confocal setup we measure the total transmission through the cavity as $T = 2.2 \times 10^{-5}$, and for $N = 15$ we find $T = 3 \times 10^{-6}$. Since the incident light onto the cavity is small (350 μW) and the total transmission is also low, we employ an avalanche photodiode mounted directly to the rear of the cavity and several electronic gain stages to detect the resonant transmission. Their use gives a signal to noise ratio of $\sim$10 at the back of the cavity.

3.6.3 He-Ne laser

With the ability to lock the cavity at a wavelength of our choice, we can implement the simple and inexpensive solution of using a stabilized He-Ne laser as our reference frequency [73]. The Newport model 117A self stabilized He-Ne laser is a turnkey system providing a specified stability of ±3 MHz/day. This self stabilization occurs at an internal 5 kHz rate, via frequency modulation of the He-Ne light. Pleasantly, we can utilize this internal frequency modulation to also provide the dither we require for locking the cavity to the He-Ne. A simple pick-off from the internal circuitry powering the He-Ne provides the reference to this 5 kHz modulation. The demodulated cavity transmission serves as the error signal for feedback to the cavity piezo.

3.6.4 Diode laser optical setup

In order to lock the diode (Sacher Lasertechnik TEC-500), we begin by injection-seeding a 100 mW anti-reflection coated amplifier laser. Roughly 20 mW of this light must be sent to the locking subsystem, due to the large number of optical elements, and the low cavity transmission. The remainder of the light is sent to the experiment as well as other diagnostics: a wavemeter for coarse wavelength readings, and another FP in scanning mode to verify proper injection and single mode operation.

In the locking subsection, diode light is sent to two AOMs in a double pass configuration and then combined with the He-Ne light via a polarizing beam splitter before finally being directed to the FP transfer cavity. More than one laser may be locked by combining their light via polarization or wavelength sensitive optics before the optical cavity. Transmission is monitored with a single detector if the lasers are modulated at separate frequencies with separate demodulation for locking, or with multiple detectors by splitting the transmitted light. We operate with a single detector, using He-Ne modulation at 5 kHz and diode modulation at 80 kHz.

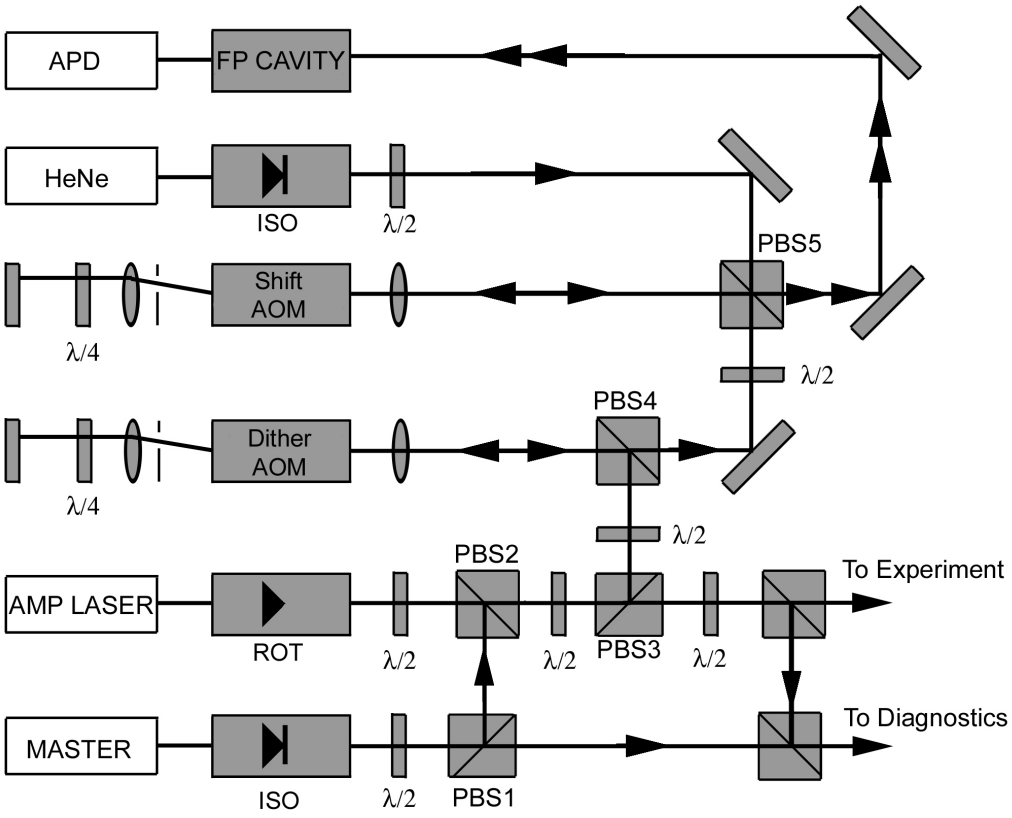

Figure 3.14: Overview of the laser lock optical setup. A grating stabilized tunable diode laser serves as the master laser to injection lock a 100 mW anti-reflection coated laser diode. 20 mW of this is required for effective locking; the rest is sent to diagnostics equipment (for monitoring the injection) and the experiment. Locking light is sent through two AOMs, each in a double pass configuration. The first AOM serves to dither the laser light, while the second shifts the overall frequency to provide tunability under lock. This light is then combined with a stabilized He-Ne reference beam and sent to the Fabry-Perot cavity, which is monitored with an avalanche photodiode (APD). One servo feedback loop locks the FP cavity to the He-Ne laser transmission maximum, and another locks the master laser to a cavity transmission maximum.

The AOMs in the diode setup provide for two functions: dithering for the locking scheme [74, 65], and stable shifting of the laser frequency offset under lock. Attempts utilizing a single AOM to perform both dither and shift found very large residual amplitude modulation (AM) at the dither frequency which confounded the lock. The cause of this AM we attribute to two effects, both of which are a direct result of combining the functions onto a single AOM. First, any AOM has an overall diffraction efficiency that is maximum at its design frequency. Operating the AOM at its design frequency and a applying small frequency dither for the locking produces residual AM that is second order in the AOM efficiency. In contrast, using this same AOM away from its design frequency implies a first order residual AM that grows substantially as one nears the edge of the AOM bandwidth. Second, the angle of the input beam to the AOM crystal must match the frequency-dependent Bragg condition for efficient diffraction. Residual AM occurs here as alignments change as the diffraction angle varies with frequency. As in the first case, aligning the crystal for maximum efficiency at its design frequency thus means that a small dither induces first-order residual AM unless the AOM is operated with the dither center at the design frequency. Taken together, these effects produced a residual AM (figure 3.15) that precluded using the AOM over its full bandwidth while remaining locked.

Employing two AOMs solves both of these problems. The dither AOM is aligned for maximum efficiency at its design frequency, on which the dither is centered. Any residual AM is then second order. The shift AOM is also aligned at its design frequency, albeit with a tight focus at the AOM crystal. This tight focus trades overall efficiency (10% single pass) for less sensitivity to large detunings (due to Bragg angle misalignments). Here, the frequency dependence of the laser amplitude has little effect on the lock, since this frequency provides the quasi-static offset. For our locking operating condition, we apply an 8 MHz-deep dither (at a rate of 80 kHz) in the first

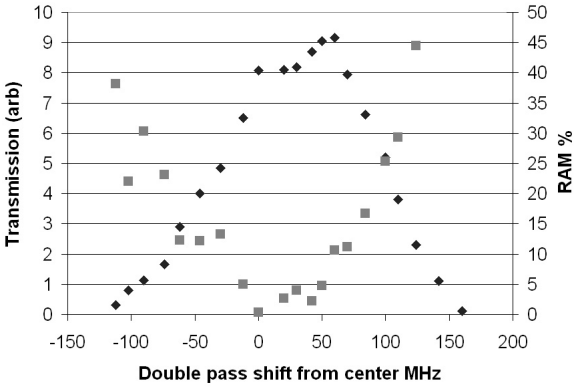

Figure 3.15: Combined efficiency of the locking optical setup to the input of the Fabry-Perot cavity over the tuning range of the shift AOM (diamonds). The squares show the residual amplitude modulation as a percent of transmission that occurs if the shift AOM also serves as the dither.

AOM that produces $< 10^{-5}$ residual AM. The overall offset tuning range is then determined by efficiency changes of the shift AOM. The efficiency relative to zero shift is shown in figure 3.15. Any relative change in this efficiency alters the total closed loop locking gain at DC; we find that the lock is stable up to double-pass shifts of about $\pm$75 MHz.

3.6.5 Lock performance

Feedback for locking occurs via the Pound-Drever-Hall locking scheme where the APD signal is demodulated both at 5 kHz (He-Ne modulation) and at 80 kHz (diode modulation) and then sent to PID controllers feeding the cavity piezo, and diode external cavity piezo, respectively. Clear separation of the error signals is possible as each demodulated signal has a bandwidth limited to 2 kHz.

We find that during operation, the lock performs well and is stable against room noise, optical table vibrations/bumps and thermal drifts. A power spectrum analysis of the error signals reveals the noise power spectrum is mostly white over the 3 dB closed loop bandwidth of each lock (1 kHz each). The largest contribution to the

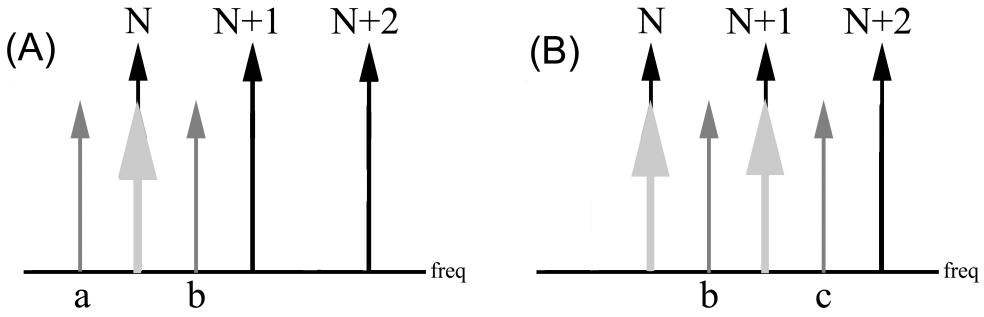

Figure 3.16: The ratchet lock process. FP cavity modes, spaced by FSR on the horizontal frequency axis, are represented by black arrows. (A) When the light entering the cavity is locked to mode N, slowly changing the AOM frequency allows for laser tuning (gray arrows) between points a and b. (B) When the laser is at point b and the AOM frequency is quickly increased one cavity FSR, light entering the cavity is "ratcheted" from mode N to mode N+1. Slowly changing the AOM now allows tuning between points b and c. The process repeats to allow locking to mode N+2 and so on, until the laser undergoes a modehop.

noise spectrum while locked is a spike at the 60 Hz line frequency corresponding to a 700 kHz peak deviation of the laser frequency.

3.6.6 Ratchet lock

To extend the tuning range under lock we implement what we call a "ratchet lock". Essentially, this process is a way to incrementally change which cavity longitudinal mode is used for locking the diode. Typical uses of FP transfer cavities use a single cavity mode. There, locking to a different cavity mode requires turning off the lock, tuning the laser, then turning the lock back on. During this process, it is difficult to determine how many modes one has skipped during the tuning process, particularly if the laser frequency is unstable over the time it takes to tune. Our ratchet scheme keeps the lock intact during the entire process, even while the mode used for locking is changed.

Normal tuning of the laser frequency (f_{laser}) occurs as the single pass frequency

deviation of the AOM from its center (f_{AOM}) is slowly shifted over one-half cavity FSR ($\pm.25$ FSR from center). Double passed through the AOM, the light entering the cavity is constrained to match the cavity resonance via feedback to the laser's piezo tuning voltage, so the lock changes the laser frequency by one FSR. This process is described mathematically as follows:

$$f_{\mathrm{laser}} + 2f_{\mathrm{AOM}} = f^{N}_{\mathrm{cavity}} \tag{3.13}$$

$$\Delta f_{\mathrm{laser}} = -2\Delta f_{\mathrm{AOM}} \tag{3.14}$$

A ratchet is performed when the normal tuning reaches its limit. For example, when the negative tuning limit ($f_{AOM} = -.25\mathrm{FSR}$) is reached, the AOM is quickly (over $\sim$10 ns) changed to its positive tuning limit ($f_{\mathrm{AOM}} + .25\mathrm{FSR}$). For this ratchet operation the time over which f_{AOM} changes is by design much quicker than the laser lock can respond ($\delta f_{\mathrm{lock}} \sim 1$ kHz). Hence, the laser frequency essentially remains constant during the operation. Since the lock has had no opportunity to respond, light entering the cavity increases by one FSR. Because this shift is exactly one FSR by design, this light is also resonant with the cavity. The lock then, when given enough time, will respond and stabilize the laser to a new cavity longitudinal mode. This process is diagramed in figure 3.16 and by the equations below.

Before ratchet:

$$f_{\mathrm{AOM}} = -.25\,\mathrm{FSR} \tag{3.15}$$

$$f_{\mathrm{laser}} - .5\,\mathrm{FSR} = f^{N}_{\mathrm{cavity}} \tag{3.16}$$

After ratchet:

$$f_{\mathrm{AOM}} = +.25\,\mathrm{FSR} \tag{3.17}$$

$$f_{\mathrm{laser}} + .5\,\mathrm{FSR} = f^{N}_{\mathrm{cavity}} + \mathrm{FSR} \tag{3.18}$$

$$= f^{N+1}_{\mathrm{cavity}} \tag{3.19}$$

We find that the ratchet process is quite robust. The only issue is the initial alignment; we must ensure that the diode alignment into the cavity couples to all resonant modes equally. Optimizing a single resonant mode leaves others depleted, varying lock gain to those modes substantially, affecting the quality of the lock as the mode is changed. However, establishing correct alignment is fairly simple by scanning the cavity over several FSR during the alignment.

Long scans are achieved by performing a series of ratchets corresponding to the total desired scan length. To control the laser frequency, a computer DAQ analog voltage output controls the AOM frequency, providing small changes in the AOM frequency for normal tuning and large changes for ratchet operations. During long scans the computer also monitors the coarse wavelength of the diode, read from a wavemeter, to warn the experimenter if a modehop occurs.

3.7 Absorption detection

The detection of molecules inside the buffer gas cell is performed with time-resolved absorption spectroscopy. Improving the detection sensitivity of this setup in order to measure the small molecular absorptions was a tedious task. There were many noise sources present, including stray light, electronic crosstalk, and laser power noise. Many different levels of sophistication were built up over the course of the cell and beam characterizations; here we follow the progression taken in the lab in order to reach adequate sensitivity levels to detect molecules.

The first concern with improving the detection efficiency are processes and effects that are concurrent with the timing of the ablation process. These processes are especially troubling because they have the potential to mimic a time-resolved absorption signal, and may be even frequency dependent. One particular example (which occurred when first beginning the spectroscopy experiments) is when the YAG electrical

noise caused the diode laser to run multimode concurrently with its firing, but only for certain wavelengths. The signal on the detectors was deceivingly similar to the sought-for absorption, and perhaps there was some sort of spectrum. Of course when this signal remaind after the YAG light was physically blocked, molecular absorption was ruled out.

Thus we see how YAG electrical noise was and still can be a major issue. The above example was only alleviated by internally realigning the diode laser to provide more stable lasing. Still, at a bare minimum it was also found that the power supply of the pulsed YAG laser should be isolated from that of the detection laser by being on different electrical circuits. In addition, since the lasers occupy the same optical table, the YAG laser head also needs to be electrically isolated. Finally, since the YAG cooling unit is directly beneath the optical table, the vibrations and noise that it generates couple directly into the table, when it is floating. Thus we currently operate with the table directly resting on its supports.

Another source of time-resolved concurrent noise is light scatter associated with the ablation process. Light from the YAG itself is so intense, that it seems to fill the cell by bouncing off of the various windows and surfaces. Although temporally short, this intensity can saturate any detector; problems arise particularly when the recovery of the detector has a time scale similar to an absorption trace. This can be dealt with by careful spatial baffling of the absorption beam. Use of colored glass and of interference filters can also spectrally filter out this noise source. Light from the ablation plume is more of an issue (see figure 3.17). Here the decay of highly excited molecules, from the center of the cell, presents a spatial and spectral light source that matches the signal. The best ways to deal with the plume are to limit the its solid angle into the detector via baffling, and to use a probe laser modulation scheme with lock in detection.

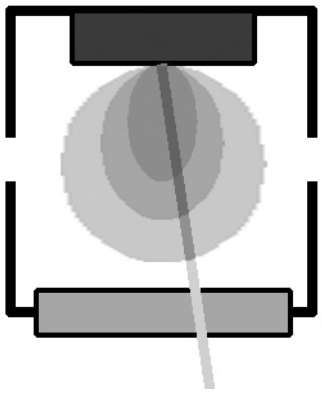

Figure 3.17: Schematic of ablation plume. When the ablation laser fires, highly excited molecules and helium form a bluish-purple plume as they decay to lower energies. The overall size of the structure is dependent on the buffer gas density inside the cell; the shape resembles the assumed cosine distribution. This light takes several milliseconds to decay and has many spectral components, making it difficult to filter out from absorption or fluorescence signals. Notably, for large signal sizes, the plume is also strong, making it a good (but not necessarily safe) way to monitor ablation efficiency.

Intrinsic laser noise, while not time-resolved like the absorption signal, still limits overall sensitivity. And while the maximum theoretical sensitivity is limited only by the shot noise on the laser power, typically 1/f noise and other technical noise sources constrain absorption sensitivity to several orders of magnitude below the shot noise limit. By splitting the absorption beam equally, sending only one through the absorbing molecules, and detecting both much of this noise can be canceled. This is because the two measurements enable complete subtraction of the common mode laser noise in the beam pair. Setup of such a scheme is a delicate process, to avoid any differential (non-common mode) noise sources, again especially for time-resolved differential signals.

In the end, the most sensitive absorption setup accomplished in the molecular beam experiments employs both an "auto-balanced" detector and a wavelength modulation scheme to reach absorption sensitivities of $\sim 10^{-4}$ over a millisecond integra-

tion time. An auto-balanced detector is one with two inputs, one for the signal beam, and the other for the reference. The two signals are sampled internally and their (DC) powers are compared. If the relative power differs, then an internal gain compensates to equalize them. The recorded signal then equals the gain-compensated subtraction of the two beam signals. This gain compensation has a bandwidth limit so that any differential signal above this is not compensated for. Thus wavelength modulation of laser faster than the gain compensation bandwidth (giving absorption modulation in the signal) will not be subtracted. All common-mode noise will still be subtracted. The main limitations preventing further sensitivity gains are absorption, etalon, and polarization effects in the optics (coated with SrO dust, poor AR coatings, etc.). Despite these limitations, the absorption inside the cell performed well. However, in the beam fewer molecules are present and we needed a more sensitive detection technique.

3.8 Fluorescence detection

Fluorescence detection is an extremely sensitive technique for the detection of minute amounts of atoms and molecules, even down to a single atom or molecule [75]. Its ultimate limit is mainly the dark counting rate of the detector along with any scatter; this technique is relatively insensitive to detection laser noise. Thus of course, the same stray light that affects the absorption detection also plagues us here. But again, careful spatial and spectral filtering reduces their effects. Maximizing the signal to noise for molecular detection then requires a careful choice of pump and probe wavelengths to maximize detection efficiency and scatter rejection. Below we discuss the experimental measures that were taken to detect the molecular fluorescence signal.

3.8.1 Collection lenses and signal filtering

To collect fluorescence light from the molecular beam a set of lenses was set up. Although conceptually simple, this required several iterations to generate a reasonable solid angle of collection while rejecting stray light. The first attempt at monitoring the beam had a single lens placed one focal length away from the collection point (see figure 3.18 (A)). The lens axis was set at a 45 degree angles to both the pump laser beam and the molecular beam to allow both to pass by undisturbed. Here the lens acts to collimate the light from the source; this collimated beam travels out of the vacuum chamber, where it was refocused onto the photo multiplier tube (PMT) detector. To collect as large a solid angle as possible, the lens with the smallest focal length consistent with the constraint on the lens diameter, that it block neither beam, was chosen. This arrangement suffered from two main flaws: difficulty of alignment, and admittance of large amounts of stray light. The process of cooling down inevitably shifts the positions of the cryostat and components as a result of thermal contractions. Using a small focal length lens invariably introduces a long lever arm between the object (here the fluorescing molecules) and the image at large distance (here nominally at infinity). This leads to strong coupling of contractions to alignments. After cooldown of the cryostat, however, there was really no way to discern if the alignment remained satisfactory; and there was no way of realigning the lens. Finally, this arrangement suffers badly from all of the stray light bouncing throughout the chamber that it collects (swamping any signal).

The second system set up to collect fluorescence light is shown in figure 3.18 (B). To cut down on the admittance of stray light, a spatial filter was employed, and to reduce alignment sensitivity, a light pipe was placed in the path. The spatial filter works by putting the lenses in a 2f-2f-1f arrangement. That is, a one-to-one image is created at the pinhole because the first lens is placed at twice its focal length away

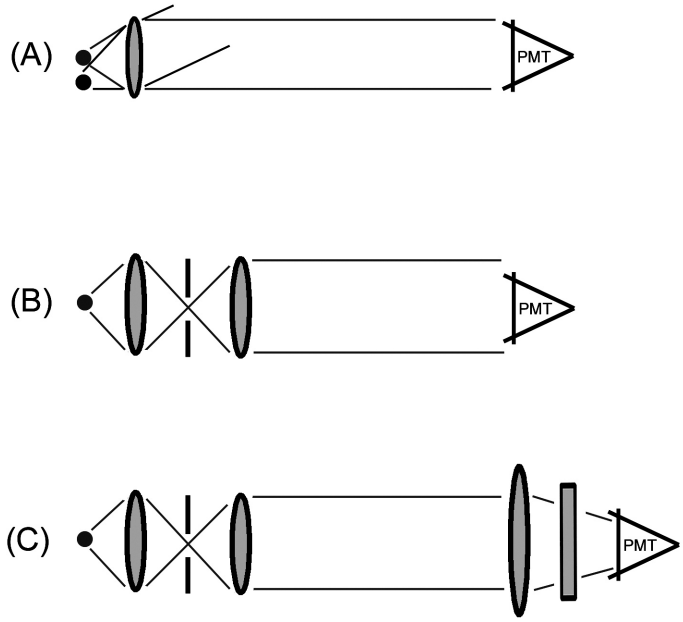

Figure 3.18: Schematic of lens arrangements for the collection of fluorescence light. (A) shows the single lens configuration, and how small displacements move the image substantially. (B) shows the 2f-2f-1f (all lenses are of focal length f) configuration (not to scale) where the first lens images the source onto a pinhole (for spacial filtering) and the second lens collimates light out to the detector. (C) shows the standard detector setup. The first element consists of a achromat lens pair because such lenses are designed to operate at infinite conjugate ratios. The spatial filtering pinhole is crucial to block scattered YAG and plume light. The (2 inch) lens in front of the detector is larger than the (1 inch) collimated fluorescence beam and is weakly focused (to avoid angular effects in the interference detectors) onto the detector. Alignment is checked prior to closing the vacuum chamber by placing a light source at the desired detection point.

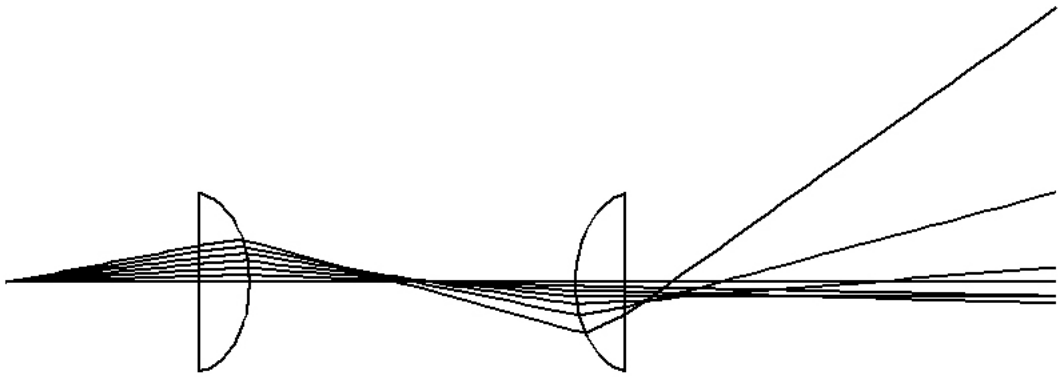

Figure 3.19: Ray tracing of fluorescence light in the two lens detection setup (with plano-spherical lenses). Notice how the output light is decidedly not collimated. This is due to spherical abberations in the lenses. The two most aberrant rays would entirely miss the 2 inch detector lens and thus sets an upper limit to the clear aperture of the first lens to less than 1/3 inch (diameter).

from the object. The pinhole serves to block any light that did not emanate from the source. The second lens is then placed one focal length away, to collimate this light into a light pipe. The light pipe ends right before the chamber window, where the detector is placed directly opposite. This setup dramatically reduced the amount of stray light that reached the detector, but it was found that the collection efficiency of this setup was not what was expected (see figure 3.19).

As any optician may have forewarned, the correct choices and use of lenses are especially important in a large-angle light gathering system. Naive assumptions that the clear aperture of a lens is its entire area and it forms an image free of abberation at a point given by standard optics formulas is just that, naive. The collection efficiency of the setup described above with these assumptions would thus be the solid angle that the first lens subtends, as seen from the molecules. This estimate of collection efficiency breaks down when spherical abberations become important because as more elements are added (and when lengths are long), the light does

not follow the paths that simple ray tracing (without regard to the true lens shape) predicts. Thus, especially at large angles, light is lost from the system. In fact, for the three lens setup of figure 3.18 (C) with standard (or even aspheric) lenses, the collection efficiency was *ten times* lower than expected.

Fortunately, substitution of achromatic lenses for the standard ones effectively solved this problem. These lenses are designed to minimize both chromatic and spherical abberations over a range of wavelengths for infinite conjugate ratios (either when the object or image are at infinity). The setup shown in figure 3.18 (C) using these lenses performs to specification. Now the (correctly oriented) front lens is placed 1 focal length away to collimate the light directly into another achromat that images it at the pinhole. The final achromat then collimates this light into the lens tube as before. Once proper collection efficiency (4% solid angle) was obtained with the proper lenses it was determined that alignment was not really an issue and the light pipe was removed (to reduce the heat load onto 4K) without any trouble.

In addition to the pinhole spatial filter, direct masking of some of the collection area was required. This is again due to the fact that the collection optics were directed right on the molecule beam exit aperture. Any stray light from the probe beam (e.g. reflections from optical surfaces) that bounced into the buffer gas cell would easily cause molecules in the cell to fluoresce. This fluorescence light can come out of the cell via the aperture and be directly captured by the detector. When the image of the aperture was covered, it was found that even light deliberately directed into the cell did not result in a fluorescence signal.

Spectral filtering of the collected light was performed to separate the signal light from any backgrounds. This was done with a combination of interference filters and colored glass. Interference filters have a narrow spectral acceptance, perfect for separating our desired wavelength (830 nm) from backgrounds (1064 nm, 532 nm,

and 785 nm). However, the large angular dependence of the filter and the finite rejection ratio means that some of this light is transmitted. The colored glass has a much broader spectral response, yet does not show the same angular behavior as the interference filter. Thus in combination the two filters worked effectively to block scattered light.

Even with all of the spatial and spectral filtering isolating the signal from backgrounds, temporal filtering was also required. Here the PMT detector was gated off during the time that the YAG beam pulses, cutting down on the recovery time needed from this large pulse. Also, chopping the probe beam intensity and synchronously detecting the fluorescence effectively distinguished between the desired signal and backgrounds due to the unmodulated plume light. The fast, time-resolved, characteristics of the signal required a >10 kHz chopping frequency. This was done with an AOM intensity modulated pump beam and a SRS lock in demodulator.

3.9 Summary

The construction of the molecular beam apparatus was a process that pulled together many of the common techniques of atomic and low temperature physics. When viewed in terms of the history of work on atomic and molecular beams it is remarkable that such a conceptually simple machine can produce this wonderfully general *and* powerful source. Although this thesis goes a long way toward proving this method as a resource to the community, the real proof may be the fact the several beams are being build up in emulation of ours by groups around the world.

3.9.1 Improvements

Several improvements to the setup are underway. First and foremost is the removal of the diffusion pump. This removal was slowed somewhat by pride, since the charcoal

cryopump was more than sufficient at pumping away our gas load; it can be placed directly where we wish the pumping to be, without the conduction losses through baffles. Removal of the pump simplifies the experiment operationally, by removing the requisite electronics, cooling water, and space required to support it. Taking the pump out also allows optical access from the bottom. This access may prove to be invaluable, since it would permit simultaneous in-cell absorption and beam monitoring at multiple positions. Hopefully, this will alleviate the current limitation of either absorption or single point (directly at the aperture) fluorescence detection. Also, detecting in a direction perpendicular to the probe (and ablation) laser beams should cut down the stray light that is conveyed to the detector, due to the larger scattering angle required.

Other improvements to the setup involve upgrading the laser and detection optics. New lasers with more stable electronics can cut down on the experimental overhead of running the system by allowing for trouble free (not yet achieved) lasing and frequency locking. Also, imaging with an intensified CCD camera might allow for better characterization of the fluorescence region, simplifying detector alignments and molecular beam shape measurements.

Chapter 4

Studies with strontium oxide

4.1 Room temperature yield

The SrO experiment began with an ablation yield study at room temperature because although the ablation yield of most targets is predictable, there have been a few exceptions. The basic setup for this study is shown in figure 4.1, it consisted of a Quick-Flange vacuum apparatus, a turbo pump, and the detection and ablation lasers. The density of the helium inside the cell was directly monitored with a Pirani vacuum gauge, and controlled with valves to a high-pressure inlet and to the pump. Both lasers were controlled and data acquisition occurred via computer in a custom-written Labview program.

Detection in the room temperature buffer gas setup was accomplished with a balanced absorption measurement. The New Focus Nirvana detector auto-balances the relative gain of its two optical inputs so that their difference is zero, at DC. Internal monitoring and gain adjustment maintains this zero difference, up to a selectable bandwidth. The optical input subtraction, however, occurs at a much faster bandwidth than the gain auto-balance, so that any common-mode noise on both inputs (e.g. from laser power fluctuations) is efficiently subtracted away. Any differential signal (caused by absorption in the molecule cloud or differential noise sources) will

appear on the output as long as it is faster than the auto-balance correction. Thus a careful setup minimizing time-varying differential signals, and proper setup of the absorption signal were key. The differential absorption was accomplished by passing both the signal and reference beams through the cell, one in front of the SrO (where it would absorb from the molecular cloud) and one behind (where it would not). The fast, time-resolved, nature of the absorption meant that the absorption signal was naturally above the auto-balance bandwidth.

Although the Nirvana detector worked well in subtracting common-mode noise, minimizing the differential noise was difficult. Turbopump vibrations moving the laser beams and cell windows caused etalon effects; this is why it was necessary to pass both beams through the cell. In addition, differential signals from stray ablation light and plume fluorescence were also key noise sources when looking for the absorption signal. Interference filters on the inputs to the detector did block most of the YAG ablation light. The plume light was more difficult to isolate spectrally, since it inevitably included spectral components from many different transitions as the excited plume decays. To further combat both sources of stray light, blackened irises, coupled by blackened tubes, were placed at the exit to the cell, halfway to the detector, and at the entrance to the detector. Also, lengthening the path from the buffer gas cell to the detector reduced the solid angle of the cell that the detector saw.

4.1.1 Determining the yield

Optical column density

Monitoring the time-resolved absorption of the detection laser after every ablation pulse can give many insights on the buffer gas cooling process. Since this is a pulsed, dynamical process, signal characteristics including signal size can strongly depend on things like buffer gas density and laser positioning. Since the ultimate goal is a

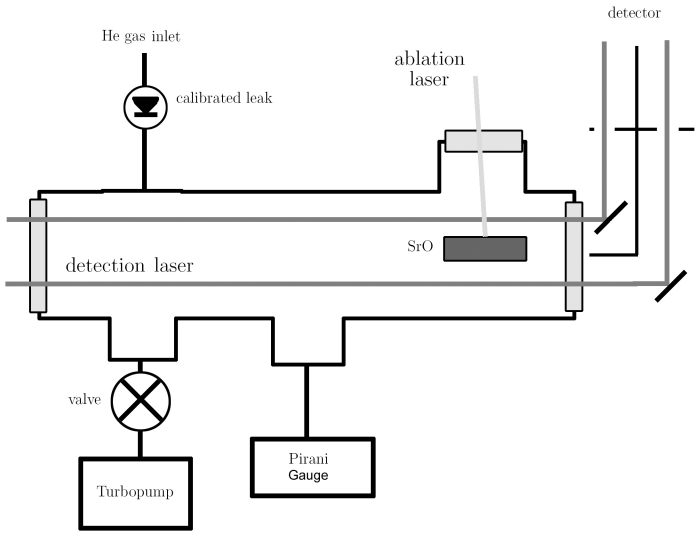

Figure 4.1: Experimental setup of the room temperature buffer gas setup, consisting only of simple vacuum components, the laser ablation, and detection laser. Careful balanced detection and spatial isolation of the detector from the ablation spot and plume are necessary for sufficient detection signal to noise ratios.

determination of the ablation yield, the ingredients leading to its deduction will now be explored.

During the ablation process, the molecules are ejected at high temperatures, with an undetermined distribution from the surface. The thermalization process is linked to the buffer gas density inside the cell. Intuition leads to a picture whereby a ball of hot molecules emerges from the surface, expanding as it collides with helium and cools. When the molecules have thermalized with the helium, the expansion will have produced a roughly symmetric cloud of molecules, centered around an average thermalization distance l_t from the surface of the ablation target. This thermalization distance should scale inversely with the helium density, since the only length scale, the mean free path between the molecule and helium, also scales in this way. Monte Carlo simulation of this process (described in section 2.4.4) suggests that the diameter of the cloud is roughly the same size as l_t, when all the molecules have fully thermalized

(c.f. figure 4.2). This size arises due to the variation in the number of collisions it takes to thermalize and the free path variations between collisions. For simplicity then, when determining the yield, the thermalized cloud is assumed to be spherical, and of constant density. Probing with an absorption laser positioned closer than l_t will catch the cloud before it has had a chance to thermalize, broadening observed Doppler widths and raising measured rotational temperatures for early observation times. Probing at l_t and beyond will show fully thermalized temperatures. However, any measurements of the cloud at positions past l_t will show reduced absorption as the cloud expands toward the probe beam position. Variation of the in-cell density allows for a fixed probe position while experimentally changing l_t to find the maximum absorption.

To summarize, a thermalized cloud of buffer gas-cooled atoms will show thermalized Doppler and rotational temperatures as well as maximum absorption when *both* the distance of the probe is placed one thermalization length l_t away from the ablation point *and* when the cloud passes this point in time. The cloud is modeled as a sphere with diameter l_t with constant density $n = \frac{N_{J'}}{(4/3)\pi(l_t/2)^3}$ where $N_{J'}$ is the ablation yield into state $|J', v' = 0\rangle$. The path length of the absorption laser inside the cloud is l_t.

To relate the absorption signal to these conditions we note that the transmitted power, P_t, of a laser of initial power P_0 through an absorbing medium is governed by Beer's law [64]:

$$P_t = P_0 \exp[-n\,\sigma_{\text{abs}}(\omega)\,\Delta x]\,, \tag{4.1}$$

where n is the density of the medium, $\sigma_{\text{abs}}(\omega)$ is the frequency-dependent absorption cross section, and Δx is the path length through the medium. When $n\,\sigma_{\text{abs}}(\omega)\,\Delta x$ (termed the optical column density) is small, the absorption will be small and the fractional absorbed power

$$\frac{\Delta P}{P_0} = \frac{P_0 - P_t}{P_0} \tag{4.2}$$

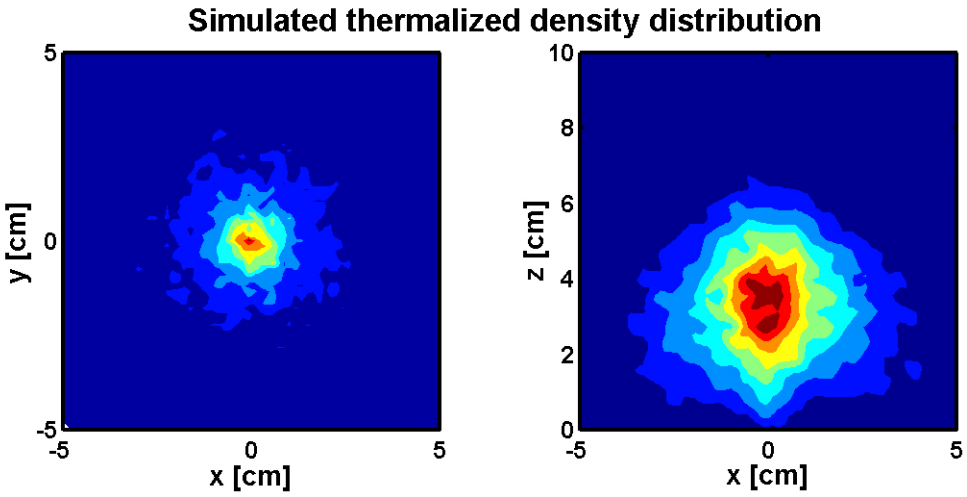

Figure 4.2: Simulation of the thermalization process. Molecules at 1000 K are allowed to propagate until they reach a velocity less than the 4.2 K thermal RMS velocity. Their distribution in 2D is shown for a plane perpendicular to the ablation beam (left) and parallel to the beam (right). The ablation point is at the origin. Parameters for the simulation are: 10000 molecules, 10^{16} cm^{-3} helium density and 10^{-14} cm^2 helium molecule collision cross section. The simulation suggests that molecules thermalize around a mean distance l_t, forming a cloud of diameter l_t due to variations in the number of collisions to thermalize and free path variations between collisions.

can be simplified to

$$\frac{\Delta P}{P_0} \simeq n\,\sigma_{\rm abs}(\omega)\,\Delta x\,. \tag{4.3}$$

Identifying with the molecular cloud parameters above gives

$$\frac{\Delta P}{P_0} = \frac{6N_{J'}}{\pi {l_t}^2}\,\sigma_{\rm abs}(\omega) \tag{4.4}$$

for the maximum absorption of the probe laser, for yield $N_{J'}$.

Absorption cross section and lineshape

When Doppler broadening is the assumed to be the largest source of broadening (valid at $T = 4.2$ K and higher), the lineshape of the fractional absorbed power will be the typical inhomogeneously broadened Gaussian line with width γ_D due to the molecules' motion that depends on the molecule's mass M and temperature T as follows:

$$\sigma_{\rm abs}(\omega) = \sigma_D(\omega) e^{-((\omega-\omega_0)/\gamma_D)^2}\,, \tag{4.5}$$

$$\gamma_D = \frac{\omega_0}{c}\sqrt{\frac{2k_bT}{M}}\,. \tag{4.6}$$

On resonance ($\omega = \omega_0 = \frac{2\pi c}{\lambda_0}$), the Doppler-broadened cross section $\sigma_D(\omega)$ for a molecular $|J', v'\rangle \Rightarrow |J'+1, v''\rangle$ transition is

$$\sigma_D(\omega_0) = \frac{{\lambda_0}^2}{4\sqrt{\pi}}\frac{2J'+3}{2J'+1}\frac{\gamma_p}{\gamma_D}\,. \tag{4.7}$$

Here the partial width γ_p is given by

$$\gamma_p = \frac{1}{\tau}{\rm FCF}[v'', v']\frac{J'+1}{2J'+3}\,, \tag{4.8}$$

where ${\rm FCF}[v'', v']$ is the Franck-Condon factor for the transition and τ is the total lifetime of the excited state. Combined use of equations 4.5–4.8 allows for calculation of the resonant cross sections for various $|J', v'\rangle \rightarrow |J'+1, v''\rangle$ transitions as a function of T.

State occupation

The number of absorbing molecules $N_{J'}$ in state $|J', v' = 0\rangle$ depends on the total molecular production N, the energy of the state $[B_e J(J+1)]$ and the temperature T through the Boltzmann probability distribution:

$$N_{J'} = \frac{N(2J'+1)\exp[\frac{-B_e J(J+1)}{k_b T}]}{Z}\,. \tag{4.9}$$

Here k_B is the Boltzmann constant and the partition function Z is the normalization for the distribution. At such low temperatures, only the lowest vibrational state has substantial population, so v' can be set to zero.

Combining equations 4.4–4.9 for a calculation of the absorption spectrum now involves placing the known [53] line centers of the transitions and calculating the molecular spectral response. Such a calculation is shown in figure 4.3, at $T = 300$ K for a production of $N = 2\times10^{12}$ molecules on several $|X^1\Sigma, J', v' = 0\rangle \rightarrow |A^1\Sigma, J'+1, v'' = 1\rangle$ transitions. The observed absorption data with 300 K buffer gas shows fully thermalized rotational temperatures and lies neatly along this prediction. It differs from the reported one significantly only near the dense band head, where a split line is found below the resolving power of the previous work. Otherwise the match between the calculated and observed is excellent. Hence we report that the ablation yield of molecular SrO is $N = 2 \pm 1 \times 10^{12}$.

4.2 Lifetime of the excited state

Since the value of the calculated yield depends on the excited state molecular lifetime τ, and no previous measurement of this value existed, experiments were carried out on the room temperature buffer gas setup to measure it. The setup was similar to the yield experiments; however, to measure τ, a chopped-beam fluorescence experiment

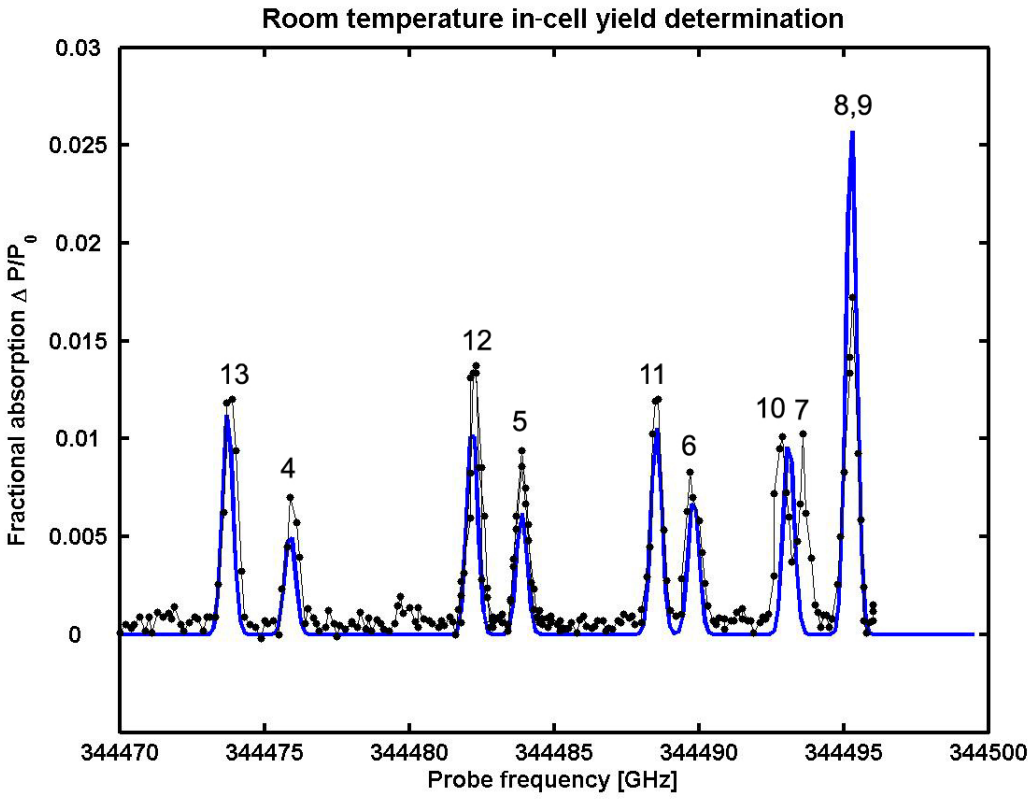

Figure 4.3: Room temperature fractional absorption of SrO molecules for $|X^1\Sigma, J', v' = 0\rangle \Rightarrow |A^1\Sigma, J' + 1, v'' = 1\rangle$ transitions near the band head. The calculated curve (blue) assumes the production of $N = 2 \times 10^{12}$ molecules and uses line centers from reference [53]. The observed spectrum shows a split line next to the band head, but otherwise good agreement. Lines are numbered according to their value of J'.

was used. When the pump beam is on, molecules are transferred into the excited state. Fluorescence from the decay of this state will be steady when the pump is on for a time greater than τ. When the pump is suddenly turned off, the excited state population will decay exponentially. Monitoring this exponential fluorescence decay allows for the extraction of τ.

For this measurement, a light pipe perpendicular to both the detection and ablation laser was added to the yield experiment setup. Fluorescence exiting from this light pipe was imaged with a lens onto the face of a fast, large-area avalanche photodiode. To combat excess light scattering from the ablation laser, the plume, and the pump laser beam (pump and fluorescence were at the same wavelength), the light pipe was enclosed in a darkened tube. Some scatter, ablation, and plume light remained, however, complicating the analysis of the data.

To take the measurement, first a single recorded absorption trace confirmed that the laser was on resonance, then 32 fluorescence data traces were averaged while the laser was on resonance. After this, another absorption trace was recorded to ensure that the laser did not drift and the SrO yield did not decay. A second, identical set of data, but now off resonance, was used as the reference and was subtracted from the first to eliminate the backgrounds. To ensure that the decay signal was due to the molecules, the detectors and electronics were carefully checked to make sure their response was faster than any expected or measured decay signal.

Since the buffer gas cooling process is a dynamical process, the pump beam intensity was chopped on and off at a rate of 100 kHz to determine if the lifetime measurement varied as the molecule cloud passed through the pump beam. The modulation was done with a single pass AOM configuration using the first order diffracted beam. The intensity modulation had a measured 10 ns response time; this chopping was tightly synchronized with the ablation pulse to prevent asynchronous

averaging. In addition to the investigation of time variation in the decay, the density of helium inside the cell was varied over an order of magnitude in order to rule out any systematic effects due to quenching collisions or diffusion through the helium. The measurements show no effect due to either (see figure 4.5): the decays were consistent across the time of the pulse and the complete range of pressure change (over a decade). The mean value of these measurements is $\tau = 270 \pm 20$ ns.

4.3 Buffer gas cooling at 4K

Cooling with a cold buffer gas rather than a warm one is not a fundamental change in any sense. To reach this colder temperature, extra collisions will be required, but the model of collisional cooling (c.f. section 2.4.2) dictates that the number will still be small ($\sim$60 at room temperature vs. $\sim$100 at 4.2 K). When the cryostat is cooled, then, reexamining the yield as before should show similar thermalization behavior and dynamics. The associated temperatures, Doppler and rotational, will be 4.2 K when the molecules are thermalized to the cold buffer. Both of these changes lead to the increased on-resonance absorption of cold molecules versus the room temperature version. The buffer gas setup for the cold absorption studies was detailed in figure 3.10.

4.4 Collision cross section

Finding the effective thermalization cross section (σ_{SrO-He}) between the helium atoms and SrO should be possible from observing the time-resolved characteristics of the molecular cloud, specifically the decay time constant T_a of the absorption signal. This is because at long times, the SrO density n_{SrO} and hence the absorption signal should be the solution to a diffusion equation with the cell boundaries at zero molecule density. Approximating the cell as a sphere of radius r_c, we look for the solutions to

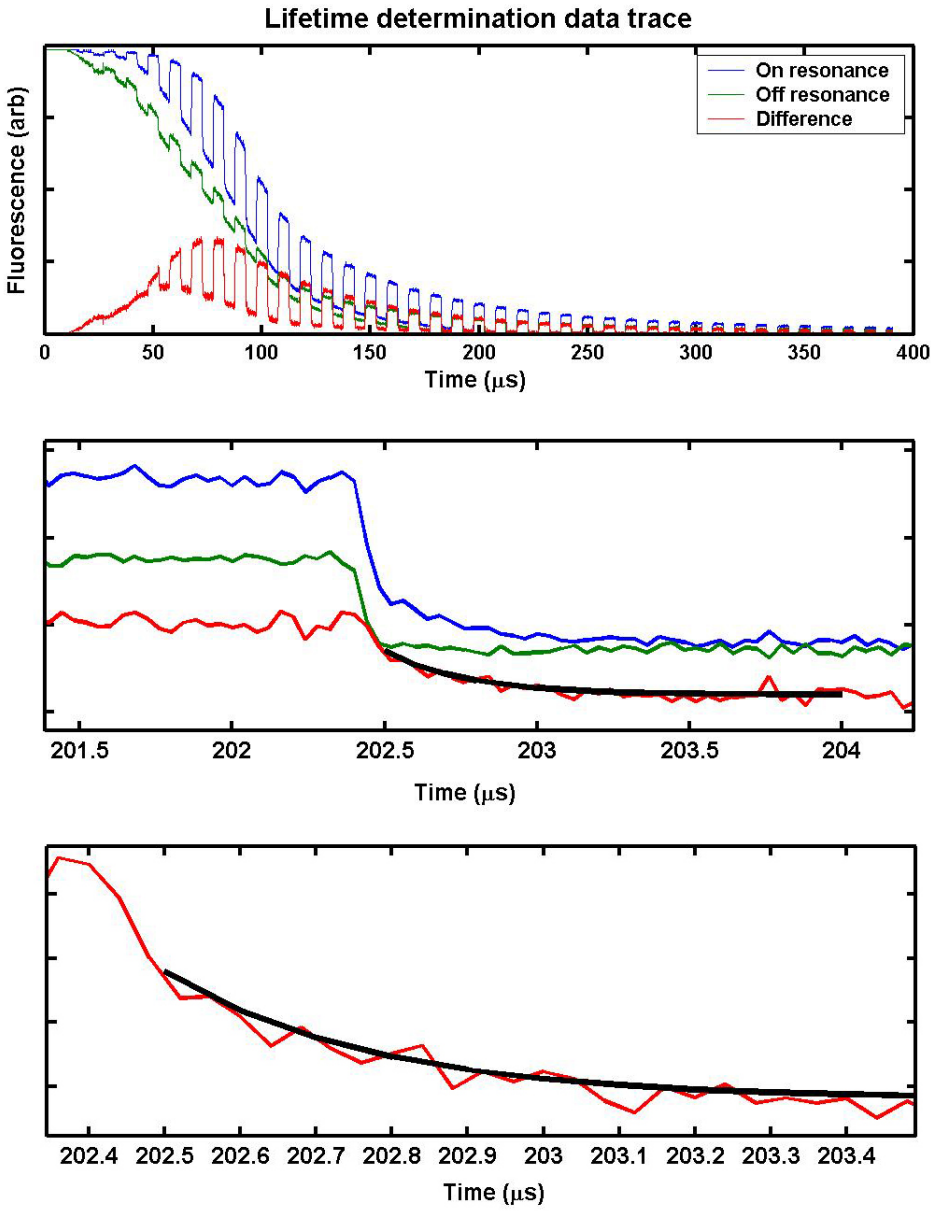

Figure 4.4: Data set from the experiment to determine the lifetime τ of the $|A^1\Sigma, J' = 1, v'' = 1\rangle$ state. Absorption traces (not shown) before and after affirm that the pump laser remained on resonance, and the that target remained fresh. Top, fluorescence on resonance (blue) and off resonance (green), are subtracted (red) to eliminate scatter and plume effects. Bottom, close up of a single decay and a fitted exponential (black). To find the lifetime, the difference was fitted to an exponential of form $A\exp[-((t-B)/\tau)]$ where the amplitude A and initial position of the decay B were also found as fitting parameters.

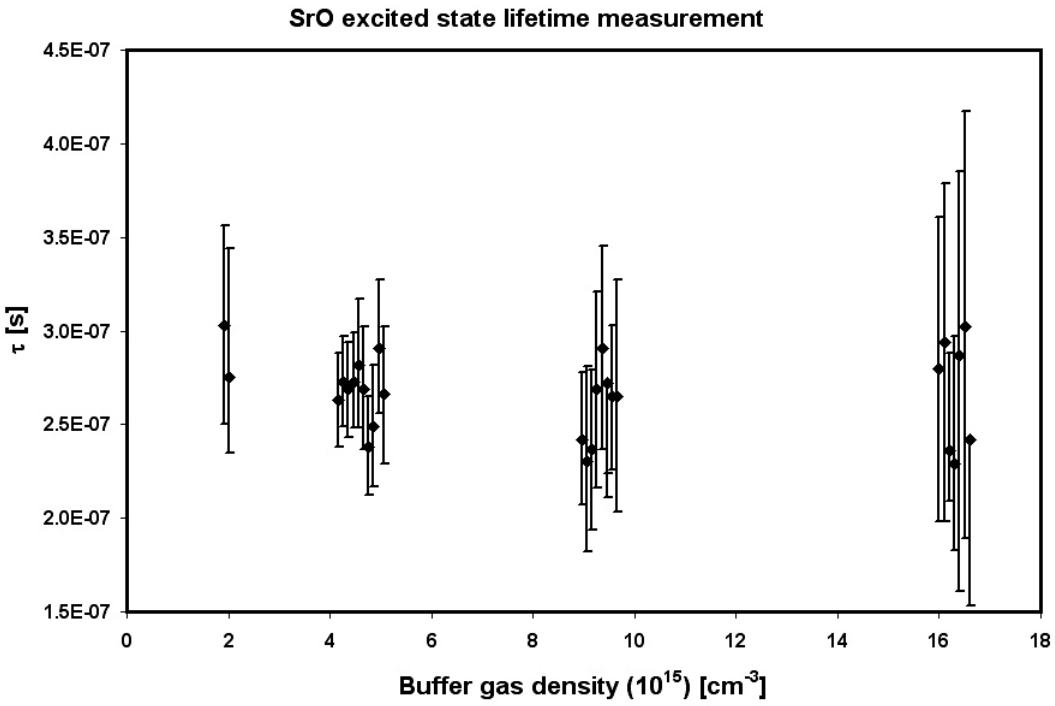

Figure 4.5: Accumulated lifetime measurement data for the SrO excited $|A^1\Sigma, J' = 10, v'' = 1\rangle$ state. Data points taken over a range of cell helium densities (2, 4, 9 and 16 $\times 10^{16}$ cm^{-3}) and increasing temporal delay (left to right separation) from ablation show no variation and give a mean lifetime of $\tau = 270 \pm 20$ ns. Error bars indicate fitting routine 90% confidence levels.

the 3D diffusion equation

$$\frac{\partial n_{SrO}}{\partial t} = D\nabla^2 n_{SrO}\,, \tag{4.10}$$

where D is the diffusion constant at temperature T, given by [76]

$$D = \frac{3}{16 n_{He}\sigma_{SrO-He}}\sqrt{\frac{2\pi k_B T}{\mu}}\,. \tag{4.11}$$

Here $\mu \equiv \frac{m_{He}m_{SrO}}{m_{He}+m_{SrO}}$ is the reduced mass of the colliding pair and n_{He} is the density of the helium buffer gas. The general solution is given by [76]

$$n_{SrO}(r,t) = \sum_{k=1}^{\infty}\frac{C_k}{r}\sin\left[\frac{r}{\sqrt{D\,T_{a,k}}}\right]\exp\left[\frac{-t}{T_{a,k}}\right]\,, \tag{4.12}$$

where

$$\frac{r_c}{\sqrt{D\,T_{a,k}}} = k\pi\,. \tag{4.13}$$

We immediately see that this set satisfies the boundary condition that the density goes to zero on the walls, $n_{SrO}(r_c,t) = 0$. The longest-lived mode has $k = 1$; at long times, even if many $k > 1$ modes are initially populated, the density should decay exponentially as $n_{SrO}(r, t\to\infty) \propto \exp\left[\frac{-t}{T_{a,1}}\right]$. Observation of the in-cell absorption at long times should follow the same time dependence because once the cell is filled the optical path length remains constant at the length of the cell (r_c). The absorption can then be fit to a decaying exponential and the time constant $T_{a,1}$ extracted. Then, the diffusion constant $D = \frac{r_c^2}{\pi^2 T_{a,1}}$, and hence the collision cross section σ_{SrO-He} can also be inferred. A characteristic exponential fit is shown in figure 4.6 and the full results from this experiment are presented in figure 4.7 for a range of in-cell buffer gas densities.

Surprisingly, the calculated value of σ_{SrO-He} from the measured decay is not constant over buffer gas density variation. To understand this behavior, the buffer gas code simulating the thermalization process was rerun. This simulation *fixed* $\sigma_{SrO-He} = 10^{-14}$ cm^2 in its code. Slight program modifications allowed the total

number of molecules passing through a 4 mm^2 area midway through the cell to be tracked as a function of time, just as an absorption laser measurement would. As in the real cell, if the molecules made it to the wall in the simulation, they "stuck" and were not tracked further. The behavior of the long-time decay in the simulation was also found to be exponential. Fitting to this, just as for the actual data, provided a similar behavior to the measured cross section. The extracted value of σ_{SrO-He} matched the input value of 10^{-14} cm^2 for high buffer gas densities and became independent of buffer gas density as expected. Insight from the simulations leads us to believe that the spurious cross sections result from cases when the probe distance is closer than the thermalization distance. From the measurements, then, we estimate the cold collision cross section between SrO and He to be $\sigma_{SrO-He} = 5 \times 10^{-15}$ cm^2. However, there are large enough uncertainties associated with the in-cell determination of the buffer gas density and from matching the spherical model assumption experimental from our geometry that we take this measurement to have an uncertainty of a factor of two.

4.5 Saturation intensity

One surprising observation about the buffer gas cooling process and its characterization is that of a large saturation intensity for absorption measurements. The saturation intensity describes the change in absorption due to optical pumping effects. Typically, these effects become important when the laser excitation rate equals the relaxation rate into the ground state. For a typical ($J' \simeq J'+1$) transition (calculated in more detail above), the resonant absorption cross section for molecules at rest is

$$\sigma_{\text{abs}} \simeq \frac{\lambda^2}{2\pi}\text{FCF}[v', v''] \,. \tag{4.14}$$

Taking the SrO transition with wavelength $\lambda = 785$ nm and FCF$[0, 3] = 0.1$, we find $\sigma_{\text{abs}} \sim 10^{-10}$ cm^2. The photon flux Φ for a typical $I = 10$ mW/cm^2 intensity used in

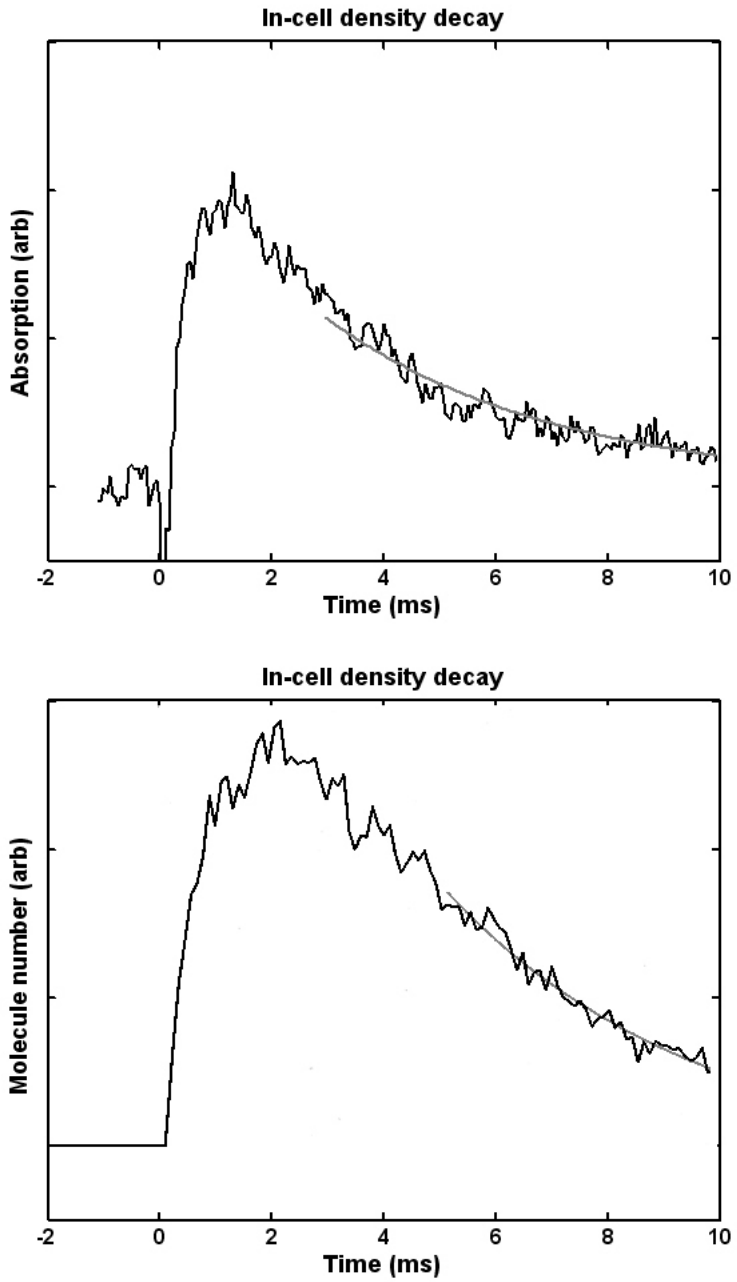

Figure 4.6: Characteristic data from the SrO-He cross section determination. Top, time-resolved absorption trace and exponential fit (light curve) for an in-cell density of 5.5×10^{15} cm^{-3}. The fit to the data yields a cross section of 1.3×10^{-14} cm^2. Bottom, number of molecules inside a detection "slice" for the buffer gas simulation (black) and exponential fit (red) for an in-cell density of 4×10^{15} cm^{-3}. The fit to the data yields a cross section of 1.2×10^{-14} cm^2.

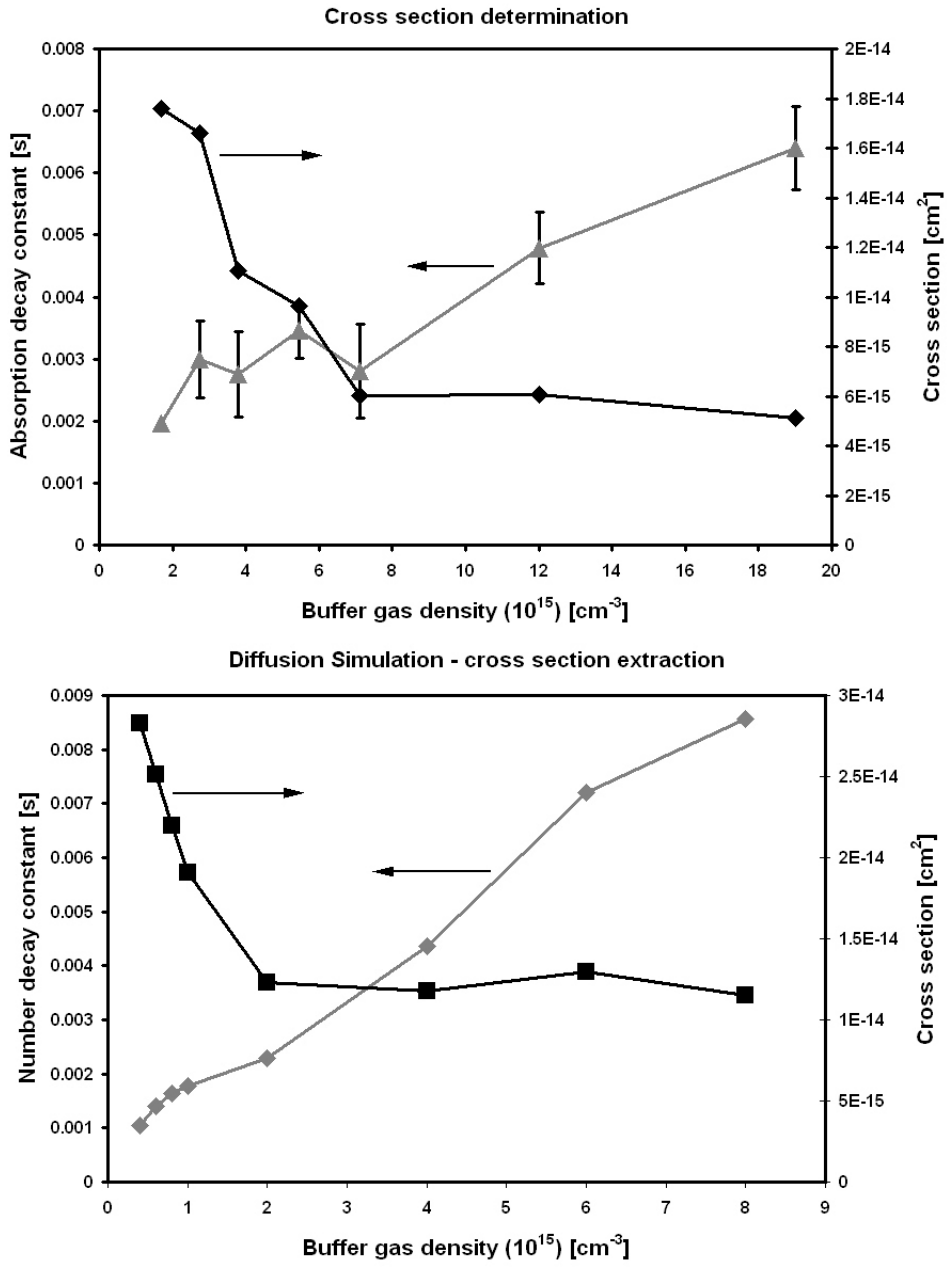

Figure 4.7: SrO-He cold cross section determination. Top, fitted absorption decay lifetimes (diamonds) and the calculated He-SrO cross section (squares) from measurements in the 4 K buffer gas-cooled cell. Error bars represent fitting confidence levels. Bottom, the same for the results of computer simulation data. Both show a large apparent buffer gas dependence when the detection laser (or simulation "detection" slice) is located less than one thermalization distance away, but approach a constant value when larger buffer gas densities thermalize the molecules before the detection point.

our experiments, is $\Phi \sim 4 \times 10^{16}$ so that the excitation rate W for a monochromatic laser beam is

$$W = \sigma_{\rm abs}\, \Phi = 4 \times 10^6\, {\rm s}^{-1}\,. \tag{4.15}$$

If the laser beam is spectrally broader (with width $\gamma_{\rm laser}$) than the natural linewidth of the transition (width $\gamma_{\rm nat}$), then many velocity classes are addressed and the on-resonance excitation rate will drop by $\sim \gamma_{\rm nat}/\gamma_{\rm laser}$. For our in-cell absorption setup we routinely used intensities this high ($W = 4 \times 10^6\, {\rm s}^{-1}$, with $\gamma_{\rm nat}/\gamma_{\rm laser} \simeq 1/3$ in our setup) *without* any evidence that saturation (bleaching or broadening) was occurring. This means that molecules are entering the interacting state at a rate as fast as the optical pumping rate, since optical pumping effects were not seen. Given that the natural lifetime of the excited state is $\tau = 270$ ns, this may not seem surprising, since natural relaxation into the interacting state could repopulate it. However, the decay of the excited state has many channels, to different ground vibrational and rotational states. Radiative decay of these states is slow [77], in the many millisecond range, disallowing this as a viable candidate for relaxation. In other words, the optical pumping is to "dark" states. Since this effect has also been seen in other buffer gas experiments [78], there may be a common mechanism that enhances the relaxation rate relevant to saturation. Molecular time of flight through the probe is much too slow to replenish the beam; even when neglecting diffusion the 4.2 K velocity through the 1 mm probe laser beam gives a time of flight only of 3×10^{-5} s.

It is possible that collisions with helium could change the SrO velocity at a fast enough rate so that as the resonant velocity class of atoms is optically pumped, a "velocity-changing collision" replenishes this depletion of the resonant velocity class with molecules from the other non-resonant classes. SrO-He collisions happen with a mean time $\tau_{coll} = 1/n\sigma_{SrO-He}\bar{v}$, where $\bar{v}$ is the mean relative velocity between the species. At 4.2 K, taking the collision cross section as $\sigma_{SrO-He} = 10^{-14}$ cm^2, and

buffer gas density as $n = 10^{16}$ cm^{-3}, the mean collision is $\tau_{coll} \sim 5 \times 10^{-7}$ s. This is in the right order of magnitude if the collisions can be considered velocity-changing. To determine if this is the case we consider a single head-on collision between SrO and helium. Here the collsion changes the SrO velocity by ∼10 m/s. The linear Doppler shift associated with this velocity change is ∼12 MHz. Although not all collisions are head-on, it is clear that on the order of one collision will shift the SrO resonant frequency by our laser linewidth of 10 MHz. Thus these collisions are a good candidate for quenching saturation in our experiments.

Another, possibly greater, source of molecules than those in other velocity classes are those in the many nearby non-resonant rotational states. Since rotational and translational thermalization occur with similar cross sections [51], SrO-He collisions also replenish the depleted state, this time from the other ground rotational states. Even at 4.2 K any given SrO rotational state population is but a fraction of the total (1–10%), thus the reservoir of molecules for state-relaxation collisions is quite large. Combined with the velocity changing collisions above, it seems reasonable that collisions are indeed the cause for quenching of our saturation and that this effect should be studied with either larger laser intensities, or in the regime of fewer collisions. The latter has been done, in the molecular beam. In this case, clear evidence of optical pumping effects occurs, with a saturation behavior that indicates the lack of these collisional effects.

4.6 Buffer gas molecular beam

Characterization of the buffer gas beam was done with the laser-induced fluorescence setup shown in figure 4.8. Here, the main desired measurements are the number of molecules in the beam, its forward velocity, and the temperature of the beam for various degrees of freedom. These measurements are ultimately what will determine

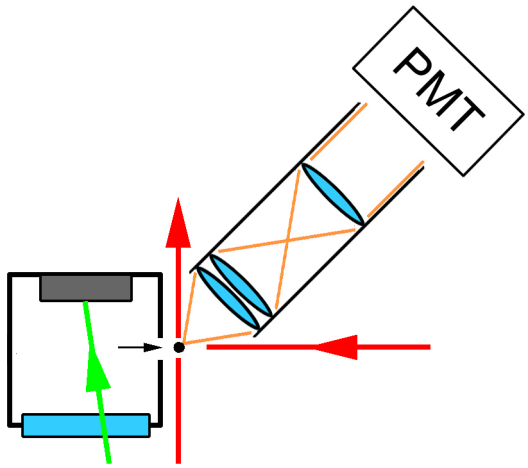

Figure 4.8: Setup of the buffer gas beam measurements. Pump beams (red) pass perpendicular to (vertical) and along (horizontal) the molecular beam (black arrow). Lenses collect light from a tight focal region (black dot) and collimate it out to the PMT detector. Several alignment techniques (not shown) ensure that the pump beams and detection lenses are aligned with the desired focal region just outside the cell orifice.

the usefulness of the buffer gas beam as a source for loading traps or other beam experiments.

4.6.1 Beam flux

The measurement of the flux of molecules in the beam is basically a counting problem. The problem is in counting them! Although as stated earlier, fluorescence detection can reach sensitivity at the single molecule level, this usually means counting single photons. This is because signal sizes are hampered by a number of technical and physical issues. One primary limitation in detection of our SrO molecules is the many decay channels that the excited state can decay by. Ultimately, the decay channels to states other than (i.e. with the initial rotation and vibration quantum number) the resonant ground state are lost from the system. In SrO, for excitation on the $\lambda = 785$ nm transition, the Franck-Condon factor for decay back to the vibrational

ground state is FCF$[v' = 0, v'' = 3] = 0.10$. Compound this with rotational branching ratios (typically 50%) and to a good approximation after only a *single* excitation, the SrO molecule is lost to further detection. This actually simplifies the counting in one way: there will be at most one photon produced per molecule (collisions were determined not to be an issue in the beam measurement due to direct observation of saturation).

The flux of photons N_γ actually detected is then the product of the beam parameters, and a number of efficiencies. We expand the probe frequency ω and time t dependent N_γ as;

$$N_\gamma(\omega, t) = N(t) \times f_J(T) \times f(v, \omega, P) \times \mathrm{FCF}[v'', v'] \times d\Omega \times \eta_{\mathrm{Opt}} \times \eta_{\mathrm{QE}}\,. \quad (4.16)$$

The parameters are defined in table 4.1. The last four parameters are the measured technical efficiencies of the detection system, limiting the overall detection efficiency to $\eta \approx 6.5{\times}10^{-5}$. The first three parameters encode the desired beam properties: flux, rotational temperature, and velocity distribution, assuming that they are independent of one another. Measuring the time-resolved photon flux immediately shows the time characteristics of the molecular beam at the probe point, since the fluorescence occurs very fast compared to the time of flight needed to travel any appreciable distance. A sample oscilloscope trace showing a time resolved fluorescence signal is shown in figure 4.9.

4.6.2 Rotational temperature

Measuring the rotational temperature consists of fitting the relative height of several spectral line peaks to the the heights expected for a given rotational Boltzmann distribution of temperature T. The form of this fit is given by:

$$f_J(T) = A\, 2(J' + 1) \exp\left[\frac{-B_e\, J'(J' + 1)}{k_b\, T}\right] \quad (4.17)$$

Parameter	definition	dependent on	value
$N(t)$	total molecule number	production and extraction yield and evolution time	—
$f_J(T)$	fraction in state J	beam rotational temp	—
$f(v, \omega, P)$	fraction excited by pump	beam velocity distribution laser frequency and power	—
FCF$[v'', v']$	Franck-Condon for decay	v"=3, v'=1	.163
$d\Omega$	detection solid angle	collection optics	0.02
η_{Opt}	detection filter efficiencies	filters	0.5
η_{QE}	quantum efficiency of PMT	PMT QE at 830nm	0.04

Table 4.1: Parameters involved in the molecule beam fluorescence detection.

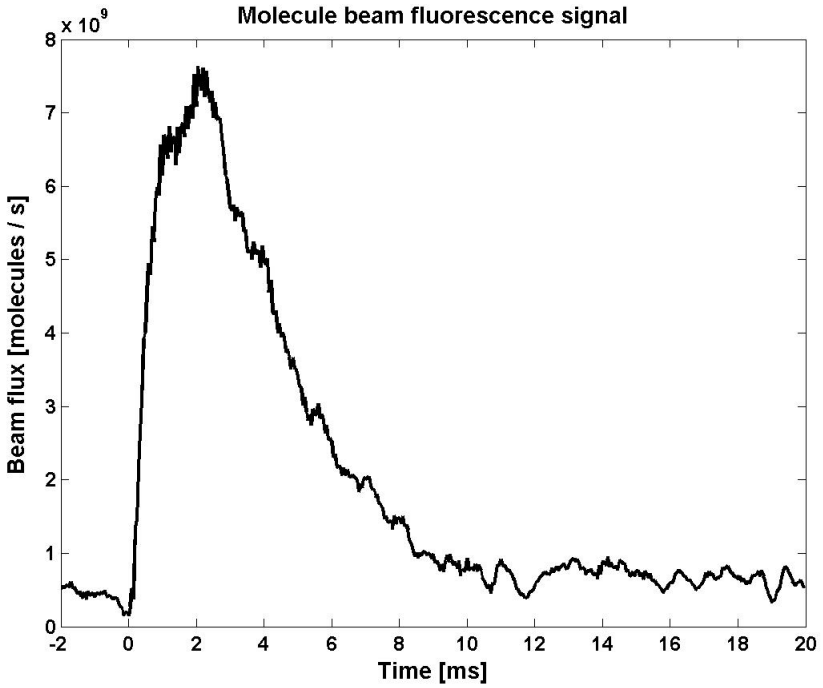

Figure 4.9: Typical fluorescence data. Experimental conditions for this data are: 5 cm cell, 3 mm diameter aperture, $|J' = 0, v' = 0\rangle \rightarrow |J'' = 1, v'' = 3.\rangle$ transition, 2×10^{16} cm^{-3} in-cell helium density.

where B_e and k_b are the rotational and Boltzmann constants, J' is the ground state rotational quantum number, and A and T are the fitting parameters describing the normalization and temperature of the beam distribution. It was expected that the exiting beam, as long as it was thermalized, would assume the buffer gas temperature, and indeed this was the case; for all cell and aperture sizes investigated, the rotational temperature was roughly consistent with 4.2 K, and showed no trend away from this temperature as the in-cell buffer gas density was changed (over a full decade). This is shown in figure 4.10.

4.6.3 Velocity distribution

When the flow of a gas exiting a source is collisionless it is in what is called the molecular flow regime. The condition for this type of flow is that the aperture is small in diameter and also thin compared to a mean free path. In this situation it is clear that this flow will not perturb the equilibrium density and temperature inside the cell. Thus with the molecular flow assumption, the flow and velocity distribution of molecules exiting the cell is the same as that for normal collisions with the cell walls [60, 51].

The gas inside the cell has a Maxwell-Boltzmann speed distribution, $f(u) = \frac{4}{\sqrt{\pi}} u^2 e^{-u^2}$, where $u = v/\tilde{v}$ and $\tilde{v} \equiv \sqrt{\frac{2kT}{m}}$. Using this, the rate of particles leaving the cell into solid angle $d\omega$ with angle θ with respect to the normal of the orifice area A is

$$\frac{dN(\theta, u)}{dt} = \frac{n_0}{\pi^{3/2}} A\, \tilde{v}\, u^3\, e^{-u^2} \cos(\theta)\, du\, d\omega\,, \tag{4.18}$$

where n_0 is the density just inside the cell. Writing this in terms of Cartesian coordinates ($\hat{z}$ along orifice normal) gives,

$$\frac{dN(\theta, u)}{dt} = \frac{n_0}{\pi^{3/2}} A\, \tilde{v}\, (e^{-u_x^2} du_x)\, (e^{-u_y^2} du_y)\, (u_z e^{-u_z^2} du_z)\,. \tag{4.19}$$

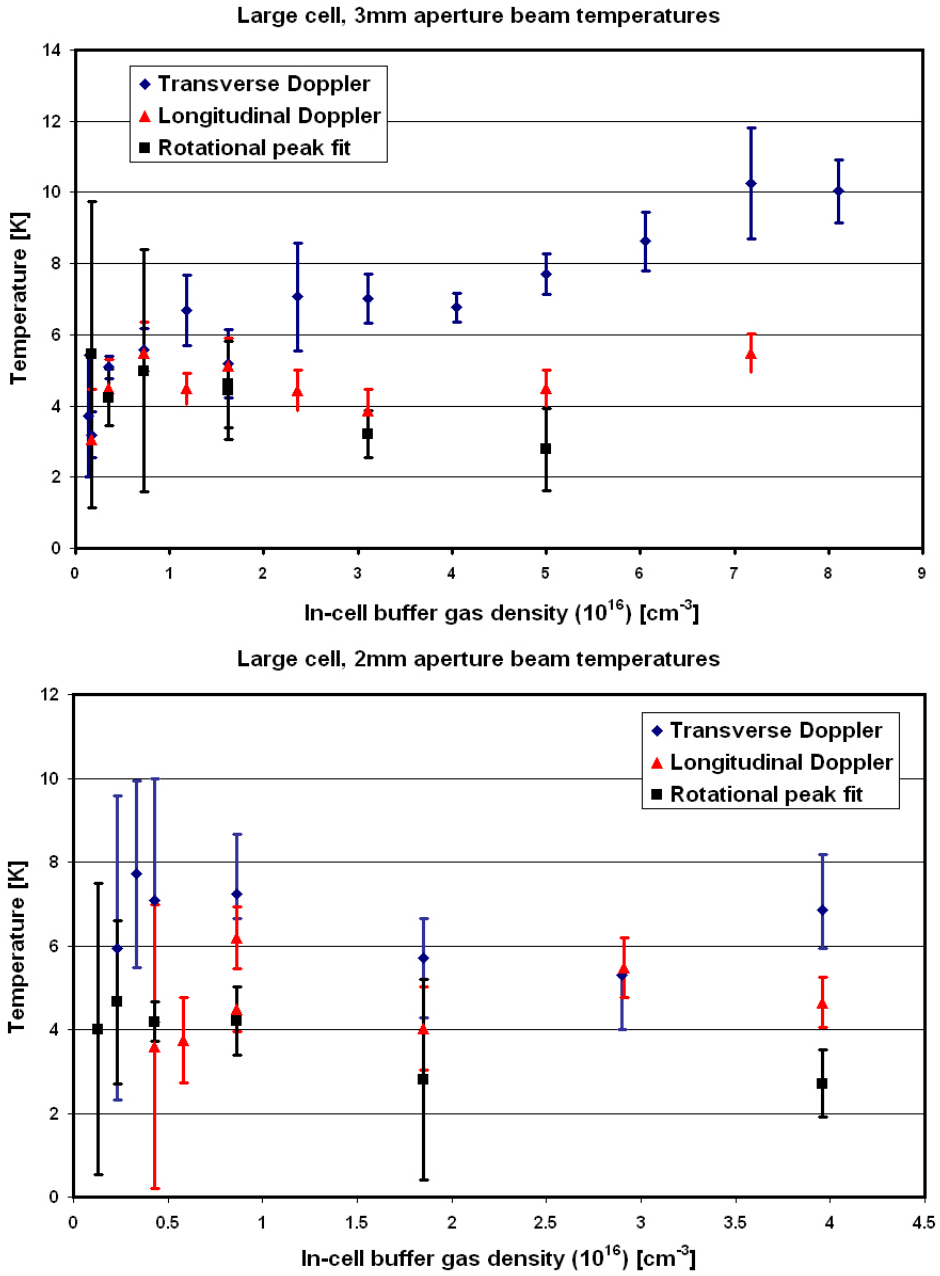

Figure 4.10: Molecular beam temperature characterization. Transverse Doppler temperature, longitudinal Doppler temperature, and rotational temperatures for the large cell with 3 mm and 2 mm apertures is shown as a function of in-cell buffer gas density. The error bars indicate fitting routine confidence levels. With one exception, all temperatures are roughly constant and consistent with 4.2 K over the variation of in-cell buffer gas densities. The positive transverse temperature trend for the 3 mm cell is likely due to collisions with helium (see discussion in section 4.6.3).

From this form we can immediately see the molecular flow velocity distributions both in the beam direction ($\hat{z}$), and in the directions transverse to it. For helium, the condition for molecular flow is that the mean free path with other helium be smaller than the diameter and thickness of the orifice. By contrast, the condition for molecular SrO flow is that *its* mean free path with *helium* be smaller than the diameter and thickness of the orifice, since the collisions will be with helium. In this true limit each species will follow the distribution of equation of equation 4.19, yet $\tilde{v}$ will be different for the two species due to the mass difference. This rigid assumption of molecular flow, however, is not valid for many of the explored experimental conditions, for both species, for reasons discussed later. However, since the transition to continuum flow is quite broad, at least the helium flow will be assumed to be effusive. The molecular velocity distribution, then, will depend on the collision dynamics between the SrO and the helium at the exit.

One additional note of interest for these measurements concerns the geometry of the probe and fluorescence detection. If the detection point is directly at the aperture, the detection may be assumed to address the entire distribution of molecules. However, for detection at places other than the aperture the detected velocity distributions may be limited geometrically. For example, for a spatially compact detection region downstream along the beam axis, molecules with large transverse velocities relative to the forward velocity will not reach the detection region. In this case, careful scrutiny should be given to the transverse velocity distribution inferred from the fluorescence measurements. For these measurements, detection was as close to the aperture as possible so that we assume that we address and detect the entire distribution of molecules.

Transverse distribution

Inside the orifice, even if there are collisions between SrO and the helium, there is no transverse flow of helium, due to the confinement of the aperture walls. Due to this and the lack of geometric constraints, as described above, detection there should reveal a Gaussian 4.2 K velocity distribution. This assumes that the Doppler broadening is much larger than the laser linewidth and any power broadening effects; this was verified to be true in our case by measuring the laser linewidth and varying the laser power and looking for broadening of the spectrum. In order to measure the velocity distribution, then, the locked laser was swept through the fluorescence line and the fluorescence lineshape was fitted to a Gaussian. Results are shown for the large buffer gas cell in figure 4.10. These data show no trend away from 4.2 K for the 2 mm aperture, but a slight upward trend for the 3 mm aperture. In the latter, the detection was taken about 1 hole diameter (3 mm) away from the actual exit; thus collisions with the fast-moving helium may speed up the SrO.

Forward velocity distribution

Collisional effects disturbing the forward velocity distribution are a much greater concern. This is because the helium exiting the aperture exhibits a "bulk flow", that is each helium gas atom has an average forward velocity. This velocity of the bulk preferentially boosts the molecules in the forward direction. The mean free path, governed by the helium density, dictates the average collision length. As before, if the act of exiting the buffer cell is collisionless, then also the forward velocity distribution of molecules exiting the source should match the 4.2 K molecular flow source distribution described above. We initially tried to reach this condition by using small apertures, but in order to detect any molecules outside the cell, found it was necessary to enlarge the aperture so that it was larger than the SrO-helium mean free

path. Since we no longer expected the source to be effusive for these conditions, we measured the forward velocity distribution via fluorescence spectroscopy in a manner similar to the transverse case, except for these measurements the pump laser beam is pointed directly at into cell aperture in order to measure the associated linear Doppler frequency shift Δf of the forward motion v_z given by,

$$\Delta f = \frac{v_z}{\lambda_0}, \tag{4.20}$$

where λ_0 is the resonant optical wavelength.

It was found that the forward velocity distribution of SrO in the beam resembled a Gaussian of roughly $T_f = 4.2$ K (see figure 4.10) with a forward offset "boost" that depended on the in-cell buffer gas density. The temperature of this degree of freedom was found from a fit to the width of the distribution and the forward offset was found from Doppler shift associated with the spectroscopic frequency shift between the longitudinal and forward distributions. Not surprisingly, the actual boost depended on the ratio of the diameter d_h of the aperture to the mean free path λ between SrO and helium. This sets the number of collisions that molecule undergoes as it exits the cell at d_h/λ.

Up to this point in the thesis the molecule-helium mean free path has been stated as the standard one found in the literature $\lambda = \frac{1}{n\,\sigma_{SrO-He}}$. This expression implicitly assumes that the velocities of the two particles are the same. For SrO and He at different velocities the true mean free path (of the SrO) is $\lambda^\dagger = \frac{v_{SrO}}{n\,\sigma_{SrO-He}\,v_{\rm rel}}$, where $v_{\rm rel}$ is the relative velocity between the SrO and helium. With this definition of mean free path we first see that the criterion for collisionless flow is more stringent than before because in general $v_{SrO} < v_{\rm rel}$ due to the mass difference. A crude model of the boost process sets exactly one "boost-collision" each $\lambda^\dagger$ over a distance d_h. For simplicity the model assumes constant helium density over this length and also a constant forward helium velocity equal to its mean effusive beam velocity. The collision is taken as an

elastic collision of the helium with the SrO directly from behind (conservation of 1D momentum and energy in the forward direction $\hat{z}$). Moreover, in the model only a few collisions are enough to raise the SrO forward velocity substantially (and change the relative velocities as well), thus $\lambda^{\dagger}$ is not constant over the process. However, the SrO velocity and total distance traveled can be tracked for increasing collision number in an iterative manner. For large numbers of collisions the modeled SrO forward velocity indeed matches that of the helium, as expected for a fully entrained beam. Good agreement with the observed forward velocity of the SrO beam when the cross section for this process is $\sigma_{SrO-He} = 0.25 \times 10^{-14}$ cm^2, is found with the model. This is shown in figure 4.11.

For large buffer gas densities, the observed SrO forward velocity actually rises above the helium effusive velocity. This is likely the case for one of the following reasons, either the helium begins to form a supersonic beam, or the high helium flows provide too large a heat load on the cryogenics and the system actually begins to warm.

Divergence of the molecular beam

One interesting observation in the buffer gas beam velocity distributions is the asymmetry of the fast forward velocity versus the slow transverse velocities. For the 2 mm exit aperture diameter, for example, it is quite clear that the transverse temperatures (and thus velocities) do not rise, even when the beam reaches the large boost up the helium effusive velocity. This combination of velocities provides a very directed beam. If true, this would indicate a remarkable enhancement of the flux of molecules on the axis of a long beam. It is possible that the detection geometry limited the transverse velocity detected, and hence that this apparent beam collimation is an artifact of our measurement. However, it also possible to envision a situation where, outside the cell,

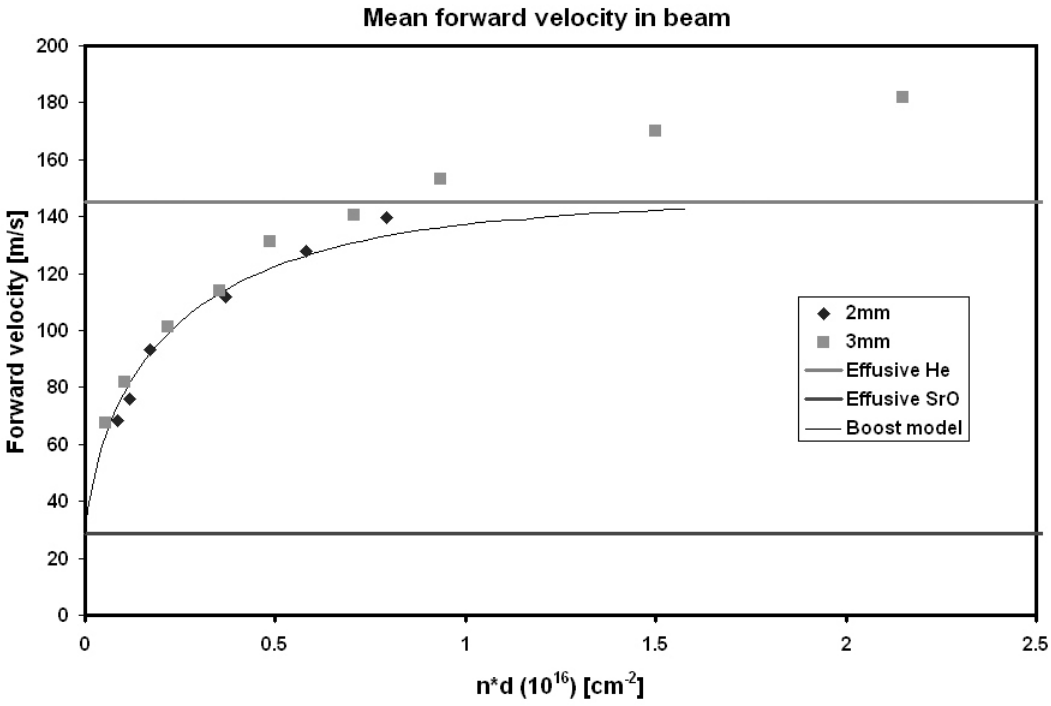

Figure 4.11: Forward velocity boost in the molecular beam as a function of the in-cell helium density n, hole diameter d, product. Collisions with helium boost the forward velocity of the SrO from its effusive value (30 m/s) towards the helium effusive velocity (145 m/s). A simple 1D model of collisions reproduces this boost quite well. The actual forward velocity goes above the helium effusive limit at sufficiently high helium densities. This is either due to non-molecular helium flow since the helium also enters transitional flow for these conditions, or to actual warming of the cell due to large heat loads.

the helium density drops fast enough so that collisions outside the cell are few. Here the boost forms during the plentiful collisions in the aperture but collisions leading to large transverse velocities (outside the cell) do not occur. A final possibility is that the boost forms inside the aperture (or inside the cell for that matter) and only outside the cell can collisions increase the transverse temperature. To see this effect necessarily means looking away from the exit. To definitively answer which of these is the case, the velocity distributions should be measured at several points along the beam axis. Currently the apparatus is being redesigned and set up to answer such a question.

4.6.4 Enhanced yield observation

In order to measure the molecular beam extraction yield, the fluorescence of molecules was integrated over the time of the molecular pulse. In addition, since it was difficult to estimate the level of power broadening in the detection, the laser beam power was raised as high as possible and its frequency was modulated via modulation of its current. This was done in an attempt to detect (pump) *all* velocity classes of the molecules when on resonance, thus giving a calibrated yield. Verification of this technique was done by increasing the modulation depth of the laser and observing the on-resonance fluorescence signal. When the signal rose as modulation increased, this was due to pumping of a larger range of velocity classes with the laser. When the signal plateaued as the modulation increased this was because all of the molecules were being pumped by the modulated beam. If the signal fell before plateauing as the modulation increased, it would be because too much pump laser power was concentrated at large modulation depths away from resonance, decreasing the pumping probability. The plateau in signal size, and a flattened fluorescence lineshape (associated with a unit pumping probability for a range of frequencies) were verified in

observation when modulating the laser. This calibrated the velocity distributions for yield calculations: the rotational state distribution still remained, but the few populated states could be summed or the total calculated if the beam temperature was known from other measurements.

As stated earlier, in order to see a molecular beam fluorescence signal, it was necessary to enlarge the size of the aperture beyond the condition for molecular flow. Once signals were seen however, they were significantly enhanced relative to the expected geometric extraction (see section 2.4.3). In the geometry with a $d_h = 3$ mm diameter hole and $D = 5$ cm diameter cell, when all totaled, roughly 1% of the total molecules made it into the beam! This is clearly a departure from the $\sim$0.1% expected in the geometric limit. Further, extraction of the beam did not fall off with high helium densities, rather it plateaued. In addition, when smaller apertures were again tried, the flux did not scale with the area of the aperture, as expected geometrically. For example, scaling down the diameter of the aperture from $d_h = 3$ mm to $d_h = 2$ mm ($3^2/2^2 = 2.23$ area ratio) reduced the flux plateau by 4.6×. In addition, scaling down to $d_h = 1$ mm eliminated the signal altogether ($< 10^{-4}$ extraction). A further oddity is the same flux produced by *both* apertures at low in-cell densities.

This behavior led us to believe that the flux is being enhanced by some sort of hydrodynamic flow inside the cell. Similarly described effects were seen in buffer gas experiments in the Doyle labs when they quickly remove helium from the buffer gas cell (in this case the removal of the helium detrimentally drags the atoms with it when they were already in-place). One proposed mechanism for this enhancement [79] relates the time it takes the in-cell molecule density to decay, τ_{Diff}, to the average amount of time that the a helium particle spends inside the cell, the so-called "pumpout" time τ_{pump}. In this model, the decay time is just the diffusion lifetime presented above in equation 4.13: $\tau_{\text{Diff}} = T_{a,1}$. The pumpout time is proportional to

the ratio of cell volume to aperture area: $\tau_{\rm pump} \propto V_{\rm cell}/A_{\rm hole}$. The dimensionless ratio of these times exhibiting the scaling is then

$$\frac{\tau_{\rm Diff}}{\tau_{\rm pump}} \propto \frac{A_{\rm hole}}{\lambda\, D} \propto \frac{{d_h}^2\, n}{D}\,, \tag{4.21}$$

where λ is the SrO-helium mean free path, n is the in-cell helium density, and D is the size of the cell. When this ratio is large, one can anticipate that every He atom in the cell will leave before the molecule will have time to diffuse to the wall. Thus if the molecule is caught up in the helium "wind" the enhancement of molecular extraction into the beam will be large.

Therefore, it was anticipated that increasing the aperture size beyond $d_h = 3$ mm would increase the hydrodynamic effect and the extraction beyond 1%. The hope was that nearly 100% of the molecules could be extracted. However, since the heat loads on the cryogenic system (due to the gas loads) and gas flows (due to poor vacuum) for any larger apertures were prohibitively large, the alternative of reducing the cell size was tried. The same measurements as described above were then carried out in a cell that was one half the size $D = 2.5$ cm. To date the results in the small cell suffer from calibration issues, yet indications are that the yield does improve. Still, as described, the total number of molecules extracted into the beam (for the large cell) plateaus as described at $\sim$1% and did not continue to increase towards 100% as the in-cell density increased, in contrast with the simple model above. Thus the true scaling and the optimal geometry for efficient extraction remains a mystery and we continue to try to improve the detection in the small cell setup for additional measurements.

4.7 Summary and improvements

With these results the use of the buffer gas-cooled molecular beam for future experiments begins to take shape. In its current condition, the high ablation yield (10^{12}),

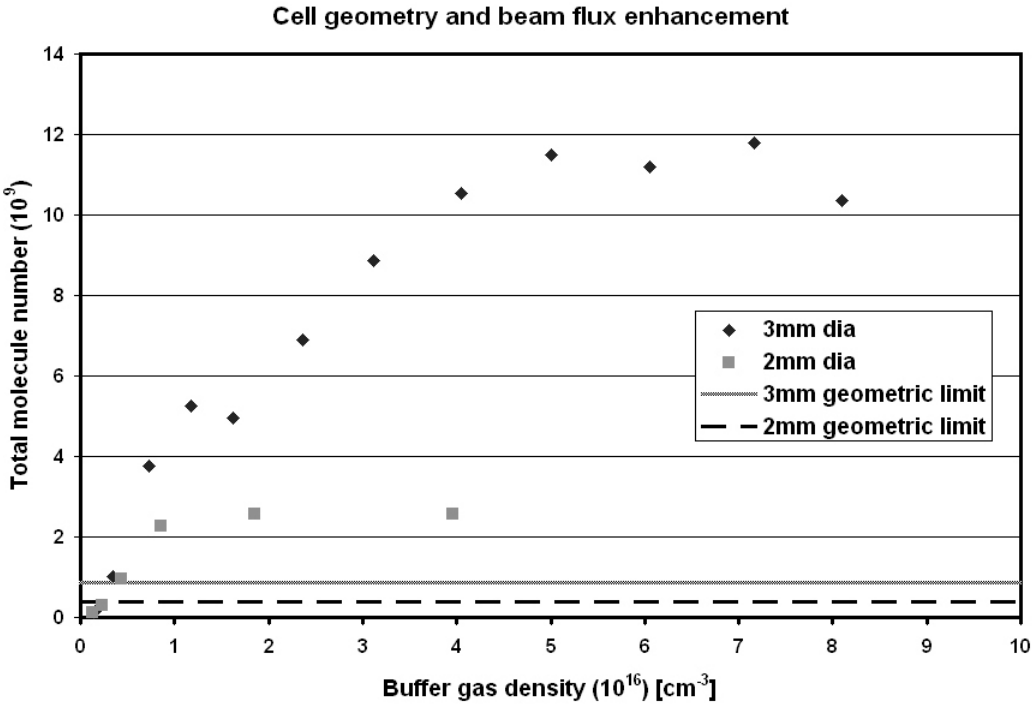

Figure 4.12: Molecule flux in the molecular beam as a function of buffer gas density for the 5 cm cell. Geometric extraction efficiencies (from equation 2.21) for 2 mm and 3 mm hole sizes are given by the dashed lines. At low helium density, the extraction efficiency is observed to be independent of hole size. For large helium density, the extraction plateaus, yet still does not scale with the area of the aperture. In both cases, the extraction plateau rises well above the geometric limit.

the high ablation repetition rate (100 Hz), the good beam extraction efficiency (1%), and the possible narrow divergence mean that $\sim 10^{12}$ molecules/second can be delivered in a highly directed beam. Given that this source is also cold ($T \sim 4.2$ K) in its velocity and rotational distributions only adds to its starting phase space density. This gives the buffer gas-cooled molecule beam excellent utility as a source for any experiment that relies mainly on counting statistics, such as precision measurements. Also, given its generality, this source could be used as the input for decelerators such as the Stark decelerator, allowing a wider range of species to be studied.

The possibility to reduce the forward velocity while maintaining the large flux enhancements [79] exists with more complicated geometries. For example, if the current aperture fed a second buffer gas cell with much lower density, it is possible that a few extra collisions with stationary helium could remove most of the forward energy from the current setup, while maintaining a drift toward the beam formation point. It also may be possible to do this by just by placing a semi-transparent mesh in the path of the boosted beam [79]. The mesh would create a small, non-moving, helium density that, again, would lead to just a few collisions with the boosted beam. Most of the beam could make it through the mesh if the transparency were large. In addition, use of a buffer gas below 4.2 K could slow the forward velocity of the beam, due to smaller buffer velocities. These enhancements seem necessary if trapping of the produced molecules is the final goal, because the energy in the boosted beam scales with the square of the forward velocity. As recapped in figure 4.13, for the most promising geometry, the forward velocity is simply too high, even for fluxes that are on the edge of detectability in our current setup.

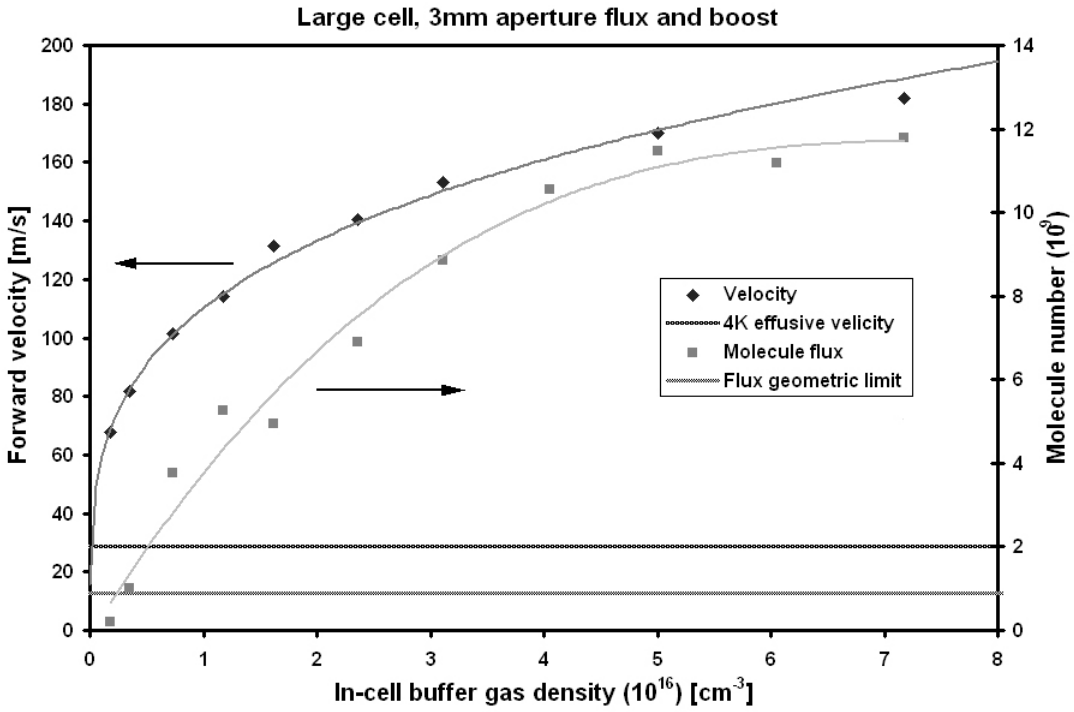

Figure 4.13: Beam flux and boost for the large cell, 3 mm aperture geometry as a function of in-cell buffer gas density.

Chapter 5

Beyond 4K: guiding and trapping

Given the interest in the applications described in the introductory chapter, it is highly desirable to produce molecules at temperatures much lower than 4 K. Presently, the methods described, including the buffer gas beam, cannot produce the combination of low enough temperatures and high phase space densities needed to be useful for those applications. Thus it is clear that using a buffer gas molecular beam, or any of the other direct cooling techniques, requires another stage of cooling to reach the ultimate desired temperatures. Trapping of the molecules and further cooling via sympathetic collisions or evaporation is the next logical step, and may in fact be the only workable method to bring to directly cooled molecules to the ultracold ($T < 1$ mK) regime.

To date, the other direct cooling methods, including in-cell buffer gas cooling, have concentrated on trapping molecules using the molecular magnetic moment in static field configurations, for example trapping of molecules in a magnetic field minimum. Such traps can have reasonable depths (a large field such as 2 Tesla produces a 1.3 K trap depth for a molecule with a 1 Bohr-magneton magnetic moment) and can be directly coupled to the molecule source. For instance, experiments to directly load such a trap superimposed on a buffer gas cell [49] has met with some success, although eliminating background collisions between trapped atoms and the helium buffer gas

was a major cryogenic challenge. Unfortunately, these traps suffer from an essential flaw. Since static field configurations can only trap molecules in a weak field seeking state, and this state for the molecular dipole is an excited state, collisions inside the trap can relax the molecule to the non-trapped ground state. Large inelastic collision rates in these traps (versus atomic samples) have thus precluded collisional cooling to proceed. Therefore, we are pursuing a new route to the ultracold regime, one that utilizes a trap for ground state molecules in a strong-field seeking configuration.

5.1 Guiding the molecules

Before we can begin to attempt trapping of the buffer gas cooled beam we must couple it to the trapping region. In the process we must also separate the molecules from the buffer gas. As the mingled beam of atoms and helium propagates away from the cell, its divergence ensures that the density of helium decreases as the square of the beam length, for long beams. The divergence of the molecules, however, also serves to reduce the molecular density in the same way. So unless the divergence of the two is different in some way [80] (c.f. section 4.6.3), forming a beam is not a way to separate the two species.

One way to maintain the flux of molecules and couple it to a trapping region while also pumping away the helium is to actively guide the molecular beam [47] (and not the helium beam). To effectively guide the molecules, field geometries that confine the molecules in two dimensions must be created. This can be done with forces either magnetic via the Zeeman effect, or electric via the Stark effect. Since we intend to study dipolar molecules, it naturally makes sense that we utilize their electric dipole moments for the interaction with which to guide. Since helium has a very small polarizability, it will not feel a much guiding force, thus the two species will be separated due to the helium beam's divergence.

However, a molecule in the absence of electric fields has no net dipole moment, $\vec{d}$. One way to see this is via a simple symmetry argument. The Wigner-Eckart theorem applied to vector operators states that the value of any vector operator (such as $\vec{d}$) must lie along the value of the total angular momentum (in this case $\vec{J}$). In the absence of an electric field, there is no preferred direction for the angular momentum, due to the rotational symmetry of space. Thus the expectation value of both vector quantities, $\langle\vec{d}\rangle$ and $\langle\vec{J}\rangle$ must equal zero.

5.1.1 DC Stark effect

When a field is applied, however, the molecule may polarize, leading to a definite orientation along the field and a non-zero interaction energy. This is the Stark effect. For small fields, perturbation theory using the Stark Hamiltonian H_{St} for the molecule dipole moment $\vec{d}$ interacting with an electric field $\vec{\mathcal{E}}$

$$H_{St} = -\vec{d}\cdot\vec{\mathcal{E}}\,, \tag{5.1}$$

can be used. By the argument above, since the dipole moment vanishes when no field is applied, the first-order perturbation shifts due to H_{st} also vanish. Calculation of the second order perturbation shifts can be performed. These calculations will be valid only when the fields are small, so that the perturbing shift of a polarized molecule is much smaller than the rotational energy spacing B_e, i.e., when

$$d\mathcal{E} \ll B_e\,. \tag{5.2}$$

However, molecules traversing a guide will experience a full range of field regimes, from a field zero at the center of the guide, to strong applied fields to guide molecules with the largest possible effect. Thus the full diagonalization of the molecular Stark Hamiltonian is necessary to give the full range of molecular energies over the region of the guide.

Full numerical the diagonalization of the Hamiltonian for the DC Stark effect proceeds as follows. The molecular energy level structure of the molecules gives the field free rotational Hamiltonian,

$$H_0 = B_e\, J(J+1)\,. \tag{5.3}$$

where we are considering here the simplified picture of a rigid rotor diatomic molecule (including SrO and other $^1\Sigma$ molecules). The states $|J,m\rangle$ of such molecules have spherical harmonic angular wavefunctions: $|J,m\rangle = Y_J^m(\theta,\phi)$. The vibrational and electronic states of the molecule are of sufficiently high energy that mixing to these states can be neglected. For simplicity we choose the field direction to lie along that of the m quantization ($\hat{z}$ direction) so that $\vec{\mathcal{E}} = \mathcal{E}\hat{z}$. Such a DC field can couple states only with the same magnetic quantum number m and rotational states J with $J \pm 1$. Since the absolute ground state of any system is a strong field seeking state, the lowest lying state to be weak field seeking (hence one that can be guided) will be the state $|J=1, m=0\rangle$. The field-mixed subspace containing this state are all states with m=0; these are the states we must keep for diagonalization. An infinite ladder of rotational states exists, but for computation we will truncate the subspace at a $J = J_{\max}$, where $J_{\max}$ is high lying enough that the additional effect of keeping more levels on the $|1,0\rangle$ state can be neglected. This condition is checked by varying the subspace and redoing the calculation.

The off-diagonal, Stark Hamiltonian matrix elements $\langle J',0|H_{St}|J,0\rangle$ are then

$$\begin{aligned}
\langle J',0|H_{St}|J,0\rangle &= -d\mathcal{E}\langle J',0|\cos\theta|J,0\rangle && (5.4)\\
&= -d\mathcal{E}\int d\Omega\, Y_{J'}^{0\,*}\cos\theta\, Y_J^0 && (5.5)\\
&= \begin{cases} -d\mathcal{E}\frac{J+1}{\sqrt{(2J+1)(2J+3)}} & (J'=J+1)\\ -d\mathcal{E}\frac{J}{\sqrt{(2J-1)(2J+1)}} & (J'=J-1)\end{cases} && (5.6)
\end{aligned}$$

When put into matrix form, then, the Hamiltonian of the field-molecule system $H_0 + H_{St}$ for $J_{\max} = 8$, $m = 0$ subspace is,

$$H_0 + H_{St} = \begin{pmatrix} 0 & \frac{d\mathcal{E}}{\sqrt{3}} & 0 & 0 & 0 & 0 & 0 & 0 & 0 \\ \frac{d\mathcal{E}}{\sqrt{3}} & 2B_e & \frac{2\,d\mathcal{E}}{\sqrt{15}} & 0 & 0 & 0 & 0 & 0 & 0 \\ 0 & \frac{2\,d\mathcal{E}}{\sqrt{15}} & 6B_e & \frac{3\,d\mathcal{E}}{\sqrt{35}} & 0 & 0 & 0 & 0 & 0 \\ 0 & 0 & \frac{3\,d\mathcal{E}}{\sqrt{35}} & 12B_e & \frac{4\,d\mathcal{E}}{3\sqrt{7}} & 0 & 0 & 0 & 0 \\ 0 & 0 & 0 & \frac{4\,d\mathcal{E}}{3\sqrt{7}} & 20B_e & \frac{5\,d\mathcal{E}}{3\sqrt{11}} & 0 & 0 & 0 \\ 0 & 0 & 0 & 0 & \frac{5\,d\mathcal{E}}{3\sqrt{11}} & 30B_e & \frac{6\,d\mathcal{E}}{\sqrt{143}} & 0 & 0 \\ 0 & 0 & 0 & 0 & 0 & \frac{6\,d\mathcal{E}}{\sqrt{143}} & 42B_e & \frac{7\,d\mathcal{E}}{\sqrt{195}} & 0 \\ 0 & 0 & 0 & 0 & 0 & 0 & \frac{7\,d\mathcal{E}}{\sqrt{195}} & 56B_e & \frac{8\,d\mathcal{E}}{\sqrt{255}} \\ 0 & 0 & 0 & 0 & 0 & 0 & 0 & \frac{8\,d\mathcal{E}}{\sqrt{255}} & 72B_e \end{pmatrix}, \quad (5.7)$$

where states are organized left to right, top to bottom with increasing J.

Numerical diagonalization of the matrix as a function of $d\mathcal{E}/B_e$ gives the eigenenergies of the molecules in the field. Figure 5.1 shows the results for various perturbation strengths. Note that the $|0,0\rangle$ state is a strong field seeking state, as expected, and $|1,0\rangle$ is the first weak field seeking state. All states show a quadratic Stark shift at low field. At larger fields, the ground state saturates to being fully polarized, while the excited states show a different general behavior. At first, for these states, since the nearest neighbor of any given state lies below it, the shift is positive. Higher J states are spread in energy more, so that their low-field shifts lessen as J increases. Eventually, as the field is increased there comes a point where the shift reverses direction and the energy of the state decreases. Thus the effective dipole of the state, given by the slope of the E vs $\mathcal{E}$ curve, actually reverses sign!

This implies that there is a maximal potential energy hill that the guided molecules can climb, one that increases with J, given by the difference between the zero field energy and the energy maximum. Table 5.1 lists this maximum for the lowest three states weak-field seeking states with $m = 0$ and gives the responsible field strength $\mathcal{E}_{turn}$ both for a general molecule and also for the specific case of SrO. For reference, $\mathcal{E}_{turn} = 1\ [B_e/d]$ (with B_e in cm^{-1} and d in Debye) is, in ordinary units, $\mathcal{E}_{turn} =$

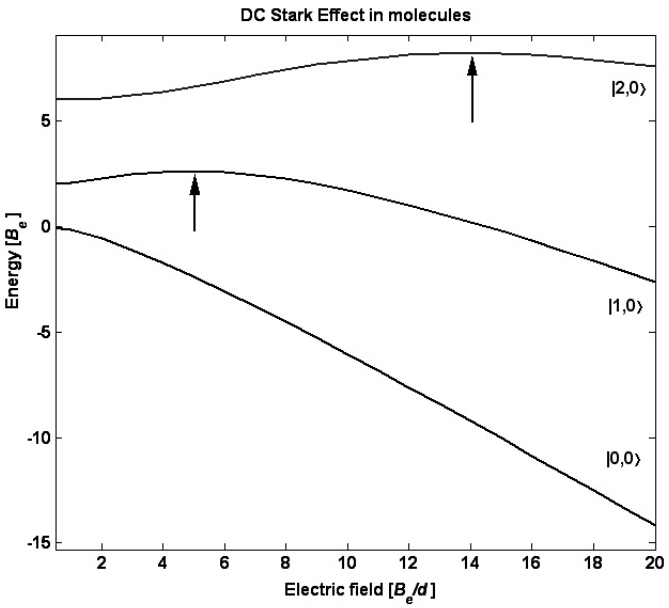

Figure 5.1: DC Stark effect in polar diatomic molecules as a function of electric field strength. States are labeled with their zero-field quantum numbers $|J, m\rangle$. Energy is in units of the molecular rotational constant B_e, and the field is in units of rotational constant B_e over dipole moment d. Arrows indicate the maximum guiding potential for the lowest two m=0 weak-field seekers.

State	$\Delta E_{\rm Max}$ $[B_e]$	$\Delta E_{\rm Max}$ (SrO) [K]	$\mathcal{E}_{\rm turn}$ $[B_e/d]$	$\mathcal{E}_{\rm turn}$ (SrO) [kV/cm]
$\|1,0\rangle$	.639	.304	4.91	11.4
$\|2,0\rangle$	2.22	1.05	13.9	32.2
$\|3,0\rangle$	4.65	2.21	27.0	62.7

Table 5.1: Outline of the maximum Stark shift, $\Delta E_{\rm Max}$, for the first three (zero field labeled) $|J,0\rangle$ weak field seeking states, and the field strength $\mathcal{E}_{\rm turn}$ where it occurs.

59.5 [kV/cm].

5.1.2 Quadrupole field

Field configurations that lead to guiding of the molecules must provide an axis for the molecules to travel along, and forces that bind the molecule along that axis. The simplest fields that provide such a configuration are the multipole electric fields. These fields $\vec{\mathcal{E}}$ are derivable in cylindrical coordinates (r,θ) from the equipotential $\phi(r,\theta)$:

$$\phi(r,\theta) = A\, r^n \cos(n\theta)\,, \tag{5.8}$$

with $n = 2$ for a quadrupole field and constant A which sets the field strength. This field can be constructed from four cylindrical rods that approximate the ideal equipotential near the guide axis. The rods alternate between applied voltage $\pm V$. Reproducing the theoretically exact hyperbolic equipotential is not only unnecessary for fields near the axis, but also difficult to manufacture, and incompatible with maintaining the voltage across rods, since they would nearly touch. The closest approximation using these rods matches the rods' radius of curvature to that of the equipotential at the rod point closest to the guide axis. This gives a geometry that equally spaces the rods one rod radius R away from the axis (see figure 5.2). It follows that the spacing between rods is $(2\sqrt{2}-2)R = .83R$ in this geometry.

For the quadrupole, the field components and magnitude have a linear radial

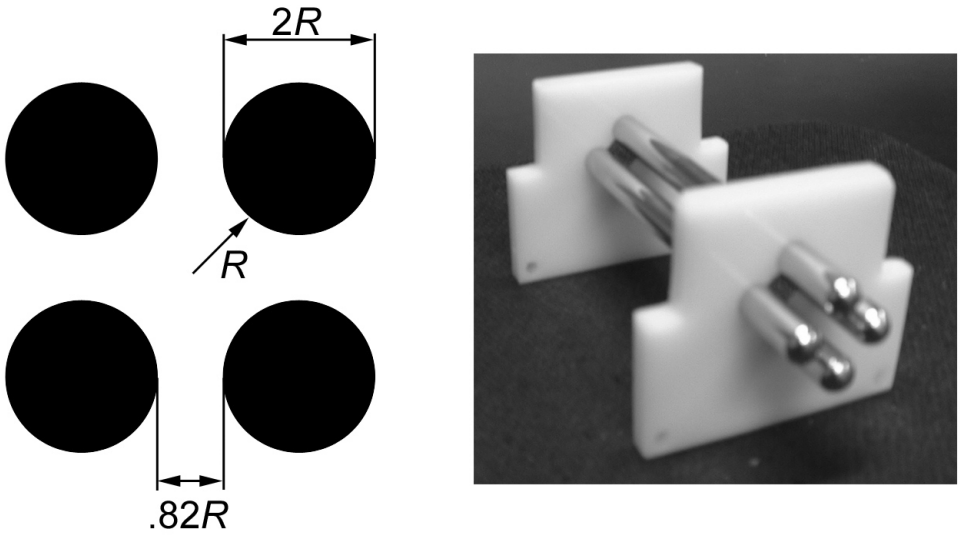

Figure 5.2: Left: general quadrupole guide geometry of radius R. Right: photograph of the constructed and tested guide using 0.25" diameter rods.

dependence:

$$\vec{\mathcal{E}} = -\nabla\phi\,; \tag{5.9}$$

$$\mathcal{E}_r = \frac{2V}{R^2} r\cos 2\theta\,; \tag{5.10}$$

$$\mathcal{E}_\theta = -\frac{2V}{R^2} r\sin 2\theta\,; \tag{5.11}$$

$$|\vec{\mathcal{E}}| = \frac{2V}{R^2} r\,. \tag{5.12}$$

The field strength $|\vec{\mathcal{E}}|$, then, created by the rods depends on their radius and the voltage difference ($2V$). At the rod face nearest the axis it is then approximately $2V/R$.

5.1.3 Molecule energies in a quadrupole field

Visualizing the actual Stark shift leading to guiding of the molecules inside the guide is not difficult, and several levels of sophistication describing this process exist. To zeroth order, the guiding of the molecules arises from the combination of the DC Stark effect with the *magnitude* of the electric field since adiabatic motion of the molecules

through the guide will maintain the projection along the field. On axis there is no electric field, and hence no shift. As the molecule flies away from the axis, the field grows, so the Stark shift causes a force toward the axis (for weak-field seekers). To guide the maximum amount of molecules, the fields near the rods should match or exceed the turning field $\mathcal{E}_{\text{turn}}$. This ensures that any molecules with energy less than ΔE_{Max} in the transverse direction will be guided. Those with energies greater than this will either leave the guide or run into the rods.

The corresponding zeroth order estimate of the transmission of the guides is then simply the probability that entering molecules (from the source distribution) have a transverse energy less than ΔE_{Max}. A fully effusive source has a normalized transverse energy, E_T, given by the distribution function $f(E_T)$ where,

$$f(E_T) = \frac{1}{k_b T} e^{\frac{-E_T}{k_b T}} . \tag{5.13}$$

Since the buffer gas beam source typically showed 4.2 K transverse Doppler temperatures, even for moderately to fully boosted beams, use of this distribution is appropriate for approximating the transmission of the guide. For guiding of the $|1,0\rangle$ state with fields at the rods corresponding to its maximum Stark shift, the transmission of such a guide is 7.3%. For the $|2,0\rangle$ and $|3,0\rangle$ states the transmission is 23% and 42% respectively, although guiding these states requires much higher fields.

Going to the next level of sophistication in a calculation of the guide efficiency requires numerically solving for the actual two dimensional field magnitude (the rods only approximate the quadrupole) and plugging in the DC Stark shift calculation at each point (figure 5.3). No substantial insights are gleaned here; the general guiding mechanism and criterion is the same as before. An even fuller picture requires thought about the full three dimensional field, with simulated loading and guiding. Here intuition becomes more difficult due to the larger parameter space. For example, when molecules enter the guide, they must traverse a fringe field region that affects their

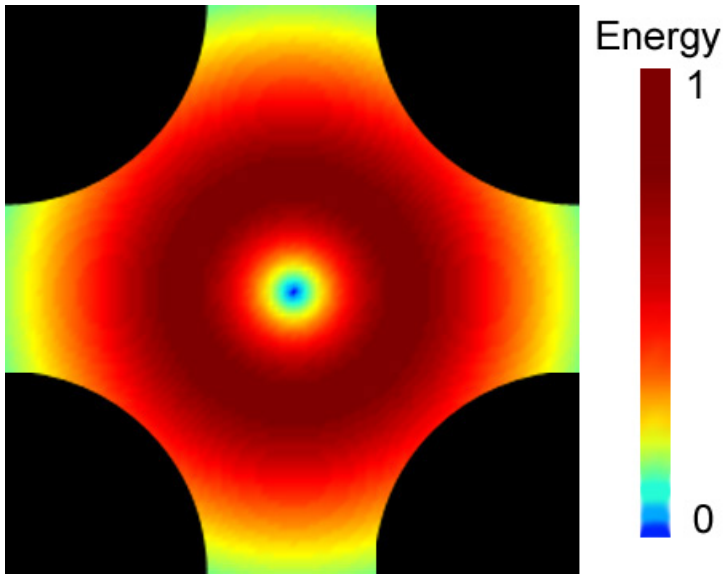

Figure 5.3: DC Stark energies of the $|1,0\rangle$ molecular state in the two dimensional quadrupole electric field. The dark red ring near the guide rods (shown as black circles) corresponds to the shift maximum. Electric field magnitudes continue to increase toward the rods.

motion. Moreover, the entrance point and velocity distribution of these molecules is a function of the molecule beam source parameters. The transmission through the guide may still be approximated by convolving these factors, but optimization of the beam source may not optimize the guide transmission due to effects like collisions with buffer gas inside the guide. A simpler way to maximize transmission through the guide may be to just try and map out the parameter space through measurement.

5.1.4 Guide construction and testing

Construction and testing of such a guide has begun. Currently the preferred design is uses $R = 0.125$" rods. For guiding of the $|1,0\rangle$ state, this corresponds to a 3.6 kV difference between the rods (± 1.8 kV applied). To maintain such a field without initiating an electrical discharge, the rods must be highly polished and high voltage construction protocols must be followed. One possible source of trouble is the large

amount of helium that streams from the buffer gas cell toward the guide because regardless of the level of engineering, sustained electric discharge can occur for large voltage drops, when gas is present.

The relevant information comes in the form of the Paschen curve, which shows that the medium-dependent breakdown voltage is a function of the background gas density times the electrode separation. Figure 5.4 shows the same typical shape that Paschen curves follow. At low densities, or when the electrode separation is very small, not much gas resides between the electrodes so that any ions created have little chance to collide with other background gas and create a sustaining discharge. Thus in this regime the breakdown voltage is large. At large densities, ions created accelerate in the field only small distances before colliding, and will not have accumulated enough kinetic energy to create more ions. And when the separation is large, the accelerating fields are smaller. Thus in this regime the breakdown voltage is large. A minimum in the breakdown voltage exists between these limits. (In)conveniently, this happens to lie somewhere near the conditions at the exit of the buffer gas cell. Further from the cell, higher vacuum conditions exist, so that there should be no breakdown issues there.

Construction of the guide was fairly straightforward. Four thin stainless steel tubes were cut to length. In each end, a stainless steel ball bearing was hard soldered, to cap the tube and round the ends. In a lathe, the rods were smoothed and polished using increasingly fine sandpaper and polishing compound. Spacers of Delrin plastic held the rods in the quadrupole geometry. Copper mounts (to match the thermal contraction of the cell) held the delrin to the cold plate. Electrical connections were made by pressing a copper ferrule onto the rod with a nylon screw. Vacuum-compatible insulated wire (MDC Inc. KAP-1) brought the high voltage to a standard SHV vacuum feedthrough.

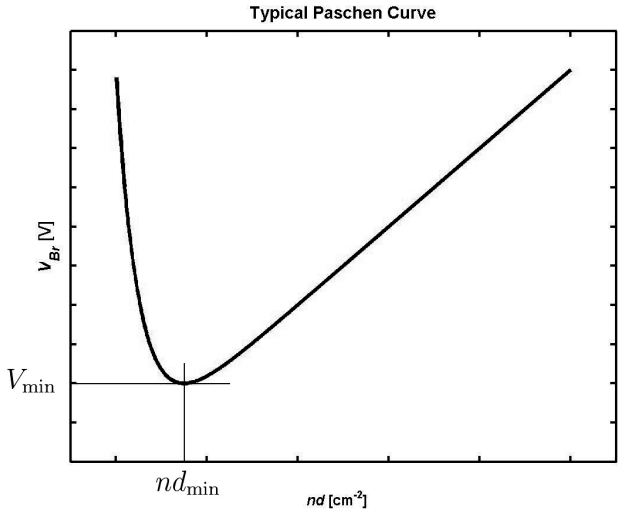

Figure 5.4: Diagram of a typical Paschen curve. The Paschen curve relates the breakdown voltage in a gas V_{Br} as a function of nd, the density n of background gas times the electrode separation distance d. In helium, the Paschen curve minimum of $V_{\min} \simeq 100$ V lies near $nd_{\min} = 2 * 10^{17}$ cm^{-2} [81]. Actual breakdown voltages depend on electrode shape and condition.

Testing of this guide in place showed mixed results. When at cryogenic temperatures, the guide rods could be charged all the way to ±5000 V without discharging. Further, even with the full helium flow required for flux enhancement and boost, the ±5000 V condition produced no discharge. Thus it seemed that a working guide could be made with little trouble. However, the act of ablating the SrO intermittently (every ten ablation shots or so) produced a discharge, tripping the power supplies. Even though it was always confined to the end of the guide nearest the cell, the discharge did not repeatedly occur on the same rod, or at the same point on the rod. Turning down the voltage and the helium density did help the situation. For example, at the lowest flow rates (where an effusive beam would be produced) with ±2000 V applied to the rods, discharge rarely, if ever, occurred.

Still, it is desirable to eliminate this discharge altogether, in order to have a trouble free system. Thus its cause and possible solutions were investigated. The observation

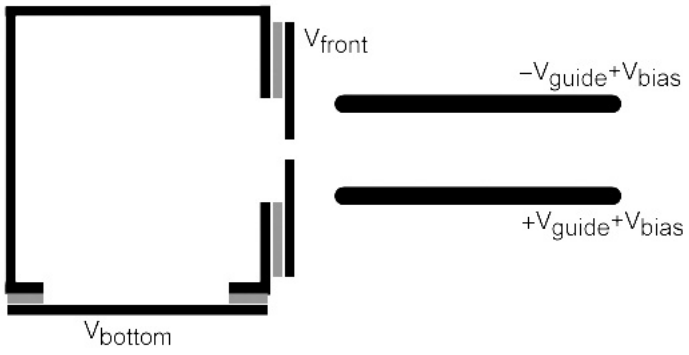

Figure 5.5: Diagram of the cell and (foreground) guides showing the manner in which ion filtering voltages were applied. The front and bottom faces were electrically isolated (grey layer) from the grounded cell. Independently applying voltages up to ±60 V in different combinations to the two faces had either no effect, or a detrimental effect on the discharge. Applying a negative bias to the rods was the only configuration that reduced the probability of discharge.

of a discharge was always correlated with the ablation pulse. As such, a plausible explanation for its cause is that ions are created directly in the ablation process, and these also make their way into the molecular beam. Since the cell was electrically grounded it was easy to apply an overall bias to the guides (±2000 V + bias) to see if these ions could be repelled, and the discharge stopped. In fact, we found that for moderately sized (negative) biases up to -500 V this was the case: helium flow could be somewhat increased before discharge occurred regularly. Application of positive bias voltages had no discernable effect. This suggests that the ions are negatively charged, and are in fact probably electrons, which would be accelerated easily by the high voltage rods. Applying voltages to the cell faces (see figure 5.5) was also attempted to filter out these charged particles, but this met with little success.

Of course this description of the guide breakdown is rather qualitative. It is such because of the intermittent nature of the breakdown. Fresh ablation spots for example

(with their higher molecule yield), also produced the most frequent discharge. Moving the ablation point within the cell, even when large helium flows produced roughly constant yield, also had an effect on the probability of a discharge. The current state of thinking is that the guides should reliably work at ±2000 V, with the lowest flow rates (effusive source) just fine. However if the guides wish to be used for the fully entrained, boosted beam, more ideas need to be tried to prevent the discharge. Some of these ideas are other in-cell voltage (ion filter) geometries, and gating the high voltage off during the ablation, or moving the guides further away from the buffer gas cell.

5.2 Molecule trapping

After the guiding stage separates the molecules from the helium, trapping of the molecules will allow for further cooling below 4.2 K. As discussed, current molecule traps rely on static fields and they suffer from a serious drawback, that of trap loss due to relaxation or inelastic collisions. The key point is that static fields cannot support a free space field maximum, so these traps all are field minimum, weak field seeking based. Weak field seeking energy states, in cases of interest, are not the ground state of the system. Thus inelastic collisions can cause relaxation to the ground (strong field seeking) state. Collisional losses can thus preclude the building up of phase space density as the gas is cooled. Although these were overcome in atomic systems, it is predicted that the loss mechanisms in molecular traps will be much greater [24].

To overcome these difficulties/drawbacks, our route to production of ultracold molecules involves development of a strong field seeking trap [82]. Similar in many respects to the optical dipole trap, this trap utilizes strong, inherently AC fields to produce a field maximum. Trapping of the ground state of the system thus energetically forbids state changing processes, removing the possibility of inelastic collisions.

The particular trap under development is a microwave trap, nearly resonant with the first molecular rotational transition, realized as a standing wave antinode in a power building, microwave resonant, cavity. Molecules are held in the trap via the AC Stark shift arising between the rotational states of the molecule. The trap relies on the large polarizability of molecules with reasonable dipole moments to produce very large trap depths (>1 K), allowing it to be used with a variety of sources, including the buffer gas-cooled molecular beam. Also, given that the microwave wavelengths are long ($\lambda \sim 1$ cm) the trapping volumes ($\lambda^3 \sim 1$ cm^3) will be large, allowing for easy loading of the available low phase space density sources.

5.3 AC Stark effect

Similarly to the calculation of the DC Stark effect described earlier, the AC Stark effect calculation allows us to map the potential of the molecules inside the microwave fields. Operating with frequencies near the $J = 0 \leftrightarrow 1$ resonance allows for efficient mixing (polarization) of these states at even low fields. Typical optical dipole traps operate much farther from resonance due to the large (optical) scattering rates. Here however, scattering is not a concern because of the cubic frequency dependence of the scattering rates [83] and the many orders of magnitude lower frequency of microwaves versus optical fields.

As in the DC Stark case, we will restrict ourselves to the calculation for rigid rotor $^1\Sigma$ molecular states. Again, the interactions are the field-dipole Stark interactions. To recap, the field free rotational Hamiltonian H_0 and Stark Hamiltonian H_{St} are

$$H_0 = B_e J(J+1)\,, \tag{5.14}$$

$$H_{St} = -\vec{d}\cdot\vec{\mathcal{E}}\,. \tag{5.15}$$

To calculate the AC Stark effect for a general microwave field of strength $\mathcal{E}_0$, frequency

ω, and polarization ϵ,

$$\vec{\mathcal{E}}(t) = Re\{\vec{\mathcal{E}}_0 e^{i\omega t}\} = \mathcal{E}_0 Re\{\vec{\epsilon} e^{i\omega t}\}\,, \tag{5.16}$$

we use the dressed state formalism of reference [84]. In this formalism the field is quantized using the photon creation and annihilation operators, $a^\dagger$ and a. The field energy H_0' is defined as the energy carried by the number of photons in the field $\hat{N}$:

$$\hat{N} = a^\dagger a\,, \tag{5.17}$$

$$H_0' = \hbar\omega(\hat{N} - \bar{N})\,, \tag{5.18}$$

with the zero of energy chosen at the mean photon number $\bar{N}$. For even low microwave powers, the photon number is large so $\bar{N} \gg 1$ for the entire calculation. The quantized version of the Stark Hamiltonian becomes

$$H_{St}' = -\vec{d}\cdot\vec{\mathcal{E}} \tag{5.19}$$

$$= -d\sqrt{\frac{\hbar\omega}{2\epsilon_0 V}}\{(\vec{n}\cdot\vec{\epsilon}^*)a^\dagger + (\vec{n}\cdot\vec{\epsilon})a\} \tag{5.20}$$

where $\vec{n}$ is molecular axis of symmetry and V is the volume of the fictitious box used to define the size of the electric field. Using the field strength definition,

$$\bar{N} = \frac{\mathcal{E}_0^2}{2}\frac{\epsilon_0 V}{\hbar\omega} \tag{5.21}$$

all physically meaningful quantities are independent of V.

To find the energy shift ΔE of any state due to the AC Stark effect we must diagonalize the full molecule plus field plus interaction Hamiltonian. For this energy shift calculation we simplify the calculation somewhat by discarding the molecule and field phase information through use of a large $\bar{N}$ Fock state for the field (the microwaves are actually a coherent state). The full states are then the zero field molecule basis – Fock state product, $|\psi_{J,m,n}\rangle \equiv |J,m\rangle|\bar{N}+n\rangle$, where J and m are the

familiar molecular rotational quantum numbers (with angular wavefunctions $|J,m\rangle = Y_J^m(\theta,\phi)$), and $n+\bar{N}$ is the photon number in the field. From the form of the Stark effect, it is clear that this combination of dipole (vector) and photon operators mixes states only where $J' = J \pm 1$ and $n' = n \pm 1$. Thus the relevant matrix elements are,

$$\begin{aligned}\langle\psi_{J,m,n}|H_0 + H_0' + H_{St}'|\psi_{J',m',n'}\rangle &= [B_e J(J+1) + \hbar\omega n]\,\delta_{J\,J'}\delta_{m\,m'}\delta_{n\,n'} \\ &\quad + \frac{d\mathcal{E}}{2}\langle J',m'|\vec{n}\cdot\vec{\epsilon}|J,m\rangle\delta_{n',n-1} \\ &\quad + \frac{d\mathcal{E}}{2}\langle J',m'|\vec{n}\cdot\vec{\epsilon}^*|J,m\rangle\delta_{n',n+1} \qquad (5.22)\end{aligned}$$

The result of the diagonalization most interesting to the problem of AC field trapping of molecules is the energy shift ΔE in the zero-field state labeled $|\psi_{0,0,0}\rangle$. Diagonalization at various field strengths allows for following of the molecular energy at different points in the trapping region. As in the DC case, the infinitely connected subspace will be truncated in order to perform the numerical diagonalization calculation. To ensure that the calculation has converged, the adjacent $|\psi_{J,m,n}\rangle$ and $|\psi_{J,m,n\pm2}\rangle$ states are compared. Also, the effect of increasing the calculational subspace was examined.

5.4 Linear polarization

When calculating the AC Stark effect, two distinct cases emerge: one using linearly polarized trapping fields and another using circularly polarized trapping fields. Somewhat surprisingly, the energy shift results using these two different polarizations differ drastically. We begin with the linearly polarized case, where the electric field is polarized along z ($\vec{\epsilon} = \hat{z}$). The subspace of levels connected to the molecular ground state $|\psi_{0,0,0}\rangle$ is shown in figure 5.6. Note that the full subspace contains several levels with the same molecular quantum numbers (J and m), but varying cavity photon number. Arrows pointing up and to the left represent the traditional absorption process,

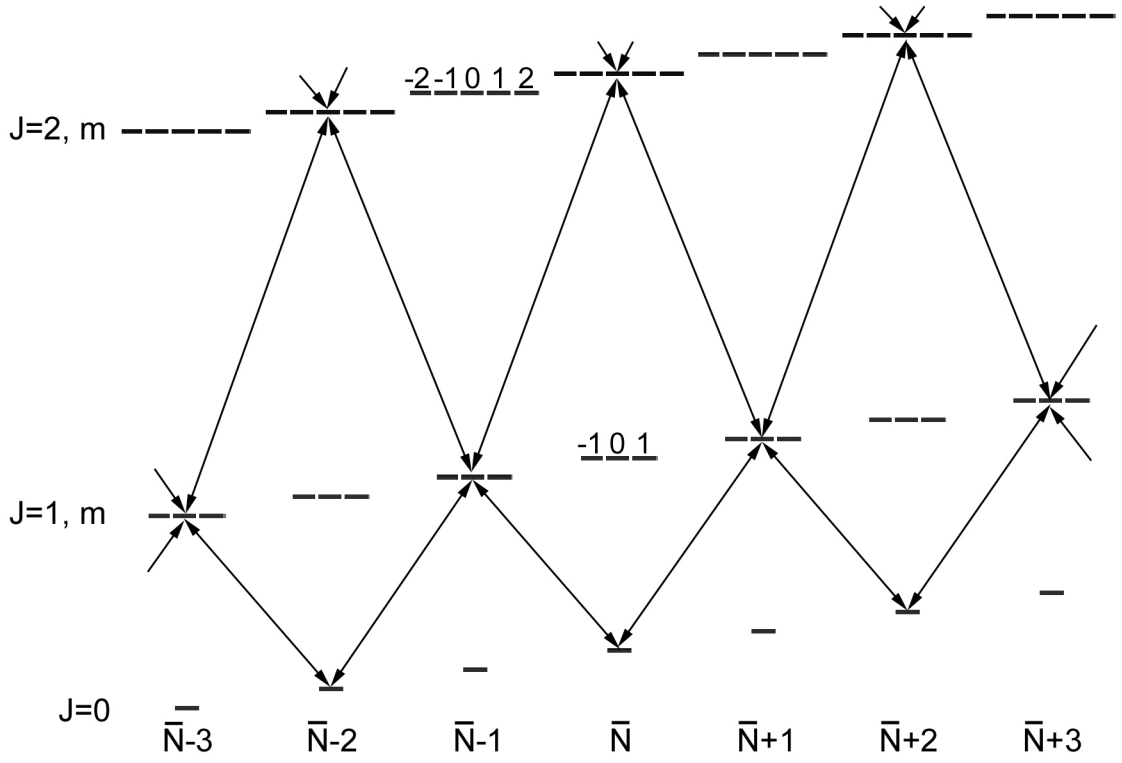

Figure 5.6: Dressed-state energy level diagrams for rotational states of a diatomic molecule subject to a linear microwave electric field. The indices at the bottom indicate the photon number $\bar{N}+n$, where $\bar{N}$ is the average number of photons in the field; the labels J, m at the side indicate the rotational angular momentum and its z-projection, respectively. Arrows indicate 1st-order couplings between levels due to H'_{St}; unterminated arrows couple to levels outside the range of the figure. The subset of the Hilbert space used for the calculations described in the main text consists of only levels connected to $|\psi_{0,0,0}\rangle$ with some number of arrows.

those to pointing down and to the right emission. The remaining arrows (pointing up and right, and down and left) correspond to the matrix elements that are usually discarded in the rotating wave approximation. It is important that these matrix elements are kept, however, as they allow multi-photon resonances with the connected subspace to be calculated.

The analytical form of the molecular matrix elements is given by

$$\begin{aligned}\langle J,m|\vec{n}\cdot\epsilon|J',m'\rangle &= \langle J',m'|\vec{n}\cdot\epsilon^*|J,m\rangle \\ &= \langle J',m'|\cos\theta|J,m\rangle \\ &= \int Y_{J'}^{m'*}\cos\theta Y_J^m d\Omega \\ = \left[\frac{J}{\sqrt{2J-1}\sqrt{2J+1}}\delta_{J',J-1} + \frac{J}{\sqrt{2J+1}\sqrt{2J+3}}\delta_{J',J+1}\right]\delta_{m',m}\,. \end{aligned} \tag{5.23}$$

Keeping a rather large subspace, with states up to $J_{\max} = 5$ and $n_{\max} = 20$, the convergence-tested energy of the dressed states is shown in figures 5.7 and 5.8. Since this subspace contains so many states, only a single state with (zero field) J value is shown in figure 5.8, in order to show the salient features of the system. First note that the state $|\psi_{0,0,0}\rangle$ state repels from the $|\psi_{1,0,-1}\rangle$ state at low field. For the calculation at low frequency (not shown) and field ($\hbar\omega \ll B_e$ and $\mathcal{E}_0 \ll B_e$), the quadratic energy shift reproduces the DC calculation when the RMS field strength matches that of the DC case, as expected. For the (near resonant) calculation shown, the DC and AC cases differ strikingly. Here, strongly avoided crossings with other states destroys the monotonic decrease of the $|\psi_{0,0,0}\rangle$ state.

These avoided crossings can be seen roughly as multi-photon resonances between molecular states. For example, the first large avoided crossing between the states labeled $|\psi_{0,0,0}\rangle$ and $|\psi_{2,0,-6}\rangle$ can be thought of as a six-photon process that the strong fields shift into resonance. However, since the full field eigenstates of the diagonalized Hamiltonian are not the same as the zero field labels, this is only an analogy, and not an exact correspondence. Avoided crossings occur with all levels in the subspace, so that every apparent crossing in figure 5.8 is actually avoided. The strength of the avoided crossing depends on the strength of coupling between the field-mixed states. Since the levels become mixed quickly and the coupling is a high order process, it is difficult to predict the energy difference of the anti-crossing.

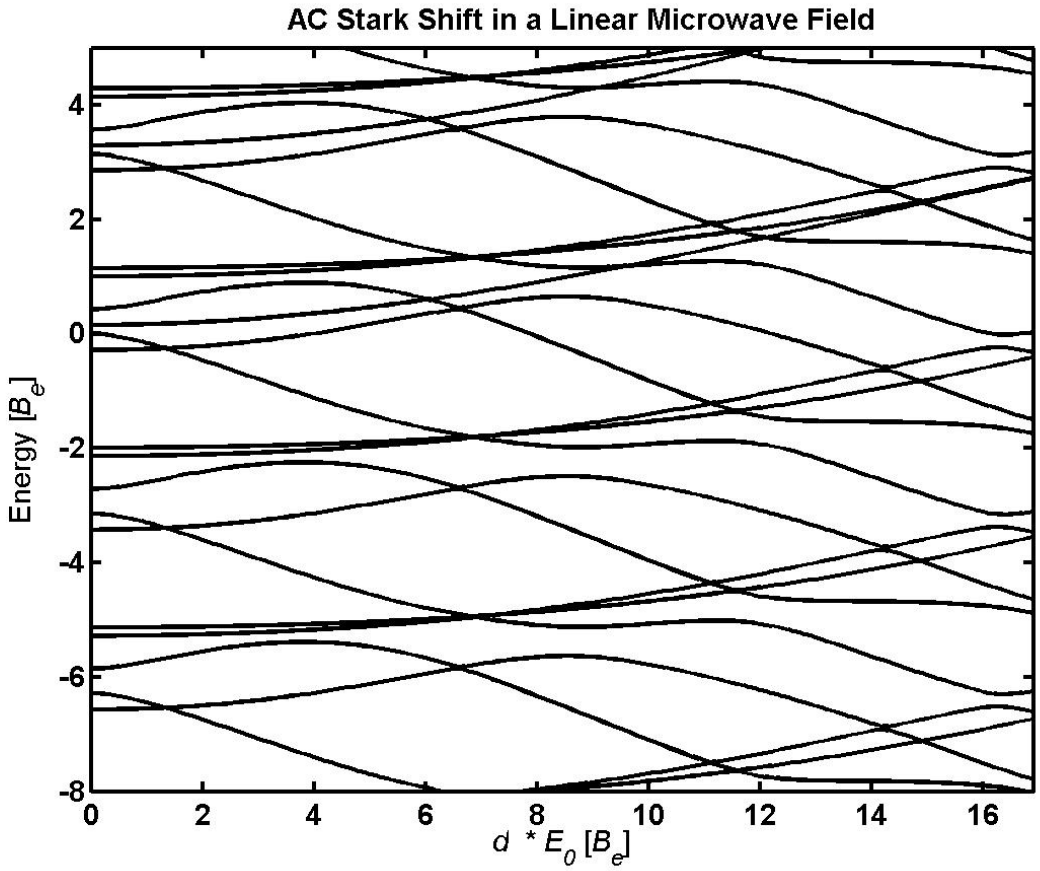

Figure 5.7: Energies of dressed states vs. applied microwave electric field strength for linear polarization ($\vec{\epsilon} = \hat{z}$), with the full calculational subspace connected to $|\psi_{000}\rangle$ shown. State labels are zero-field basis states $|\psi_{J,m,n}\rangle$. For this figure we have chosen a typical working value of the microwave frequency, $\omega = 1.57B_e$. In this calculation the subspace includes states up to $J_{max} = 5$ and $n_{max} = 20$. Note how the pattern of levels is repeated for states with photon number $n' = n \pm 2k$, where k is any integer.

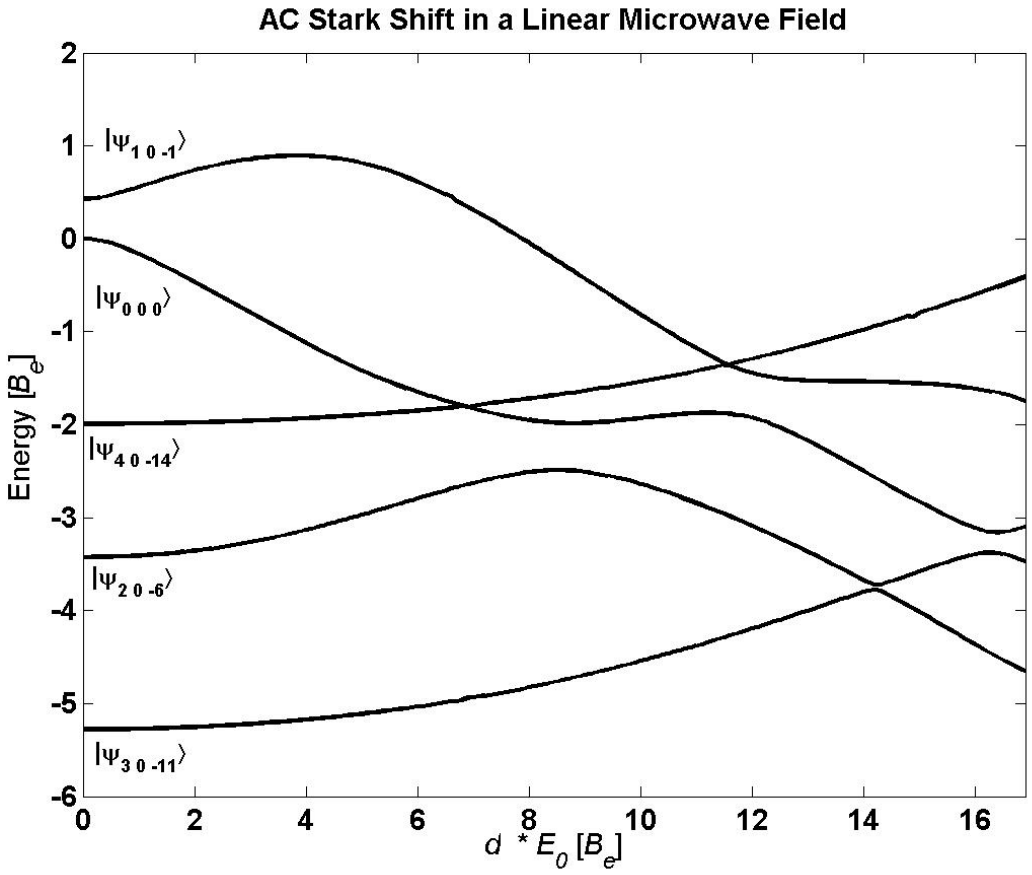

Figure 5.8: Energies of dressed states vs. applied microwave electric field strength for linear polarization ($\vec{\epsilon} = \hat{z}$), partial subspace. State labels are zero-field basis states $|\psi_{J,m,n}\rangle$. Only the subspace connected to $|\psi_{0,0,0}\rangle$ is shown. For this figure we have chosen a typical working value of the microwave frequency, $\omega = 1.57B_e$. In this calculation the subspace includes states up to $J_{max} = 5$ and $n_{max} = 20$. For clarity, only one dressed state for each initial value of $J < J_{max}$ is shown in the diagram. Note the large avoided crossings with the state that originates as $|\psi_{000}\rangle$ at zero field; the crossing of $|\psi_{0,0,0}\rangle$ and $|\psi_{4,0,-14}\rangle$ is also avoided, but the separation is too small to see in this diagram.

These anti-crossings are highly undesirable, as the molecular motion through the trap will cause it to experience varying fields. As the molecule samples the varying field, the anti-crossings will cause trouble if the energy gap of the avoided crossing Δ is larger than the effect of the field change $\Delta \sim \frac{1}{E}\frac{\partial E}{\partial t}$. Then the "motion" of the molecular state will be adiabatic, and the avoided crossing will be followed instead of hopping through the crossing. From the simple multi-photon resonance picture, this corresponds to adiabatically absorbing the multiple photons needed to excite to the molecular state with which the crossing occurs. Of course, states other than $|\psi_{0,0,0}\rangle$ have smaller trap depths, and in any case, transfer of molecules to the other anti-crossed levels is unsuitable for trapping.

5.5 Circular polarization

A completely different picture emerges for the case of using circular polarization $\vec{\epsilon} = (\hat{x} - i\hat{y})/\sqrt{2}$ for the microwave trapping fields. Here, due to conservation of angular momentum, the "subspace selection rule" for states connected to $|\psi_{0,0,0}\rangle$ entails that the molecular projection m is the same as the change in photon number n. In contrast to the simple resonance picture used in the linear case, coupling can now only occur to states $|\psi_{J',m'=\pm J',n'=m'}\rangle$ (see figure 5.9). For frequencies less than the $J = 0 \rightarrow J' = 1$ transition frequency, there are no connected subspace levels that will have lower energy than $|\psi_{0,0,0}\rangle$. In addition, this precludes any levels being resonant with $|\psi_{0,0,0}\rangle$, at any photon number level.

The calculation and checking of the circular polarization energy level diagram is

the same as for the linear case. Here, the off diagonal matrix elements are

$$\begin{aligned}\langle J,m|\vec{n}\cdot\epsilon|J',m'\rangle &= \langle J',m'|\vec{n}\cdot\epsilon^*|J,m\rangle \\ &= \frac{1}{\sqrt{2}}\langle J',m'|\sin\theta\, e^{i\phi}|J,m\rangle \\ &= \frac{1}{\sqrt{2}}\int Y_{J'}^{m'*}\,\sin\theta\, e^{i\phi}\, Y_J^m\, d\Omega \\ = \left[\frac{\sqrt{J-m-1}\sqrt{J-m}}{\sqrt{2J-1}\sqrt{2J+1}}\delta_{J',J-1} + \frac{\sqrt{J+m+1}\sqrt{J+m+2}}{\sqrt{2J+1}\sqrt{2J+3}}\delta_{J',J+1}\right]&\delta_{m',m+1} \quad (5.24)\end{aligned}$$

and the matrix for a subspace containing $J_{max} = 2$ states is simple enough to be shown as,

$$H_0 + H_0' + H_{St}' = \begin{array}{c} \begin{array}{cccccc} |\psi_{0,0,0}\rangle & |\psi_{1,1,1}\rangle & |\psi_{1,-1,-1}\rangle & |\psi_{2,2,2}\rangle & |\psi_{2,0,0}\rangle & |\psi_{2,-2,-2}\rangle \end{array} \\ \begin{pmatrix} 0 & \frac{d\mathcal{E}}{\sqrt{6}} & \frac{d\mathcal{E}}{\sqrt{6}} & 0 & 0 & 0 \\ \frac{d\mathcal{E}}{\sqrt{6}} & 2B_e-\hbar\omega & 0 & \frac{d\mathcal{E}}{\sqrt{5}} & \frac{d\mathcal{E}}{\sqrt{30}} & 0 \\ \frac{d\mathcal{E}}{\sqrt{6}} & 0 & 2B_e+\hbar\omega & 0 & \frac{d\mathcal{E}}{\sqrt{30}} & \frac{d\mathcal{E}}{\sqrt{5}} \\ 0 & \frac{d\mathcal{E}}{\sqrt{5}} & 0 & 6B_e-6\hbar\omega & 0 & 0 \\ 0 & \frac{d\mathcal{E}}{\sqrt{30}} & \frac{d\mathcal{E}}{\sqrt{30}} & 0 & 6B_e & 0 \\ 0 & 0 & \frac{d\mathcal{E}}{\sqrt{5}} & 0 & 0 & 6B_e-6\hbar\omega \end{pmatrix} \end{array}.$$

With no states lower in energy than $|\psi_{0,0,0}\rangle$, its energy as a function of field (figure 5.10) simplifies greatly. In fact, the behavior is remarkably similar to that of the DC case, as was originally expected for the linear polarization case. For low frequencies and fields, the behavior again replicates the DC case. For large fields the molecule fully polarizes and a linear Stark shift of $\Delta E \approx -d\mathcal{E}_0/2$ results; the transition from quadratic to linear shifts occurs at smaller field strengths as the frequency detuning is decreased.

5.6 Microwave trap design

Since the ultimate goal is trapping and further cooling of the molecules produced in the buffer gas-cooled beam, very large Stark shifts, minimally on the order of the beam temperature, will be required to contain any substantial fraction of the beam

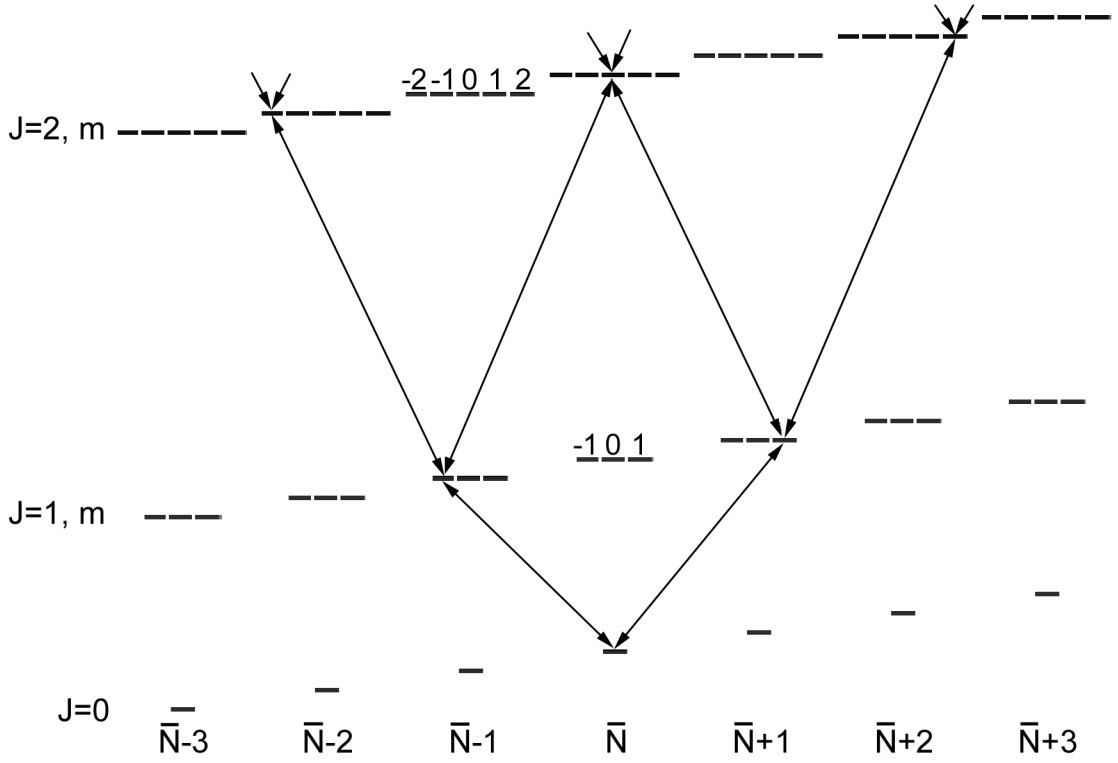

Figure 5.9: Dressed-state energy level diagrams for rotational states of a diatomic molecule subject to a circular microwave electric field. The indices at the bottom indicate the photon number $\bar{N}+n$, where $\bar{N}$ is the average number of photons in the field; the labels J, m at the side indicate the rotational angular momentum and its z-projection, respectively. Arrows indicate 1st-order couplings between levels due to H'_{St}; unterminated arrows couple to levels outside the range of the figure. The subset of the Hilbert space used for the calculations described in the main text consists of only levels connected to $|\psi_{0,0,0}\rangle$ with some number of arrows. For clarity, we have chosen $\hbar\omega = 0.2B_e$ for this figure.

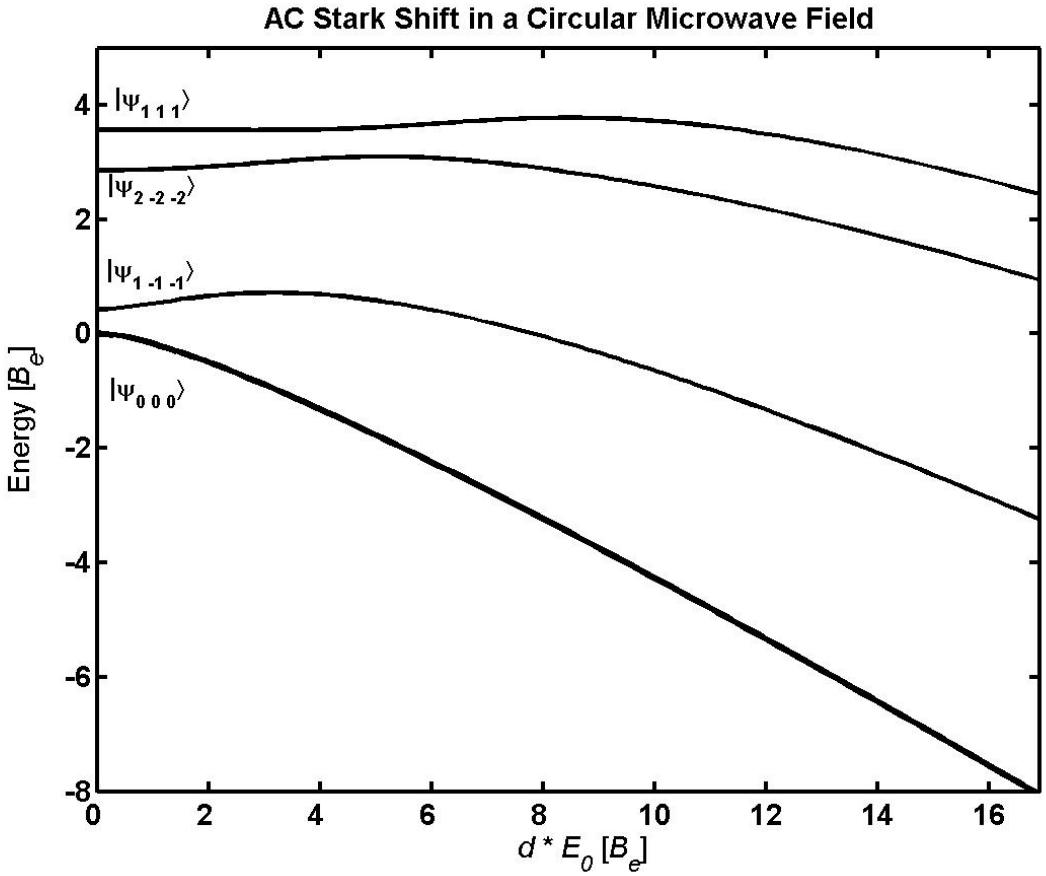

Figure 5.10: Energies of dressed states vs. applied microwave electric field strength for circular polarization ($\vec{\epsilon} = \frac{1}{\sqrt{2}}\hat{x} - i\hat{y}$). State labels are zero-field basis states $|\psi_{J,m,n}\rangle$. Only the subspace connected to $|\psi_{0,0,0}\rangle$ is shown. For this figure we have chosen a typical working value of the microwave frequency, $\omega = 1.57B_e$. In this calculation the subspace includes states up to $J_{max} = 10$ and $n_{max} = 10$. All states of the coupled subspace in the plotted energy region are shown. Note the monotonic behavior and lack of avoided crossings for the $|\psi_{0,0,0}\rangle$ state.

in the microwave fields. For large Stark shifts ($\Delta E > B_e$) in the microwave fields figure 5.10 shows that the shift scales with field like

$$\Delta E = \frac{d\mathcal{E}_0}{2} \tag{5.25}$$

$$\simeq 1.2 \times 10^{-5}\,[\mathrm{K}] \times d\,[\mathrm{Debye}] \times \mathcal{E}_0\,[\mathrm{V/cm}] \tag{5.26}$$

For a desired SrO trap depth of $\Delta E = 4$ K, this requires an extremely large field of $\mathcal{E}_0 = 3.7 \times 10^4$ V/cm.

The open geometry of traditional optical dipole traps is particularly appealing particularly for loading the trap with the molecules and having room for optical access to the trapping region. Setting up the trap by simply focussing a Gaussian beam of wavelength λ and power P to its minimum waist $w \sim \lambda$ [85] yields an on-axis field $\mathcal{E}_0$ at the focus of

$$\mathcal{E}_0\,[\mathrm{V/cm}] \sim \sqrt{\frac{1000P\,[\mathrm{W}]}{2(\lambda\,[\mathrm{cm}])^2}}\,. \tag{5.27}$$

For the required SrO field strengths and frequencies ($\frac{\omega}{2\pi} = 20$ GHz, $\lambda = 1.5$ cm), the power required is $P = 6.5 \times 10^6$ W. Fortunately, substantial power (up to 2 kW) is available for the required SrO trapping frequencies; unfortunately, this is substantially less than the required field for a 4 K trap depth. Using a cavity could solve this problem, by building up the recirculating power. Although the 3250× (power) enhancement required is slightly out of reach of a simple room temperature confocal cavity [82] with the parameters above, we currently have a test cavity that we believe could give reasonable trap depths of $\Delta E \simeq 2$ K.

5.7 Future directions

Currently the experiment is undergoing modifications to allow for better optical detection away from the cell aperture. With this enhancement, it should be possible to definitively answer open questions about the beam flux (hydrodynamic enhancement)

and divergence. From here the experiment faces the question on whether to slow the forward motion of the molecules using a buffer-gas type or decelerator type technique. Once these questions are answered, it should be fairly straightforward to reinsert the guides into the apparatus, and couple the buffer-gas forward-slowed beam into the trapping region, or the boosted beam into a decelerator. Only then will it be possible to employ the microwave to proceed with further cooling.

Bibliography

[1] A.L. Schawlow and C.H. Townes, Infrared and optical masers. Physical Review **112(6)**, 1940 (1958).

[2] T.W. Hänsch and A.L. Schawlow, Cooling of gasses by laser radiation. Optics Communications **13(1)**, 68 (1975).

[3] S. Chu, L. Hollberg, J.E. Bjorkholm, A. Cable, and A. Ashkin, Three-dimensional viscous confinement and cooling of atoms by resonance radiation pressure. Physical Review Letters **55(1)**, 48 (1985).

[4] E.L. Raab, M. Prentiss, A. Cable, S. Chu, and D.E. Pritchard, Trapping of neutral sodium atoms with radiation pressure. Physical Review Letters **59(23)**, 2631 (1987).

[5] Erik W. Streed, Ananth P. Chikkatur, Todd L. Gustavson, Micah Boyd, Yoshio Torii, Dominik Schneble, Gretchen K. Campbell, David E. Pritchard, and Wolfgang Ketterle, Large atom number Bose-Einstein condensate machines. Review of Scientific Instruments **77**, 023106 (2006).

[6] M.H. Anderson, J.R. Ensher, M.R. Matthews, C.E. Wieman, and E.A. Cornell, Observation of bose-einstein condensation in a dilute atomic vapor. Science **269**, 198 (1995).

[7] K.B. Davis, M.O. Mewes, M.R. Andrews, N.J. van Druten, D.S. Durfee, D.M. Kurn, and W. Ketterle, Bose-einstein condensation in a gas of sodium atoms. Physical Review Letters **75(22)**, 3969 (1995).

[8] Markus Greiner, Olaf Mandel, Tilman Esslinger, Theodor W. Hänsch, and Immanuel Bloch, Quantum phase transition from a superfluid to a Mott insulator in a gas of ultracold atoms. Nature **415**, 39 (2002).

[9] M.R. Andrews, C.G. Townsend, H.J. Miesner, D.S. Durfee, D.M. Kurn, and W. Ketterle, Observation of interference between two bose condensates. Science **275**, 637 (1997).

[10] J. M. McGuirk, G. T. Foster, J. B. Fixler, M. J. Snadden, and M. A. Kasevich, Sensitive absolute-gravity gradiometry using atom interferometry. Physical Review A **65**, 033608 (2002).

[11] I. K. Kominis, T. W. Kornack, and J. C. Allred anb M. V. Romalis, A subfemtotesla multichannel atomic magnetometer. Nature **422**, 596 (2003).

[12] Kurt Gibble and Steven Chu, Laser-Cooled Cs Frequency Standard and a Measurement of the Frequency Shift due to Ultracold Collisions. Physical Review Letters **70**, 1771 (1993).

[13] B. C. Regan, Eugene D. Commins, Christian J. Schmidt, and David DeMille, New Limit on the Electron Electric Dipole Moment. Physical Review Letters **88**, 071805 (2002).

[14] J. J. Hudson, B. E. Sauer, M. R. Tarbutt, and E. A. Hinds, Measurement of the Electron Electric Dipole Moment Using YbF Molecules. Physical Review Letters **89**, 023003 (2002).

[15] I.B. Khriplovich and S.K. Lamoreaux, *CP Violation Without Strangeness* (Springer, Berlin, 1997).

[16] M. Pospelov and I. B. Khriplovich, . Soviet Journal of Nuclear Physics **53**, 638 (1991).

[17] Eugene D. Commins, in *Advances in Atomic, Molecular, and Optical Physics, Volume 40*, edited by Benjamin Bederson and Herbert Walther (Academic Press, San Diego, 1999), Chap. Electric Dipole Moments of Leptons, p. 1.

[18] Eugene D. Commins, J. David Jackson, and David P. DeMille, The electric dipole moment of the electron: An intuitive explanation for the evasion of Schiffs theorem. American Journal of Physics **75**, 532 (2007).

[19] M G Kozlov and L N Labzowsky, Parity violation effects in diatomics. Journal of Physics B **28**, 1333 (1995).

[20] C. S. Wu, E. Ambler, R. W. Hayward, D. D. Hoppes, and R. P. Hudson, Experimental Test of Parity Conservation in Beta Decay. Physical Review **105**, 1413 (1957).

[21] C. S. Wood, S. C. Bennett, D. Cho, B. P. Masterson, J. L. Roberts, C. E. Tanner, and C. E. Wieman, Measurement of Parity Nonconservation and an Anapole Moment in Cesium. Science **275**, 1759 (1997).

[22] A.V. Titov, N.S. Mosyagin, A.N. Petrov, T.A. Isaev, and D. DeMille, Study of P,T-Parity Violation Effects in Polar Heavy-Atom Molecules. arXiv:physics/0506038v1 (2005).

[23] Gerhard Herzberg, *Molecular Spectra and Molecular Structure* (Van Nostrand Reinhold Company, New York, 1950).

[24] John L. Bohn, Inelastic collisions of ultracold polar molecules. Physical Review A **63**, 052714 (2001).

[25] D. S. Petrov, M. A. Baranov, and G. V. Shlyapnikov, Superfluid transition in quasi-two-dimensional Fermi gases. Physical Review A **67**, 031601 (2003).

[26] M. A. Baranov, M. S. Mar'enko, Val. S. Rychkov, and G. V. Shlyapnikov, Superfluid pairing in a polarized dipolar Fermi gas. Physical Review A **66**, 013606 (2002).

[27] K. Góral, L. Santos, and M. Lewenstein, Quantum Phases of Dipolar Bosons in Optical Lattices. Physical Review Letters **88**, 170406 (2002).

[28] L. E. Sadler, J. M. Higbie, S. R. Leslie, M. Vengalattore, and D. M. Stamper-Kurn, Spontaneous symmetry breaking in a quenched ferromagnetic spinor Bose condensate. Nature **443**, 312 (2006).

[29] E Bodo, F A Gianturco, N Balakrishnan, and A Dalgarno, Chemical reactions in the limit of zero kinetic energy: virtual states and Ramsauer minima in F + H2 → HF + H. Journal of Physics B **37**, 3741 (2002).

[30] A. V. Avdeenkov, D. C. E. Bortolotti, and J. L. Bohn, Field-linked states of ultracold polar molecules. Physical Review A **69**, 012710 (2004).

[31] K. A. Brickman, P. C. Haljan, P. J. Lee, M. Acton, L. Deslauriers, and C. Monroe, Implementation of Grovers quantum search algorithm in a scalable system. Physical Review A **72**, 050306 (2005).

[32] Peter W. Shor, Polynomial-Time Algorithms for Prime Factorization and Discrete Logarithms on a Quantum Computer. arXiv:quant (1996).

[33] Hoi-Kwong Lo and Norbert Lütkenhaus, Quantum Cryptography: from Theory to Practice. arXiv:quant-ph/0702202v3 (2007).

[34] See http://qist.lanl.gov/qcomp_map.shtml for a roadmap to quantum computation.

[35] D. DeMille, Quantum computation with trapped polar molecules. Physical Review Letters **88(6)**, 067901 (2002).

[36] P. Rabl, D. DeMille, J. M. Doyle, M. D. Lukin, R. J. Schoelkopf, and P. Zoller, Hybrid Quantum Processors: Molecular Ensembles as Quantum Memory for Solid State Circuits. Physical Review Letters **97**, 033003 (2006).

[37] A. Andre, D. DeMille, J. M. Doyle, M. D. Lukin, S. E. Maxwell, P. Rabl, R. J. Schoelkopf, and P. Zoller, A coherent all-electrical interface between polar molecules and mesoscopic superconducting resonators. Nature Physics **2**, 642 (2006).

[38] B. Dubetsky and M. A. Kasevich, Atom interferometer as a selective sensor of rotation or gravity. Physical Review A **74**, 023615 (2006).

[39] Shengwang Du, Matthew B. Squires, Yutaka Imai, Leslie Czaia, R. A. Saravanan, Victor Bright, Jakob Reichel, T. W. Hnsch, and Dana Z. Anderson, Atom-chip Bose-Einstein condensation in a portable vacuum cell. Physical Review A **70**, 053606 (2004).

[40] O. Dutta, M. Jääskeläinen, and P. Meystre, Polarizing beam splitter for dipolar molecules. Physical Review A **71**, 051601 (2005).

[41] J. Doyle, B. Friedrich, R.V. Krems, and F. Masnou-Seeuws, Quo vadis, cold molecules?. The European Physical Journal D **31**, 149 (2004).

[42] M.D. Di Rosa, Laser-cooling molecules. The European Physical Journal D **31**, 395 (2004).

[43] Andrew J. Kerman, Jeremy M. Sage, Sunil Sainis, Thomas Bergeman, and David DeMille, Production and State-Selective Detection of Ultracold RbCs Molecules. Physical Review Letters **92**, 153001 (2004).

[44] Cindy A. Regal, Christopher Ticknor, John L. Bohn, and Deborah S. Jin, Creation of ultracold molecules from a Fermi gas of atoms. Nature **424**, 47 (2003).

[45] Hendrick L. Bethlem, Giel Berden, Andre J. A. van Roij, Floris M. H. Crompvoets, and Gerard Meijer, Trapping Neutral Molecules in a Traveling Potential Well. Physical Review Letters **84**, 5744 (2000).

[46] R. Fulton, A. I. Bishop, and P. F. Barker, Optical Stark Decelerator for Molecules. Physical Review Letters **93**, 243004 (2004).

[47] S.A. Rangwala, T. Junglen, T. Rieger, P.W.H. Pinkse, and G. Rempe, A continuous source of translationally cold dipolar molecules. arXiv:physics/020904 (2002).

[48] R. deCarvalho, J.M. Doyle, B. Friedrich, T. Guillet, J. Kim, D. Patterson, and J.D. Weinstein, Buffer-gas loaded magnetic traps for atoms and molecules: A primer. The European Physical Journal D **7**, 289 (1999).

[49] John M. Doyle, Bretislav Friedrich, Jinha Kim, and David Patterson, Buffer-gas loading of atoms and molecules into a magnetic trap. Physical Review A **52**, R2515 (1995).

[50] Jonathan D. Weinstein, Robert deCarvalho, Thierry Guillet, Bretislav Friedrich, and John M. Doyle, Magnetic trapping of calcium monohydride molecules at millikelvin temperatures.. Nature **395**, 148 (1998).

[51] *Atomic and Molecular Beam Methods*, edited by Giacinto Scoles (Oxford University Press, New York, 1988).

[52] *Foundations of Vacuum Science*, edited by J. M. Lafferty (John Wiley and Sons, Inc., New York, 1998).

[53] Hongzhi Li, Randall Skelton, Cristian Focsa, Bernard Pinchemel, and Peter F. Bernath, Fourier Transform Spectroscopy of Chemiluminescence from the SrO $A^1\Sigma^+X^1\Sigma^+$ Transition. Journal of Molecular Spectroscopy **203**, 188 (2000).

[54] J.A. Kerr, in *CRC Handbook of Chemistry and Physics*, edited by D.R. Lide (CRC Press, New York, 2000).

[55] R. W. Nicholls, Franck-Condon Factors to High Vibrational Quantum Numbers II: SiO, MgO, SrO, AlO, VO, NO. Journal of Research of the National Bureau of Standards A **66A**, 227 (1962).

[56] Charles W. Bauschlicher Jr., Harry Partridge, Mariona Sodupe, and Stephen R. Langhoff, Theoretical Study of the Alkaline-Earth Metal Superoxides BeO_2 through SrO_2. Journal of Physical Chemistry **96**, 9259 (1992).

[57] D. W. Sedgley, A. G. Tobin, T. H. Batzer, and W. R. Call, Characterization of charcoals for helium cryopumping in fusion devices. Journal of Vacuum Science & Technology A **5**, 2572 (1987).

[58] Jack W. Ekin, *Experimental Techniques for Low-Temperature Measurements* (Oxford University Press, Oxford, 2006).

[59] *Physics Vade Mecum*, edited by Herbert L. Anderson (American Institute of Physics, New York, 1981).

[60] F. Reif, *Statistical and Thermal Physics* (McGraw-Hill, New York, 1965).

[61] N. H. Balshaw, *Practical Cryogenics* (Oxford Instruments, Oxon, England, 1996).

[62] Taken from from a NASA report summarized at http://www.lesker.com/newweb/fluids/greases_cryogenic_apiezon.cfm.

[63] E. J. Bolton, Cryopump system for a laboratory evaporator. Journal of Scientific Instruments **42**, 894 (1965).

[64] Wolfgang Demtroder, *Laser Spectroscopy* (Springer, Berlin, 1998).

[65] R W P Drever, J L Hall, F V Kowalski, J Hough, G M Ford, A J Munley, and H Ward, Laser Phase and Frequency Stabilization Using an Optical Resonator. Applied Physics B **31**, 97 (1983).

[66] Pawel Kruk, Andrzej Noga, Teresa Trepka, Jerzy Zachorowski, and Wojciech Gawlik, Frequency reference for laser spectroscopy with the stabilized 4-m-long FabryPerot cavity. Review of Scientific Instruments **76**, 033109 (2005).

[67] P. Bohlouli-Zanjani, K. Afrousheh, and J. D. D. Martin, Optical transfer cavity stabilization using current-modulated injection-locked diode lasers. Review of Scientific Instruments **77**, 093105 (2006).

[68] E Reidle, S H Ashworth, J T Farrell, and D J Nesbitt, Stabilization and precise calibration of a continuous-wave difference frequency spectrometer by use of a simple transfer cavity. Review of Scientific Instruments **1**, 42 (1994).

[69] W. Z. Zhao, J. E. Simsarian, L. A. Orozco, and G. D. Sprouse, A computer-based digital feedback control of frequency drift of multiple lasers. Review of Scientific Instruments **69**, 3737 (1998).

[70] A. Rossi, V. Biancalana, B. Mai, and L. Tomassetti, Long-term drift laser frequency stabilization using purely optical reference. Review of Scientific Instruments **73**, 2544 (2002).

[71] John H. T. Burke, Ofir Garcia, K. Jeramy Hughes, Brian Livedales, and Charles A. Sackett, Compat implementation of a scanning transfer cavity lock. Review of Scientific Instruments **76**, 116105 (2005).

[72] Dmitry Budker, Simon M Rochester, and Valeriy V Yashchuk, Obtaining frequency markers of variable separation with a spherical mirror Fabry-Perot interferometer. Review of Scientific Instruments **71**, 2984 (2000).

[73] B. G. Lindsay, K. A. Smith, and F. B. Dunning, Control of long-term output frequency drift in commercial dye Basers. Review of Scientific Instruments **62**, 1656 (1991).

[74] R. V. Pound, Electronic Frequency Stabilization of Microwave Oscillators. Review of Scientific Instruments **17**, 490 (1946).

[75] E. B. Shera, N. K. Seitzinger, L. M. Davis, R. A. Keller, and S. A. Soper, Detection of single fluorescent molecules. Chemical Physics Letters **174**, 553 (1990).

[76] J. B. Hasted, *Physics of Atomic Collisions*, 2 ed. (Elsevier Publishing Company, New York, 1972).

[77] Sebastiaan Y.T. van de Meerakker, Nicolas Vanhaecke, Mark P.J. van der Loo, Gerrit C. Groenenboom, and Gerard Meijer, Direct measurement of the radiative lifetime of vibrationally excited OH radicals. Physical Review Letters **95**, 013003 (2005).

[78] John Doyle, private communication.

[79] David Patterson and John M. Doyle, A Bright, Guided Molecular Beam With Hydrodynamic Enhancement. arXiv:physics/0703025v1 (2007).

[80] James B. Anderson, Separation of gas mixtures in free jets. American Institute of Chemical Engineers Journal **13**, 1188 (1967).

[81] P Hartmann, Z Donko, G Bano, L Szalai, and K Rozsa, Effect of different elementary processes on the breakdown in low-pressure helium gas. Plasma Sources Sci. Technol. **9**, 183 (2000).

[82] D. DeMille, D.R. Glenn, and J. Petricka, Microwave traps for cold polar molecules. The European Physical Journal D **31**, 375 (2004).

[83] Dmitry Budker, Derek F. Kimball, and David P. Demille, *Atomic Physics: An exploration through problems and solutions* (Oxford University Press, Oxford, 2004).

[84] Claude Cohen-Tannoudji, Jacques Dupont-Roc, and Gilbert Grynberg, *Atom photon interactions* (Wiley Science, New York, 1992).

[85] Shojiro Nemoto, Nonparaxial Gaussian Beams. Applied Optics **29**, 1940 (1990).